Technische Universität München

Department für Physik

Walther-Meißner-Institut für Tieftemperaturforschung

Bayerische Akademie der Wissenschaften

Spatially resolved spin Seebeck experiments

Diploma Thesis

Michael Schreier

Advisor: PD. Dr. Sebastian T. B. Gönnenwein

Garching, Tuesday 16th October, 2012

Contents

Mystery creates wonder and wonder is the basis of man's desire to understand.

Neil Armstrong

1 Introduction

In the last 100 years technology has advanced at a pace never seen before. The famous "Moore's Law" [1] is probably the most well known example of this seemingly ever accelerating process. Since electricity was first described by Thales[1] followed by extensive research in the 17^{th}, 18^{th} and 19^{th} century by people like Benjamin Franklin [2], Luigi Galvani [3] and André-Marie Ampère [4], this advance has been driven mainly by the transportation and utilization of the electron's charge.

The 20^{th} century however saw the rise of a fundamentally new way to transport information without any flow of charge. In early experiments by Mersevey, Tedrow [5] and Julliere [6] it was discovered that the electron's spin influences charge transport properties to a large extent. This sparked a whole chain of developments and led to the conclusion that even a device that only utilized the spin degree of freedom for transport could be imagined. Nowadays scientists are able to create pure spin currents by a number of techniques, one of which will be extensively discussed in this thesis.

In 1825, Seebeck [7] discovered that a magnetic field could be observed in a ring made from two different but intrinsically non magnetic metals if their two contacts were exposed to different temperatures (Fig. 1.1). What he indeed discovered was that the electrons in the two metals were moving in order to bring the entropy in the system into equilibrium and hence caused a charge current to flow in the ring that in turn gave rise to the magnetic field. The Seebeck effect, as it is called nowadays, is used today in a number of applications. It is, however, restricted to the creation of charge currents. It was not until 2008, when Uchida *et al.* [8] discovered that a thermal nonequilibrium not only influences charge transport but also spin distribution, which Seebeck might have made responsible for his observation did he know spins even existed.

The spin Seebeck effect, as it was called by Uchida *et al.*, describes the creation of a pure spin current that originates from a complex interaction of phonons, magnons and electrons at interfaces.

[1] Thales of Milet c. 624 BC - c. 546 BC

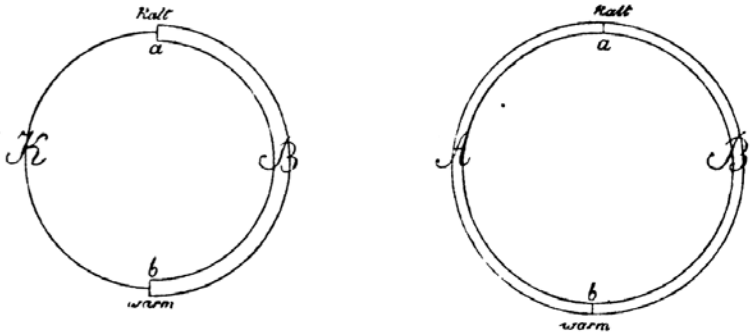

Figure 1.1: Picture taken from Seebeck's original publication [7]. By heating one of the contacts **a** and **b** with a spirit of wine lamp he observed how the rings suddenly created a magnetic field that he observed with a magnetic needle. **A**, **B** and **K** denote the metals antimony, bismuth and copper.

Since the discovery of the spin Seebeck effect many questions arose on its origin, nature and even its very existence was doubted at times. Starting from the foundations laid by Uchida and his co workers [8], the theory work from Bauer, Xiao [9] and others and especially the research that was done at the Walther-Meißner-Institute by Weiler, Meyer and co-workers, this thesis focusses on creating a qualitative and quantitative and consistent understanding of how spin currents are created by the spin Seebeck effect: what factors influence their creation and transport and how the spin Seebeck effect compares to other spin current driven effects.

It is found that previous and current "spin Seebeck measurement" can not be understood in terms of the anomalous Nernst effect, that the processes involved happen on timescales smaller than 1 µs and maybe most importantly that there is strong evidence the spin Seebeck and the other spin current driven effects (the spin Hall magneto resistance and spin pumping) indeed arise from the same microscopic physics.

This thesis is organized as follows: starting with an introduction to the theory behind the spin Seebeck effect (Ch. 2), followed by results (Ch. 4) obtained from a special measurement technique, which is explained in detail in the corresponding section (Sec. 4.1) and whose challenges, theoretical and practical limits will be laid out throughout the course of this thesis, it is explained how the experimental results are influenced by different sample parameters and the measurement setup. The samples studied in this thesis are mostly platinum/yttrium iron garnet hybrids which are presented in Ch. 3. The data was analyzed with help of a numerical thermal profile simulation (Sec. 5.2) and then compared to results from other experiments that also focus on the creation of spin currents (Ch. 6). The thesis concludes with a summary of the main results and the remaining open questions and an outlook on possible future experiments (Ch. 7).

2 Theory

When the spin Seebeck effect was first discovered [8], it was already proposed that this effect originates from a thermally induced imbalance in the electrochemical potential of the two electron spin species. However, a thermal excitation also gives rise to "conventional" magneto-thermo-caloric effects, which need to be critically considered in spin Seebeck experiments. A brief introduction into the most relevant magneto-thermo-caloric effects will therefore be given in the following.

2.1 Classical thermo-electric effects

The interplay between heat and electric currents has been known since the 1820's [7]. Since then an understanding of how exactly heat and electrical conduction are linked to each other has gradually been developed. Nevertheless thermo-electric effects are still a topic of current research. Among the plethora of phenomenona that couple heat and electrical currents, the *Seebeck* and the *Nernst* effect are of special interest to this thesis and will be discussed in more detail in the following.

2.1.1 Seebeck effect

In the solid state, phonons always contribute to heat transportation [10]. However, additional transport channels can be provided, e.g. by electrons or magnons [10]. When a thermal gradient is applied to a conductor the charge carriers will redistribute such as to thermally equilibrate the system. In the specific case of an assumed *local* thermal equilibrium at the hot and cold end of the conductor according to the Fermi-Dirac

distribution [11, 12]

$$F(E) = \frac{1}{e^{\frac{E-E_F}{k_B T}} + 1}, \tag{2.1}$$

more charge carriers in high energy states are present at the hot side of the solid compared to the cold side. In order to establish a thermal equilibrium in the system charge carriers on the hot side will move to the cold side, carrying energy and increasing the entropy of the system[1]. Consequently a charge imbalance builds up, which results in an electric field that counteracts this movement until the system is in steady state. The strength of this balancing motion and the resulting electric field is described by the Seebeck coefficient S.

Defining the electrical current density as $\boldsymbol{j}_c = \sigma \boldsymbol{E} - \alpha \nabla T$ and the heat current density

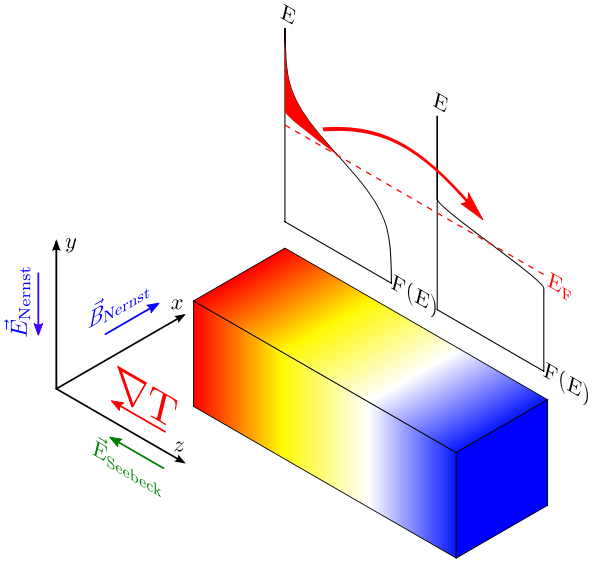

Figure 2.1: In a metal the electrons move from the hot to the cold side of the sample which results in an electric field that counteracts this movement. Applying a magnetic field $\boldsymbol{B}$ perpendicular to the movement of the electrons creates a Hall type geometry that leads to an electric field perpendicular to both ∇T and $\boldsymbol{B}$.

as $\boldsymbol{j}_Q = \beta \boldsymbol{E} - \kappa \nabla T$ with the electric, thermal and thermoelectric conductivity tensors σ, κ and α, respectively one can express the Seebeck coefficient as (using the geometry of Fig. 2.1) [13]

$$S = \frac{-E_{\text{Seebeck}}}{|\nabla T|} = \frac{\alpha_{zz}}{\sigma_{zz}}. \tag{2.2}$$

where α is given by

$$\alpha = \frac{\pi^2 k_B^2 T}{3e} \left.\frac{\partial \sigma}{\partial E}\right|_{E_F}, \tag{2.3}$$

[1] Likewise electrons in low energy states from the cold end will move to the hot end. To preserve the simplicity of the argument this is neglected here.

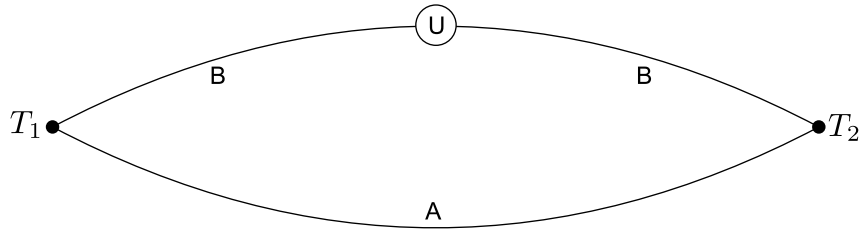

Figure 2.2: The loop of the two conductors A and B is thermalized to two different temperatures T_1 and T_2. If the Seebeck coefficients S_A and S_B are different then a voltage U can be measured along the conductors.

and α and β are connected via the Kelvin relation $\beta = \alpha T$. The Seebeck coefficient S can then be derived as

$$S = -\frac{\pi^2 k_\mathrm{B}^2 T}{3e} \left.\frac{\partial \ln\sigma}{\partial E}\right|_{E_\mathrm{F}}. \tag{2.4}$$

Since the Seebeck effect is difficult to measure directly, usually two different conductors A and B with different Seebeck coefficients S_A and S_B are connected to a loop (Fig. 2.2). Heating (cooling) their contacts causes a current to flow through the system that can be measured as a voltage drop

$$U = \int_{T_1}^{T_2} \left(S_\mathrm{B}(T) - S_\mathrm{A}(T)\right) dT. \tag{2.5}$$

across one of the conductors.

At low temperatures this mechanism can be assisted by the so called *phonon drag* where electrons are "dragged" along by the phonons [10].

2.1.2 Nernst effect

Around 60 years after the discovery of the Seebeck effect [7] Ettingshausen and Nernst discovered that a magnetic field $\boldsymbol{B}$ that is applied perpendicular to a heat current $\boldsymbol{I}_\mathrm{Q}$ leads to the creation of an electric field $\boldsymbol{E} \propto \boldsymbol{B} \times \boldsymbol{I}_\mathrm{Q}$ in the direction perpendicular to both [14]. This can be easily understood in terms of the Lorentz force, which acts on the charge carriers moving from the hot end of the sample to the cold end.

Referring to the geometry of Fig. 2.1 the Nernst coefficient N is defined as [13]

$$\nu = \frac{N}{B} = \frac{E_{\mathrm{Nernst}}}{B_{\mathrm{Nernst}}|\nabla T|} = \frac{\alpha_{zy}\sigma_{zz} - \alpha_{zz}\sigma_{zy}}{\sigma_{zz}^2 + \sigma_{zy}^2}. \tag{2.6}$$

With the help of the Hall angle $\alpha_{\mathrm{H}} = \mathrm{atan}(-\mu B_{\mathrm{Nernst}})$ and the mobility μ, the Nernst coefficient N can be expressed as [13]

$$N = \frac{\pi^2 k_{\mathrm{B}}^2 T}{3e} \left.\frac{\partial \alpha_{\mathrm{H}}}{\partial E}\right|_{E_{\mathrm{F}}}. \tag{2.7}$$

In materials with strong spin-orbit coupling (e.g. ferromagnets) the so called *anomalous* (or spontaneous) Nernst effect (ANE) can occur [15]. While the exact mechanism is still controversially discussed [15] the anomalous Nernst effect also obeys Eq. (2.6) so that

$$\boldsymbol{E}_{\mathrm{ANE}} \propto \boldsymbol{M}_{\mathrm{sp}} \times \nabla T, \tag{2.8}$$

where M_{sp} is the spontaneous magnetization of the material.

2.2 Spin transport phenomena

The effects discussed in Sec. 2.1 arose from an interplay between currents of phonons and electrons (or other charge carriers). Electrons, however, also carry spin angular momentum ("spin" for short) [16]. In addition to charge currents, spin polarized and pure spin currents must be considered [17].
In a two channel model [18] a charge current $\boldsymbol{I}_{\mathrm{c}}$ can be split up into the contributions from particles with spin up ($\boldsymbol{I}_{\uparrow}$) and spin down ($\boldsymbol{I}_{\downarrow}$). For a single species of charge carriers (e.g. electrons) it is obvious that

$$\boldsymbol{I}_{\mathrm{c}} = \boldsymbol{I}_{\uparrow} + \boldsymbol{I}_{\downarrow}, \tag{2.9}$$

as the charge operator $\hat{\boldsymbol{Q}} = -e\mathbb{1}_2$ [18] does not distinguish between spin up and spin down particles. Application of the spin operator $\hat{\boldsymbol{S}} = \hbar/2\,(\sigma_x, \sigma_y, \sigma_z)^{\mathrm{T}}$ with the Pauli matrices σ_i and $det(\hat{\boldsymbol{S}}) = -1$ however yields

$$\boldsymbol{I}_{\mathrm{s}} = -\frac{\hbar}{2e}\left(\boldsymbol{I}_{\uparrow} - \boldsymbol{I}_{\downarrow}\right). \tag{2.10}$$

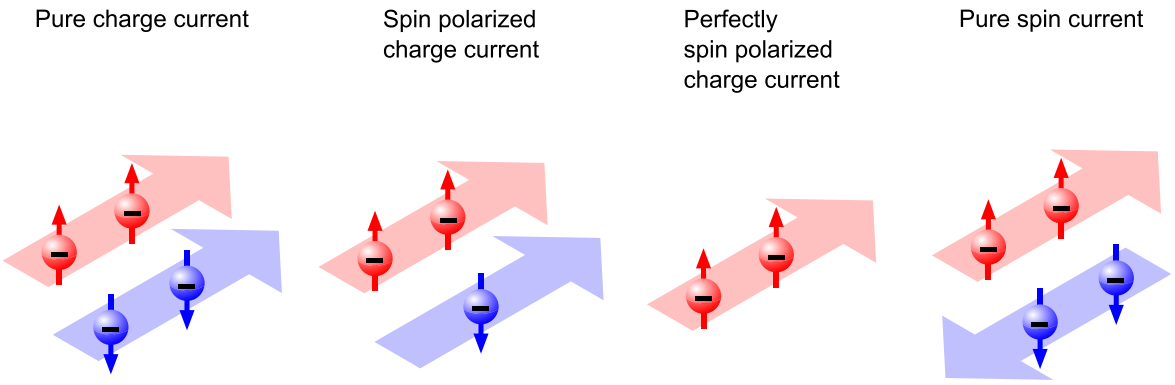

Figure 2.3: In a *pure charge current* spin up and spin down electrons are moving in the same direction. Consequently there is no net flow of angular momentum. In a *spin polarized* and *perfectly spin polarized charge current* spin up and spin down electrons move in different directions but the individual currents are of different magnitude. Both charge and angular momentum are transported. In a *pure spin current* spin up and spin down electrons move in opposite directions so that no charge but angular momentum is transported.

In the absence of any spin dependent scattering mechanisms, such that $\boldsymbol{I}_\uparrow$ and $\boldsymbol{I}_\downarrow$ are parallel and of same magnitude there is no flow of angular momentum ($\boldsymbol{I}_\mathrm{s} = 0$) so that we have a pure charge current $\boldsymbol{I} = \boldsymbol{I}_\mathrm{c} + \frac{2e}{\hbar}\boldsymbol{I}_\mathrm{s} = \boldsymbol{I}_\mathrm{c}$.
The spin orbit interaction, however, gives rise to a number of such processes such as *skew scattering* [19], *side-jumps* [20] and intrinsic contributions [21] all of which cause an imbalance between $\boldsymbol{I}_\uparrow$ and $\boldsymbol{I}_\downarrow$. For $\boldsymbol{I}_\uparrow = -\boldsymbol{I}_\downarrow$ this leads to a pure spin current with no accompanying charge flow whereas for $|\boldsymbol{I}_\uparrow| \neq |\boldsymbol{I}_\downarrow|$ both angular momentum and charge are flowing. Last but no least it is worth mentioning that spin currents can propagate in magnetically ordered materials even in the complete absence of mobile charge carriers. Then $\boldsymbol{I}_\mathrm{s}$ is carried by magnons [22]. The different current types are sketched in Fig. 2.3.

2.2.1 Inverse spin Hall effect

The direct detection of spin currents is not straightforward. An elegant approach is to exploit a method that converts spin currents to a quantity that can be measured with conventional charge-based electronics.
In electrical conductors with pronounced spin-orbit coupling the spin Hall effect [23] converts a charge current flowing in $\hat{\boldsymbol{z}}$ direction into a pure spin current with spin polarization $\hat{\boldsymbol{s}}$. The efficiency of this process is described by the so called *spin Hall angle* θ_H that is

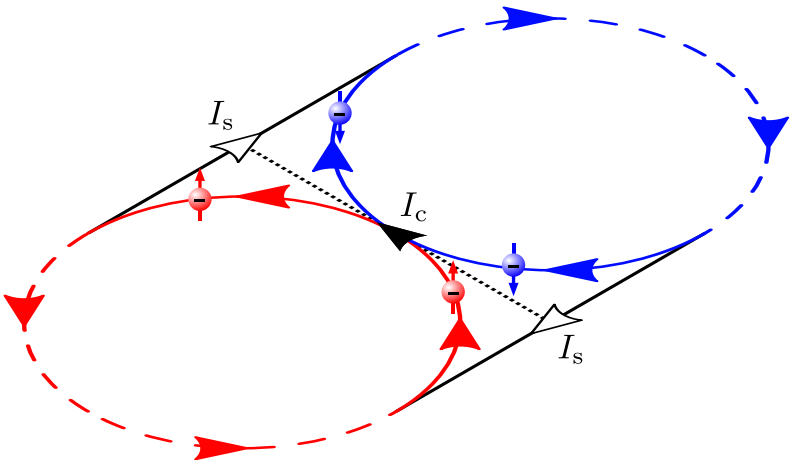

Figure 2.4: Due to the *spin Hall effect* a pure charge current I_c is converted to a pure spin current I_s. The *inverse spin Hall effect* subsequently converts a pure spin into a pure charge current.

given by the ratio of the spin conductivities and the electrical conductivity [18]:

$$\boldsymbol{I}_\mathrm{s}^\mathrm{SH} = \theta_\mathrm{H} \left(-\frac{\hbar}{2e}\right) I_\mathrm{c}[\hat{\boldsymbol{z}} \times \hat{\boldsymbol{s}}]. \tag{2.11}$$

The inverse spin Hall effect is therefore given by

$$\boldsymbol{I}_\mathrm{c}^\mathrm{ISH} = \theta_\mathrm{H} \left(-\frac{2e}{\hbar}\right) I_\mathrm{s}[\hat{\boldsymbol{z}} \times \hat{\boldsymbol{s}}], \tag{2.12}$$

where $\hat{\boldsymbol{z}}$ is now the direction of flow of the spin current.
Inverse spin Hall effect and Nernst effect share the same geometry (*cf.* Fig. 2.1 and 2.6). This represents an important issue for the interpretation of the *longitudinal* spin Seebeck effect, which is addressed in the following.

2.2.2 Spin Seebeck effect

In the spin Seebeck effect a pure spin current is generated through thermal activation of a precessing motion of magnetic moments which is subsequently redistributed.
A very intuitive model for the spin Seebeck effect was given by Xiao *et al.* [9], and is briefly sketched in the following.

Spin current generation

The approach by Xiao *et al.* is based on the results of Tserkovnyak *et al.* [24] who showed that the energy inherent to temperature induces a precessing motion of magnetic moments. In proximity to a reservoir this causes a spin current

$$\boldsymbol{j}_{\mathrm{sp}}(t) = \frac{\hbar}{4\pi}\left[\mathrm{Re}(g^{\uparrow\downarrow})\boldsymbol{m}(t) \times \dot{\boldsymbol{m}}(t) + \mathrm{Im}(g^{\uparrow\downarrow})\dot{\boldsymbol{m}}(t)\right] \tag{2.13}$$

to flow in order to distribute the energy. Here $\boldsymbol{m} = \boldsymbol{M}/M_{\mathrm{s}}V$ denotes the magnetic unit vector with saturation magnetization M_{s} in the volume V and $g^{\uparrow\downarrow}$ is the spin mixing conductance [25] at the interface between the magnet and the reservoir.
This kind of situation can, in principle, occur in any system that allows for the flow of a spin current, when a single magnetic moment in a ferromagnet is excited and relaxes by exciting its neighbours. In reality, however, a bilayer of a ferromagnet F that acts as spin source and a normal metal N that acts as reservoir is usually studied. Such a situation is depicted in Fig. 2.5 which will now serve as the basis for the derivation of the spin Seebeck effect.

For the spin Seebeck effect the temperature that determines the precession amplitude is

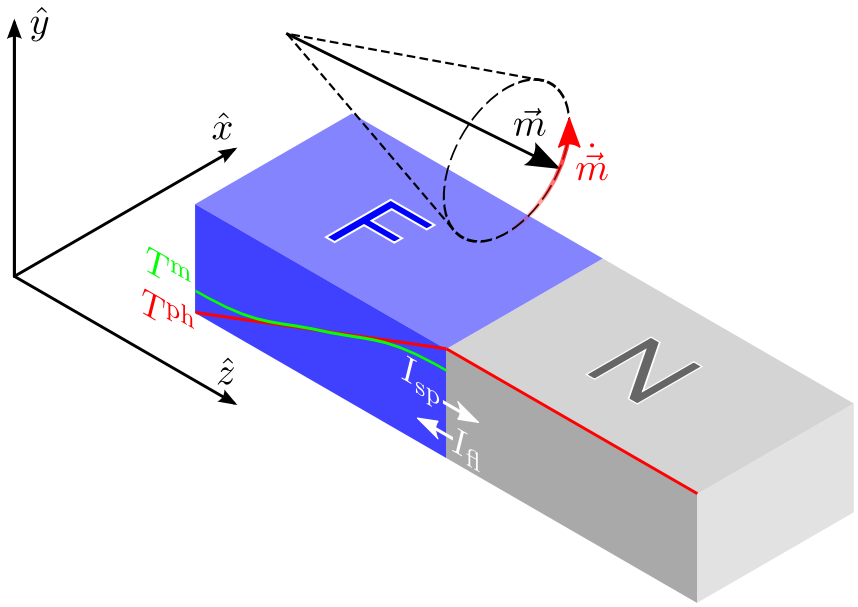

Figure 2.5: A ferromagnet (F) is coupled to a normal metal (N). Assuming different boundary conditions for phonons and magnons different temperature distributions can develop as sketched by the red and green line. The magnetization of the ferromagnet precesses around the $\hat{\boldsymbol{z}}$ direction.

the magnon temperature T^{m}. Now T^{m} must not necessarily be the same as the material's

phonon (T^{ph}) or electron (T^{el}) temperature. Such a mismatch can arise e.g., due to different boundary conditions for the respective heat transport equations. For the phonons (and due to good coupling also the electrons) a continuous temperature distribution and finite first derivative (flow of phonons through the interface is possible) across the interface can be assumed. In contrast, for the magnons no flow across the interface is possible due to the lack of magnon states in the normal metal (Fig. 2.5). Note that the lack of magnon states also means that no temperature $T_{\mathrm{N}}^{\mathrm{m}}$ can be defined in N. Another source for such a mismatch is the existence of thermal contact resistance (see Sec. 5.2) that additionally leads to a discontinuity of the phonon temperature at the interface.
The motion of magnetic moments is usually described by the Landau-Lifshitz-Gilbert equation [26]

$$\dot{\boldsymbol{m}} = -\gamma \boldsymbol{m} \times (\boldsymbol{H}_{\mathrm{eff}} + \boldsymbol{h}) + \alpha \boldsymbol{m} \times \dot{\boldsymbol{m}} \tag{2.14}$$

or

$$\dot{m}_x = -\gamma(m_y H_{\mathrm{eff},z} - m_z H_{\mathrm{eff},y} + m_y h_z - m_z h_y) + \alpha(m_y \dot{m}_z - m_z \dot{m}_y) \tag{2.15}$$

$$\dot{m}_y = -\gamma(m_z H_{\mathrm{eff},x} - m_x H_{\mathrm{eff},z} + m_z h_x - m_x h_z) + \alpha(m_z \dot{m}_x - m_x \dot{m}_z) \tag{2.16}$$

$$\dot{m}_z = -\gamma(m_x H_{\mathrm{eff},y} - m_y H_{\mathrm{eff},x} + m_x h_y - m_y h_x) + \alpha(m_x \dot{m}_y - m_y \dot{m}_x) \tag{2.17}$$

where γ is the gyromagnetic ratio, $\boldsymbol{H}_{\mathrm{eff}}$ the effective magnetic field, α the Gilbert damping parameter and $\boldsymbol{h}$ a randomly fluctuating field from various sources such as thermal or contact noise [9]. In the experiments, presented later in this thesis (Ch. 4), the effective magnetic field $\boldsymbol{H}_{\mathrm{eff}}$ will essentially be given by an external magnetic field. A comparison shows that the term proportional to $\mathrm{Re}(g^{\uparrow\downarrow})$ in Eq. (2.13) is equivalent to the Gilbert damping term in Eq. (2.14). Due to the fluctuation-dissipation theorem (Eq. (2.30)) the spin current $\boldsymbol{j}_{\mathrm{sp}}$ has to be accompanied by a fluctuating spin current arising from thermal noise in the reservoir described by a random magnetic field $\boldsymbol{h}'$

$$\boldsymbol{j}_{\mathrm{fl}} = -\frac{M_{\mathrm{s}} V}{A\gamma} \gamma \boldsymbol{m}(t) \times \boldsymbol{h}'(t), \tag{2.18}$$

where A is the area of the F/N interface.
The total current density from the ferromagnet to the normal metal is then given by

$$\boldsymbol{j}_{\mathrm{s}} = \boldsymbol{j}_{\mathrm{sp}} + \boldsymbol{j}_{\mathrm{fl}}. \tag{2.19}$$

The static (DC) component of this current is given by

$$\langle \boldsymbol{j}_{\mathrm{s}} \rangle_{\mathrm{DC}} = \frac{M_{\mathrm{s}} V}{\gamma} \left[\alpha' \langle \boldsymbol{m} \times \dot{\boldsymbol{m}} \rangle - \frac{\gamma}{A} \langle \boldsymbol{m} \times \boldsymbol{h}' \rangle \right], \tag{2.20}$$

with $\alpha' = (\gamma\hbar \mathrm{Re}(g^{\uparrow\downarrow})/4\pi M_\mathrm{s} V)$ and where $\langle \cdots \rangle$ denotes the ensemble average.
With the geometry of Fig. 2.5 in mind, where the net flow of angular momentum is from the ferromagnet F to the normal metal N in $\hat{\boldsymbol{z}}$ direction, the spin current reads

$$\langle j_z \rangle = \frac{M_\mathrm{s} V}{\gamma} \left[\alpha' \langle m_x \dot{m}_y - m_y \dot{m}_x \rangle - \frac{\gamma}{A} \langle m_x h'_y - m_y h'_x \rangle \right]. \tag{2.21}$$

For the random magnetic fields $\boldsymbol{h}$ and $\boldsymbol{h}'$ the fluctuation-dissipation theorem (Eq. (2.30)) furthermore yields [27, 28]

$$\begin{aligned} \langle \gamma h'_i(t) \gamma h'_j(0) \rangle &= \frac{2\alpha' \gamma k_\mathrm{B} T_\mathrm{N}}{M_\mathrm{s} V_\mathrm{mc}} \delta_{ij} \delta(t) \\ \langle \gamma h_i(t) \gamma h_j(0) \rangle &= \frac{2\alpha \gamma k_\mathrm{B} T_\mathrm{F}^\mathrm{m}}{M_\mathrm{s} V_\mathrm{mc}} \delta_{ij} \delta(t) \end{aligned} \tag{2.22}$$

where the temperature $T_\mathrm{N} = T_\mathrm{N}^\mathrm{el} = T_\mathrm{N}^\mathrm{ph}$ in the normal metal is assumed to be equal for both phonons and electrons and $i, j = x, y$. The volume V_mc here is in fact *not* the volume of the ferromagnet but the so called *magnetic coherence volume* [9]. This quantity describes the region in which a local perturbation influences the magnetic moments. It is given by [29]

$$V_\mathrm{mc} = \frac{2}{3\zeta\left(\frac{5}{2}\right)} \left(\frac{4\pi D}{k_\mathrm{B} T_\mathrm{F}^\mathrm{m}} \right)^{3/2} \tag{2.23}$$

and takes a value of $V_\mathrm{mc} \approx (5.4\,\mathrm{nm})^3$ for yttrium iron granet [29], the ferromagnet used for most samples in this thesis. $D = 2\pi\hbar A_\mathrm{ex}/M_\mathrm{s}$ denotes the spin stiffness with exchange constant A_ex. For extended ferromagnets all occurrences of V in this chapter have to be substituted by V_mc.
In a near equilibrium situation the Landau-Lifshitz-Gilbert equation can be linearized along the $\hat{\boldsymbol{z}}$ direction ($m_z \simeq 1 \Rightarrow \dot{m}_z = 0,\ h_z \simeq 0,\ \boldsymbol{H}_\mathrm{eff} = H_\mathrm{eff}\hat{\boldsymbol{z}}$). Using $\gamma H_\mathrm{eff} = \omega_0$ Eq. (2.15) and (2.16) then take the following form

$$\dot{m}_x + \alpha \dot{m}_y = -\omega_0 m_y + \gamma h_y \tag{2.24}$$

$$\dot{m}_y - \alpha \dot{m}_x = +\omega_0 m_x - \gamma h_x. \tag{2.25}$$

Fourier transforming the equations via $\tilde{f}(\omega) = \int f(t) \mathrm{e}^{i\omega t} dt$ yields

$$\tilde{m}_x \left[(\omega_0 - i\alpha\omega)^2 - \omega^2 \right] = (\omega_0 - i\alpha\omega)\gamma\tilde{h}_x - i\omega\gamma\tilde{h}_y \tag{2.26}$$

$$\tilde{m}_y \left[(\omega_0 - i\alpha\omega)^2 - \omega^2 \right] = i\omega\gamma\tilde{h}_x - (\omega_0 - i\alpha\omega)\gamma\tilde{h}_y. \tag{2.27}$$

Introducing

$$\chi(\omega) = \frac{1}{(\omega_0 - i\alpha\omega)^2 - \omega^2} \begin{pmatrix} \omega_0 - i\alpha\omega & -i\omega \\ i\omega & \omega_0 - i\alpha\omega \end{pmatrix} \tag{2.28}$$

the above can be written as

$$\tilde{m}_i(\omega) = \sum_j \chi_{ij}(\omega)\gamma\tilde{h}_j(\omega). \tag{2.29}$$

With the help of Nyquist's fluctuation dissipation theorem [30]

$$S(\omega) = \int \langle M(t), M(0)\rangle \mathrm{e}^{i\omega t} dt = \frac{2k_\mathrm{B}T}{\omega}\mathrm{Im}\chi(\omega) \tag{2.30}$$

the ensemble averages in Eq. (2.21) can be computed, resulting in (*cf.* [31, 9])

$$\langle j_z \rangle = \frac{\gamma\hbar\mathrm{Re}(g^{\uparrow\downarrow})k_\mathrm{B}}{2\pi M_\mathrm{s} V_\mathrm{mc}} \left(T_\mathrm{F}^\mathrm{m} - T_\mathrm{N}\right). \tag{2.31}$$

For the experimental geometry used in this thesis (Fig. 5.4) it is assumed that the difference $T_\mathrm{F}^\mathrm{m} - T_\mathrm{N}$ can be expressed as

$$T_\mathrm{F}^\mathrm{m} - T_\mathrm{N} = T_\mathrm{F}^\mathrm{ph} - T_\mathrm{N}^\mathrm{ph} = \Delta T \tag{2.32}$$

due to thermal contact resistance and negligible temperature change within F and N, respectively (see Sec. 5.2). This is in contrast to the expression derived by Xiao *et al.* who assume that ΔT originates entirely from the different boundary conditions for the magnons (T_F^m) and phonons (T_F^ph) in the ferromagnet, with the latter continuously continuing into the normal metal ($T_\mathrm{F}^\mathrm{ph}\Big|_{\mathrm{F/N\ interface}} = T_\mathrm{N}|_{\mathrm{F/N\ interface}}$). Note that Eq. (2.32) does not contradict the original expression derived by Xiao *et al.* but is merely taking into account the different geometries of the experimental setups.

Spin current conversion

In the spin Seebeck effect the spin current generated as just described is then detected via the inverse spin Hall effect (via conversion of the spin current into a charge current which can be measured by conventional means).

Due to the inverse spin Hall effect (Eq. (2.12)), the spin current is transformed as:

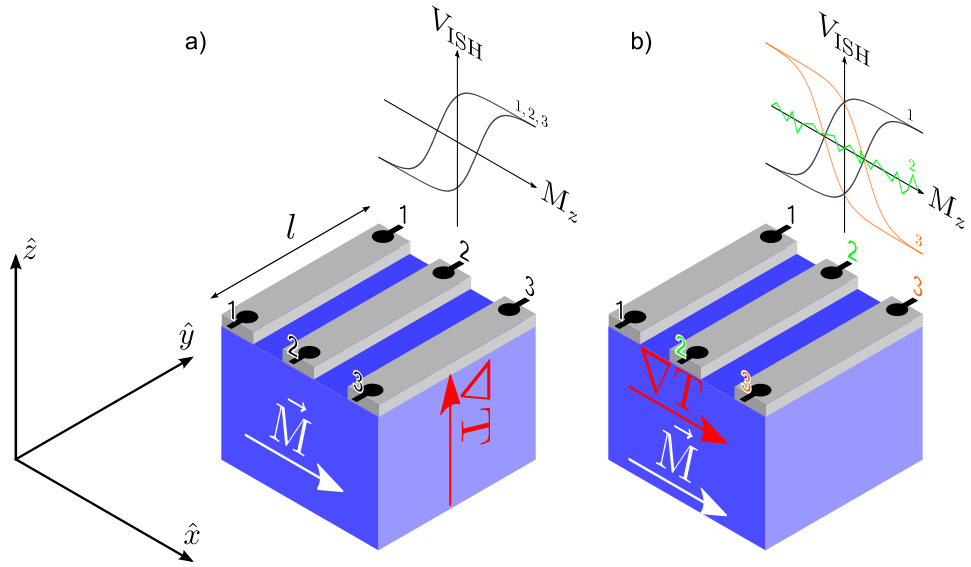

Figure 2.6: The two different geometries in which the spin Seebeck effect can be observed. **a)** In the *longitudinal* spin Seebeck effect the temperature gradient is perpendicular to the magnetization and along the F/N interface normal. **b)** In the *transversal* spin Seebeck effect temperature gradient and magnetization lie in the same plane. The characteristic signature is that the sign of the obtained voltage changes continuously along the temperature gradient. The spin Seebeck effect was first observed in the transversal geometry [8].

$$j_c \hat{\boldsymbol{x}} = \theta_H \frac{2e}{\hbar} \langle j_z \rangle \hat{\boldsymbol{s}} \times \hat{\boldsymbol{z}}. \tag{2.33}$$

Inserting Eq. (2.31) into Eq. (2.33) and using the relation $V_{ISH} = \rho l j_c$ where l is the length of the normal metal in $\hat{\boldsymbol{x}}$ direction, the final expression for the spin Seebeck voltage takes the form

$$V_{ISH} = \frac{\rho \theta_H e \gamma \mathrm{Re}(g^{\uparrow\downarrow}) k_B}{\pi M_s V_{mc}} l \Delta T. \tag{2.34}$$

In the spin Seebeck experiments discussed in this thesis, the temperature difference ΔT (Eq. (2.32)) is induced via local illumination of the F/N bilayer by a focussed laser beam with power P. In this case, in simple terms, one can say that the amplitude and sign of the spin Seebeck voltage are given by the temperature difference ΔT in $\hat{\boldsymbol{z}}$ direction, with the magnetization direction in the ferromagnet determined by an external magnetic field $\boldsymbol{H}_{ext}$ and the measurement direction $\hat{\boldsymbol{y}}$ (see Fig. 2.6)

$$V_{ISH} \propto \boldsymbol{m}(\Delta T \hat{\boldsymbol{y}}) \propto \frac{\boldsymbol{H}_{ext}}{H_{ext}} P \cdot \hat{\boldsymbol{y}}. \tag{2.35}$$

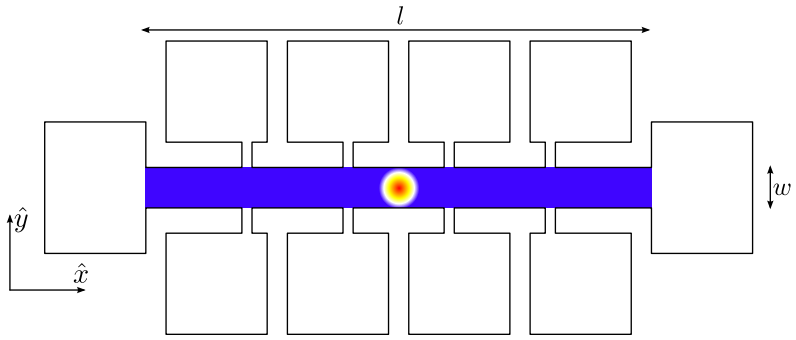

Figure 2.7: Sketch of the temperature distribution across the Hall bar as induced by the local laser heating. Cold parts are depicted in blue whereas hot parts are depicted in red. For the generation of the spin Seebeck voltage only the colored part is taken into account.

Alterations to the theory

Now, the spin Seebeck theory by Xiao *et al.* detailed above was derived for the geometry (Fig. 2.6 **b**) used by Uchida *et al.* [8, 32, 33] and Jaworski *et al.* [34] for their experiments. The spin Seebeck experiments discussed in this thesis use a different geometry that needs to be accounted for to fully capture the experimental situation (Fig. 5.4). Therefore, an extension to the theory outlined above is presented here.

In Eq. (2.34) the assumption is made that the temperature difference ΔT between the magnons in the ferromagnet and the electrons in the normal metal is constant across the entire length l of the F/N interface (see Fig 2.6). In this thesis heat is applied *locally* by a laser beam, such that the aforementioned assumption of constant temperature across the entire interface is certainly not true. Additionally, Weiler *et al.* [35] observed a $1/w$ relation between the spin Seebeck signal and the width w of the normal metal (see Fig.2.7) that is not represented in Eq. (2.34).

To model the experimental situation a laser with a Gaussian beam profile is assumed to hit the Hall bar at its center, for simplicity reasons. It will be shown in Sec. 4.2 that a Gaussian beam profile is indeed a good approximation.

Considering the geometry as depicted in Fig. 2.7, in a first step the temperature profile across the $\hat{\boldsymbol{x}}$ direction is taken into account by replacing the factor $l\Delta T$ with the integral expression

$$l\Delta T \rightarrow \Delta T' \int_{-l/2}^{+l/2} \mathrm{e}^{-2\left(\frac{x}{a}\right)^2} dx \simeq \Delta T' \int_{-\infty}^{+\infty} \mathrm{e}^{-2\left(\frac{x}{a}\right)^2} dx, \tag{2.36}$$

where $\Delta T'$ denotes the temperature difference $T_{\mathrm{F}}^{\mathrm{ph}} - T_{\mathrm{N}}^{\mathrm{ph}}$ at the center of the laser spot. The approximation $l \to \infty$ in the integration limits is reasonable since the typical Hall bar dimensions in the experiments where around 1 mm in length compared to around 2.5 µm laser spot radius a (Sec. 4.2). Consequently as long as the spot is not very close to the edge of the Hall bar one should not observe any change in signal amplitude which is confirmed in the experiment (see e.g. Fig. 5.3 and 5.2**b**).
Equation (2.34) also assumes constant temperature in $\hat{\boldsymbol{y}}$ direction. To take the nonuniform temperature distribution caused by the laser beam into account the mean temperature along this direction is computed by

$$\Delta T_y^{\mathrm{mean}} = \frac{\Delta T'}{w} \int_{-w/2}^{+w/2} \mathrm{e}^{-2\left(\frac{y}{a}\right)^2} dy \simeq \frac{\Delta T'}{w} \int_{-\infty}^{+\infty} \mathrm{e}^{-2\left(\frac{y}{a}\right)^2} dy. \tag{2.37}$$

The approximation holds with the same argument as in Eq. (2.36).
Combining Eq. (2.36) and 2.37 yields

$$l\Delta T \to \frac{\Delta T'}{w} \int\int \mathrm{e}^{-2\left(\frac{\sqrt{x^2+y^2}}{a}\right)^2} dydx = \frac{\Delta T'}{w} \frac{a^2\pi}{2}. \tag{2.38}$$

With this Eq. (2.34) transforms into

$$V_{\mathrm{ISH}} = \frac{\rho\theta_{\mathrm{H}} e\gamma \mathrm{Re}(g^{\uparrow\downarrow}) k_{\mathrm{B}}}{\pi M_{\mathrm{s}} V_{\mathrm{mc}}} \frac{\Delta T'}{w} \frac{a^2\pi}{2}. \tag{2.39}$$

For the case where the temperature difference is uniform across the entire F/N interface the same calculations (without the $\cdots \to \infty$ approximation) again yield the original result of Eq. (2.34), which makes the extended model consistent with the geometry for which the theory was originally intended for. Additionally both the originally heuristic $1/w$ term and the necessary a^2 dependence now are naturally taken care of. For the later it will be shown later (Sec. 4.6, Ch. 5) that the temperature rise induced by the laser scales with $1/a^2$ but that for $a \lesssim w/2$ it is found that $V_{\mathrm{ISH}} = \text{const.}$ as predicted by Eq. (2.39).
The result of these, originally geometrically motivated, alterations to the original spin Seebeck theory are therefore well reproduced by the experimental data.

In this chapter it was briefly addressed how phonons, electrons and magnons interact and give rise to a number effects that show how rich and complicated a seemingly well known field like the transport of heat can be. While the conventional Seebeck and Nernst effect

rely on the transport properties of conductors, the spin Hall and inverse spin Hall effect made it possible to show that, even in the absence of charge carriers, mechanisms quite similar in their result, but drastically different in their origin, can emerge.
The spin Seebeck effect is therefore fundamentally different from the conventional Seebeck effect due to a number of reasons. Firstly, the conventional Seebeck can, in principle, occur in any electrical conductor whereas the spin Seebeck effect requires the presence of spin polarization that can be excited by the application of heat. Secondly the conventional Seebeck effect gives rise to a *charge* current whereas the spin Seebeck effect gives rise to a *spin* current. Finally the spin Seebeck effect is not dependent on charge carriers at all but can also occur in electric insulators.

3 Samples and materials

During the course of this work, spin Seebeck measurements were conducted on 25 different samples using the setup explained in Sec. 4.1. The main focus was on samples based on the ferromagnetic insulator yttrium iron garnet ($Y_3Fe_5O_{12}$, or YIG for short) that was epitaxially grown in house at the Walther-Meißner-Institute (WMI) by Matthias Althammer and Sybille Meyer.
More specifically, the samples consist of thin yttrium iron garnet films grown on (111) oriented gadolinium gallium garnet or yttrium aluminium garnet substrates. The yttrium iron garnet thin films were covered in situ, without breaking the vacuum, by a normal metal thin film to enable spin current detection. Additionally, samples made from nickel, cobalt, nickel ferrite and magnetite, made by Matthias Althammer, Franz Czeschka, Mathias Weiler and A. Gupta[1] were also examined. Table 3.2 and 3.1 show an overview over all samples investigated. All samples were patterned into Hall bar structures (*cf.* Fig. 3.2) by various members of the magnetics group at the WMI to enable magneto-transport and spin Seebeck experiments.
In the following a short summary of the different materials used in the yttrium iron garnet samples is given.

- **Gadolinium Gallium Garnet (GGG)** The choice of the substrate for the yttrium iron garnet thin films is determined by the need of small lattice mismatch to avoid crystallographic defects. Gadolinium gallium garnet ($Gd_3Ga_5O_{12}$) is commonly chosen [36, 37, 38] due to its lattice constant $a = 12.383\,\text{Å}$ [39] being almost identical to the one of yttrium iron garnet ($a = 12.4\,\text{Å}$) [40]. However, GGG is also a strong paramagnet, which makes experiments at low temperatures problematic, but is not relevant here since the spin Seebeck effect originates at the platinum/yttrium iron garnet interface where the magnetization of the GGG is irrelevant.

[1] University of Alabama, USA

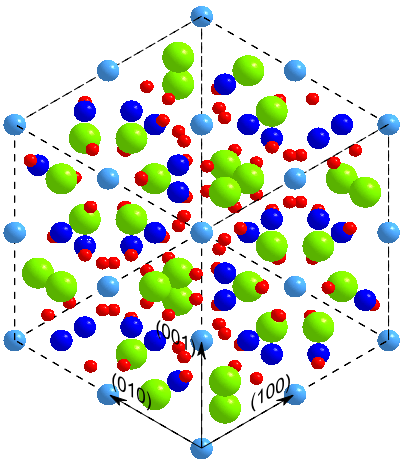

Figure 3.1: Unit cell of yttrium iron garnet. Yttrium is represented in green, oxygen in red and the two different iron sites in blue. The size of the spheres is given by the atoms' atomic radius.

- **Yttrium Aluminium Garnet (YAG)** For experiments where the paramagnetic contribution of the substrate is of concern and also to study the effect of different substrates onto the yttrium iron garnet thin films, yttrium aluminium garnet $Y_3Al_2(AlO_4)_3$ was chosen as an alternative substrate. YAG only exhibits very weak paramagnetism [41] but has a large lattice mismatch ($a = 12.01\,\text{Å}$) [42] with YIG.

- **Yttrium Iron Garnet (YIG)** To avoid the occurrence of the Nernst effect (Sec. 2.1.2) the electrically insulating ferrimagnet yttrium-iron-garnet $Y_3Fe_2(FeO_4)_3$ is used as the source for the spin currents in this thesis. YIG is an artificially created member of the garnet group where calcium (Ca) has been substituted by yttrium (Y) and both silicon (Si) and aluminum (Al) by iron (Fe) compared to natural garnet ($Ca_3Al_2(SiO_4)_3$). The crystal structure is *bcc* so that a unit cell ($a = 12.4\,\text{Å}$) [40] of YIG consists of four complete YIG formula units with a total of 80 atoms. Due to the complex structure (see Fig. 3.1) of the unit cell the five Fe(III)-ions occupy two different types of positions within the unit cell leading to ferrimagnetic behaviour. The exchange coupling breaks down at a temperature of $T_C = 560\,\text{K}$ [40, 43].
  The YIG thin films investigated here are grown at a substrate temperature of 550°C via laser molecular beam epitaxy from a stochiometric polycrystalline yttrium iron garnet target. The laser was operating with a wavelength of $\lambda = 248\,\text{nm}$ at a repetition rate of 10 Hz depositing $2\,\text{J/cm}^2$ at the target in a $p = 25\,\mu\text{bar}$ oxygen atmosphere [44]. More details on the growth process and structural poperties can be found in [44, 45].

- **Platinum (Pt)** To detect the spin current from the YIG the inverse spin Hall effect (Sec. 2.2.1) is utilized. A large spin Hall angle is therefore beneficial to the experiment. Platinum exhibits a spin Hall angle of $\theta_{\mathrm{H}} = 0.013$ [46] or even larger [44], which is considerably larger than the spin Hall angle found in most other metals. The platinum was deposited in situ, without breaking the vacuum, on top of the YIG thin films via electron beam evaporation.

- **Copper (Cu) and gold (Au)** In some samples a buffer layer of either copper or gold is deposited between the YIG and the platinum. Except for sample #13 this was done to critically test the impact of magnetic proximity polarization induced in the Pt by the YIG [47]. Due to the large lattice mismatch ($a_{\mathrm{Pt/Au/Cu}} \approx 4\,\text{Å}$) the normal metals are all amorphous or polycrystalline. Gold and copper exhibit only small ($\theta_{\mathrm{H}}^{\mathrm{gold}} = 0.0035$) [46] or even vanishing ($\theta_{\mathrm{H}}^{\mathrm{copper}} \approx 0$) [48] spin Hall angles.

sample #	lab name	platinum layer thickness [nm]	buffer layer	YIG layer thickness [nm]	substrate (500 µm)
1	YIG1	unknown		30	GGG
2	YIG19	7		20	GGG
3	YIG20	7		20	GGG
4	YIG44	7	Au (7 nm)	20	GGG
5	YIG45	7	Cu (9 nm)	20	GGG
6	YIG55	5		46	GGG
7	YIG56	3		65.5	GGG
8	YIG57	2		58	GGG
9	YIG58	1.5		56	GGG
10	YIG59	11		37.5	GGG
11	YIG60	8.5		54	GGG
12	YIG61	17		54	GGG
13	YIGAu1	-	Au (7 nm)	unknown	GGG
14	YY14	7		70	YAG
15	YY17	3		45	YAG
16	YY19	3	Au (10 nm)	45	YAG
17	YY21	20		45	YAG
18	YY22	7		45	YAG
19	YY24	10		45	YAG
20	YY26	15		45	YAG

Table 3.1: Overview over the YIG based samples

sample #	lab name	composition
21	FBI2	Ni(50 nm)-MgO(500 µm)
22	FBI3	Co(50 nm)-MgO(500 µm)
23	NFO	Pt(10 nm)-$NiFe_2O_4$(620 nm)-$MgAl_2O_4$
24	SP1	Pt(7 nm)-Ni(10 nm)-MgO(500 µm)
25	SP35	Pt(7 nm)-Fe_3O_4(20 nm)-MgO(500 µm)

Table 3.2: Overview over the non-YIG samples

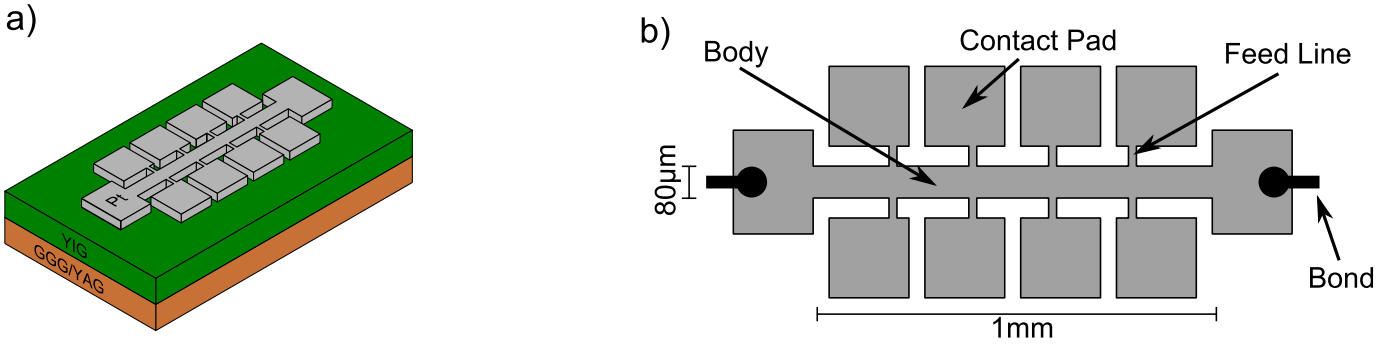

Figure 3.2: a) Schematic of a standard sample (e.g., sample #3). The platinum is deposited on the YIG during the initial growth process. Using photolithography and ion beam etching the Pt is then patterned into a Hall bar structure. **b)** Schematic with dimensions of the Hall bar with the naming convention that is used in this thesis.

4 Experimental results

In this chapter, the main experimental results obtained in this thesis are presented and discussed. A more involved quantitative analysis requires qualitative information about ΔT and thus is postponed to Sec. 6.1. In this chapter, first, the optics used in the experiments are characterized. Then the results of local spin Seebeck measurements conducted on several samples will be summarized. These data show that all the experimental results in this thesis are qualitatively consistent with the spin Seebeck effect and that the relevant timescales for the spin Seebeck effect must be smaller than 1 µs.

4.1 Experimental setup

Most spin Seebeck experiments to date [32, 33, 34] were done by applying a homogeneous temperature gradient across the whole sample. This method is comparatively easy to set up and makes it easier to detect the voltage induced by the spin Seebeck effect since the whole sample is heated. However, questions of sample geometry, local effects and the role of interfaces for example can hardly be studied.
Therefore, a new spin Seebeck measurement method was developed at the WMI by Weiler *et al.* [35, 49] where, instead of applying a spatially homogeneous temperature gradient, a focussed, scannable laser (*cf.* Fig. 4.1) is used to generate a *local* thermal gradient. It will be shown later (see Ch. 5) that an increase of the sample's surface temperature of about 50 K can be achieved with this method using the setup presented in this thesis. A schematic of the setup is shown in Fig. 4.1.

Throughout the course of this work, two different laser diodes with wavelengths of 658 nm and 660 nm, and output powers of 46 mW and 120 mW, respectively, have been used. The laser beam is coupled into a single mode optical fibre that terminates in a $f = 11$ mm lens mounted onto a xyz-stage with a 4 mm scanning range in each direction. That way one can scan the laser beam across a sample's surface. The latter is mounted between

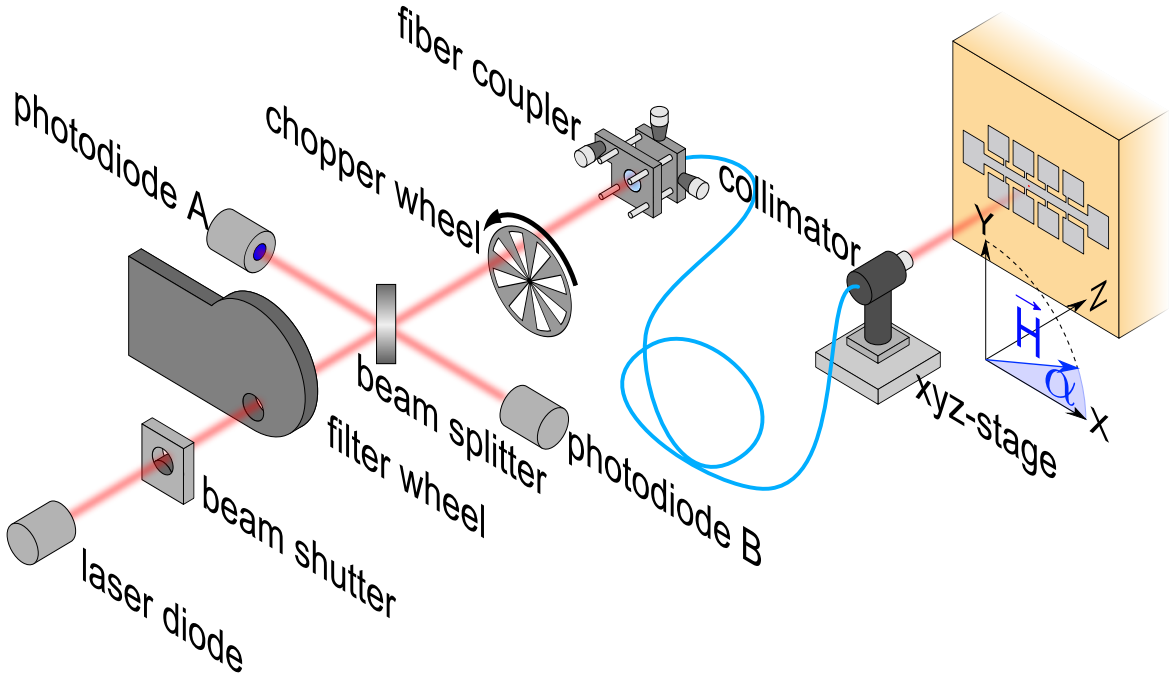

Figure 4.1: Depiction of the experimental setup used for the spin Seebeck measurements. The laser beam from the laser diode can be blanked by an electronic beam shutter or adjusted in intensity by a filter wheel. A beam splitter is used in some experiments to either record light that is reflected from the sample or directly measure the shape and intensity of the laser beam. A chopper wheel is used to modulate the beam to allow for lock-in detection of the signal created by the spin Seebeck effect. The laser beam is coupled into a fiber that terminates in a collimator mounted onto a xyz-stage. That way the laser beam can be scanned across the sample. The complete setup is mounted onto an optical table to stabilize the system against external influences such as vibrations. The sample is depicted not to scale.

two pairs of magnetic coils that form a 2D vector magnet. In addition to the already present chopper wheel, an electronic beam shutter, a filter wheel and a beam splitter were inserted into the beam's path. The filter wheel is fitted with neutral density filters, allowing the beam power to be varied reproducibly. The beam splitter is utilized in two ways. The beam fraction that is outcoupled from the original beam can be detected by a photodiode (photodiode A in Fig. 4.1) to serve as trigger signal for the time resolved measurements that will be presented in Sec. 4.7 of this thesis. The other purpose is that light reflected from the sample's surface is guided back through the fibre and then by aid of the beam splitter onto another photodiode (photodiode B in Fig. 4.1). That way not only the thermoelectric but also the optical response of a sample can be measured. The chopper wheel is used to modulate the beam intensity in a square wave like fashion to allow for a better signal to noise ratio via lock-in detection. The samples are glued and bonded to a chipcarrier system that enables recording a voltage originating from the

sample to be transmitted via BNC connectors.
For the measurements of the spin Seebeck signal (Sec. 4.4), the voltage arising due to the spin Seebeck effect (*cf.* Eq. (2.39)) is fed into a *Stanford Research SR830* lock-in detector that is triggered via the chopper wheel. The multimeter (or lock-in as well) is used to measure the signal from photodiode B that captures light reflected from the sample's surface (Sec. 4.3). For the time resolved measurements (Sec. 4.7) the signal from the sample is first amplified and then read out by a digitizer card that is triggered directly by the laser light which is measured by photodiode A.
Note that during this thesis from here on, whenever a value for the laser power P is given for the measurements this value is to be understood as the continuous wave equivalent of the laser power. Simplifying the modulation of the laser to

$$P(t) = P_0 \cdot \frac{1}{2}\left[1 + \sin(\omega t)\right].$$

It follows that

$$P = \langle P(t) \rangle = \frac{P_0}{2}.$$

The lock-in technique, however, returns $P(t)$ for those points where $\omega t = \frac{\pi}{2} + 2n \cdot \pi$, hence $P = P_0$. In simple terms, if during this thesis a quantity is given as function of the laser power P this is equivalent to a continuous wave ($P(t) = \text{const}$) measurement at $2P$.

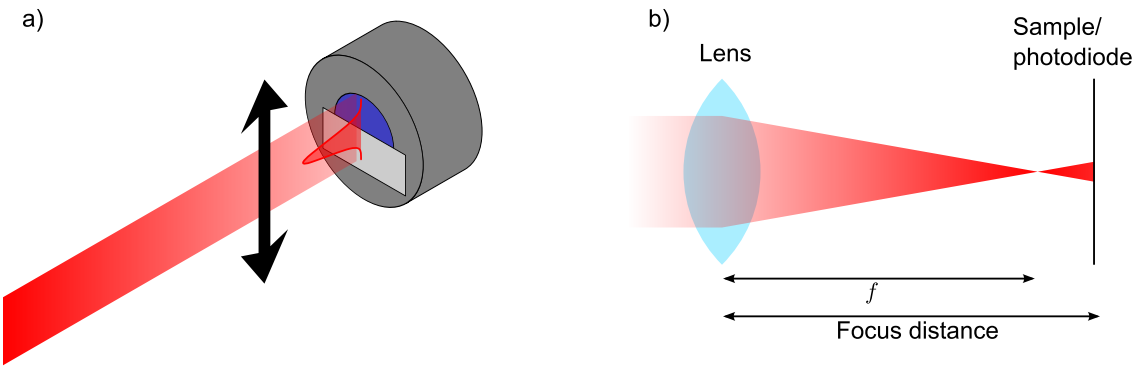

Figure 4.2: a) Depiction of the "knife edge" technique [50]. The sharp edge was made by covering half of the photodiode's sensor with a piece of a scalpel's blade. **b)** The "focus distance" is given by the distance between lens and sample. Note that since the collimator (the lens) is mounted by hand first the position of focus distance= 0 is arbitrarily defined in every measurement. Optimal focus is achieved when the distance between the lens and the sample is equal to the lens' focal distance f.

4.2 Characterization of the laser beam

As described in Sec. 4.1 a laser beam is used to heat the sample and generate the temperature drop across the F/N interface. It was shown in Ch. 2 that the laser spot radius a has to be taken into account for a quantitative analysis of the spin Seebeck effect. The value of the a is determined by the collimation optics but since a enters Eq. (2.39) quadratically a separate measurement of a was done to verify the value quoted in the spec sheet given by the manufacturer. The so called "knife edge" [50] technique is used to determine the laser spot radius. This technique is generally considered to return very accurate and reliable results [50] while being fairly straightforward to conduct.
For the knife edge technique the focussed laser beam is moved across a sharp edge that covers part of a photodiode. Plotting the diode's output current as a function of the laser beam displacement then yields a characteristic curve (Fig. 4.3**a**) allowing to quantify the laser spot radius.

To derive the photodiode current as a function of the laser spot position consider a photodiode in the x-y-plane where $y < 0$ is covered so that no light can reach the sensor here. Assuming a Gaussian laser beam profile $\exp\left[-2\left(\frac{x^2+y^2}{a^2}\right)\right]$ at position $y = b$, it can be derived from simple geometrical considerations that a normalized signal is expected to

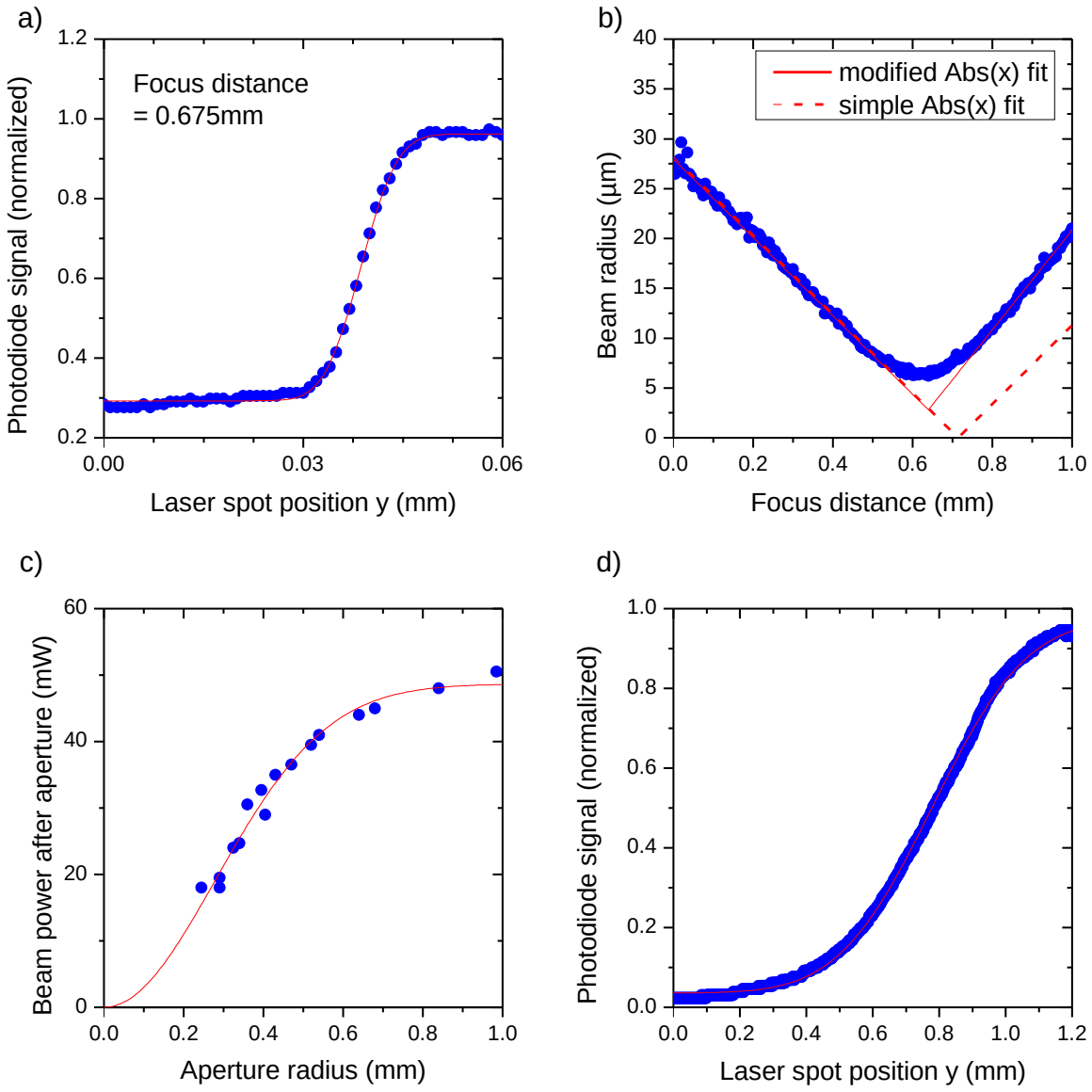

Figure 4.3: The blue dots represent experimental data whereas the red lines are fitted curves according to Eq. (4.2). **a)** The focussed laser beam is moved across the sharp edge. The signal is proportional to the area of the laser spot that is impinging onto the photodiode. The laser spot radius can then be determined from the slope of the curve. **b)** Combination of several measurements of the type shown in a) with varying distance between collimator and photodiode. For a perfectly focussing system the curve is expected to follow the dashed line. Due to the imperfections of the lens the diameter is limited by the lens' numerical aperture. The minimal spot size can then be determined from the difference between the cusp of the solid curve and the minimum of the experimental data. **c)** The laser beam (before collimation) was examined by incrementally closing a ring aperture and measuring the remaining laser power by hand with a power meter. That way one can calculate back the laser beam radius. The value obtained with this technique is slightly larger (0.56 µm) than the one obtained from the other two methods depicted in a) and d), but so is the error. **d)** Same as a) but without collimation optics.

follow

$$g(b) = \frac{2}{a^2\pi} \int_0^{+\infty} \int_{-\infty}^{+\infty} \mathrm{e}^{-2\left(\frac{x^2+(y-b)^2}{a^2}\right)} dxdy \tag{4.1}$$

with a the $\frac{1}{\mathrm{e}^2}$ radius[1] which will also be called beam radius from here on. Figure 4.3**a** shows typical knife edge technique data for the $P = 120\,\mathrm{mW}$ laser used in the majority of the experiments. It can be seen that the photodiode signal does in fact not drop to zero for $b \gg a$ as expected, but has a slight offset c that has to be corrected for in the fit. This is possibly due to diffuse scattering at a wavelength filter in front of the diode. Since the raw data from the photodiode are not normalized this has to be accounted for by a scaling factor s. Additionally it can be seen in Fig. 4.4 that the edge is not at the same position d for different distances between lens and photodiode. Thus the experimental data have to be fitted to

$$c + s \cdot g(b - d) \tag{4.2}$$

This procedure was repeated for varying distances between lens and photodiode to find the optimal focus point. For a perfect lens a plot of the beam radius over the focussing distance z should show a linearly decreasing beam radius until $a = 0$ where it vanishes and subsequently starts to grow linearly again. This $Abs(z)$ type of behaviour with vanishing beam radius at optimal focus is reproduced reasonably well in the data (Fig. 4.3b), although there are several factors that limit the minimal radius. The dominant factor is the diffraction limit which is derived from Ernst Abbe's sine condition [51] that connects the minimal distance between two resolvable points $d_{\min}$ with the lens' numerical aperture A_N:

$$d_{\min} = \frac{0.61 \cdot \lambda}{A_{\mathrm{N}}}. \tag{4.3}$$

The 11 mm lens in the setup has a numerical aperture of $A_{\mathrm{N}} = 0.26$ yielding a lower limit for the spot radius of about 1.5 µm.

The data obtained by the procedure described above yields a minimal beam radius of about 6.4 µm as shown in Fig. 4.3**b** but fitting this to an $Abs(z)$ shows that there is a clear offset in the data, apparently due to the initial offset of the signal at the edge. Taking into account the distance between the fit's cusp and the minimum of the experimental data the minimal beam radius is about 2.5 µm (solid red line in Fig.4.3**b**).

From this one can also calculate the unfocussed beam radius right at the lens which is about 0.5 mm. This can then be compared to measurements following the same procedure as described above, but with the lens removed from the collimator (Fig. 4.3**d**). Additionally an experiment was done in which the radius was determined by measuring the total power through an iris aperture with varying diameter (Fig. 4.3**c**). All three measurements

[1] The radius at which the beam intensity drops by a factor of $\frac{1}{\mathrm{e}^2}$

yield an unfocussed beam radius of just around 0.5 mm, corroborating the result obtained in the first experiment.

Note that the value $a = 2.5\,\mu m$ is about a factor of 2 smaller that the value of 5 µm quoted in the spec sheet of the collimator. However, manufacturers are known to be very conservative with these type of data.

Overall, since all the measurements return about the same optimum value for the laser spot radius a value of $a = 2.5\,\mu m$ will be used throughout this thesis.

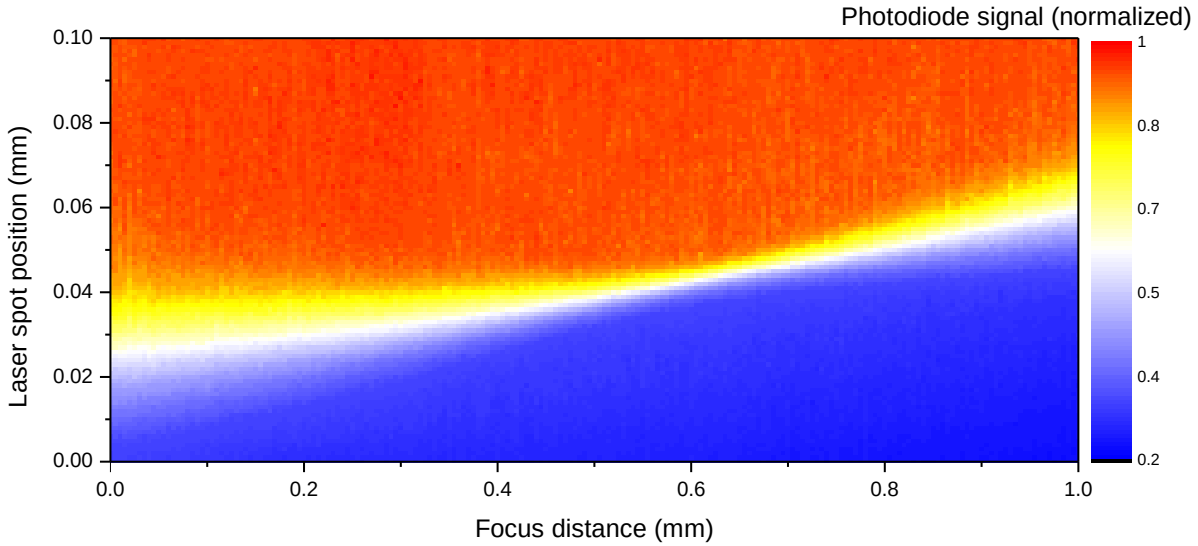

Figure 4.4: Complete result of a "knife edge" measurement (a single line can is shown in Fig. 4.3**a**). The reason why the signal does not go down to 0 is probably due to diffusive scattering at the color filter in front of the lens. The bent edge is due to an angular mismatch between sample and laser

4.3 Laser-raster reflectometry imaging

The immediate benefit of the system described in Sec. 4.1 is that it allows for the observation of local effects in, or properties of the sample.
In order to generate a spatial image of the quantity of interest, the stage is moved in such a fashion that the laser spot scans the sample point by point with a fixed step size that is limited by the stage's accuracy of about 60 nm [52]. The distance between two neighbouring points in this scanning process will be referred to as "resolution" in the following.
As part of this thesis a photodiode (photodiode B in Fig. 4.1) was inserted into the setup in order to simultaneously conduct spin Seebeck measurements and optical imaging: a fraction of the light that reaches the sample is reflected from its surface and recoupled into the fibre. Once it reaches the beam splitter a certain amount is redirected onto the photodiode. The photodiode thus yields a current that is proportional to the reflectivity of the sample's surface. Plotting the photodiode current in false color as a function of the laser spot position (x, y) then gives an image of the sample, just like plotting $V_{\mathrm{ISH}}(x, y)$ gives a map of the spin Seebeck effect [35]. Due to the different refractive indices of the materials composing the sample different amounts of light are reflected making it possible to clearly map the Hall bar structures on the sample as shown in Fig. 4.5. This laser-raster reflectometry imaging allows one to safely attribute the spin Seebeck signal V_{ISH} discussed in Sec. 4.4 to stem exactly from the Hall bar, and that there is no such thing as ghosting where the spin Seebeck signal would appear at a slightly different position than the Hall bar itself.

In Fig. 4.5 Newton's rings [53] can also be observed. Those appear due to reflections between the lens and the sample and can be described by [53]

$$r_n = \sqrt{\left(n - \frac{1}{2}\right)\lambda R} \tag{4.4}$$

where r_n denotes the radius of the n^{th} bright ring, λ the wavelength of the laser and R the curvature of the lens. From the position of the center of the rings, seeming to be located beyond the lower end of the picture, it is theoretically possible to calculate back on the angular mismatch between optical axis and sample normal. For the experiments conducted during this thesis the small angular mismatch was not relevant. Should it however become necessary to have a better alignment between sample normal and optical axis, this effect could be used to properly align the setup.

The optical resolution achieved by the laser-raster reflectometry imaging is limited by the laser spot radius of 2.5 µm. Even though images taken with smaller step sizes between the

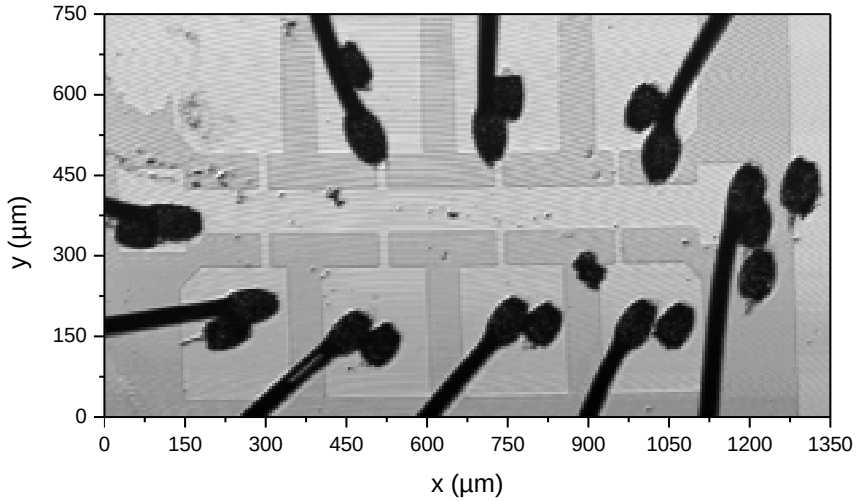

Figure 4.5: Laser-raster reflectometry image of sample #3. The greyscale represents the photodiode current that is proportional to the reflectivity of sample at each position (x, y). The lighter parts outline the shape of the Hall bar. Improper patterning of the Hall bar structure can be seen in the upper left corner. Next to the bonds (black) additional black spots show that the sample has been bonded twice. On the main body of the Hall bar some dirt can be seen (e.g. at around $[450\,\mu\text{m}, 450\,\mu\text{m}]$) that is also reflected in the spin Seebeck image taken simultaneously (see Fig. 4.7).

individual points appear more pleasing (less pixelated) to the eye, no additional features can be observed below a resolution of about 2 µm (Fig. 4.6). Comparing an image that was taken at 16 times the resolution of the 2 µm resolution image to which a Gaussian blur was applied shows a striking similarity, the only notable difference being that the higher resolution image shows more artefacts from the lock-in detection. However it does not resolve the additional finer features that can be seen on a microscope image of the same area. This further supports the notion that, as derived in Sec. 4.2, the laser spot radius is around 2.5 µm.

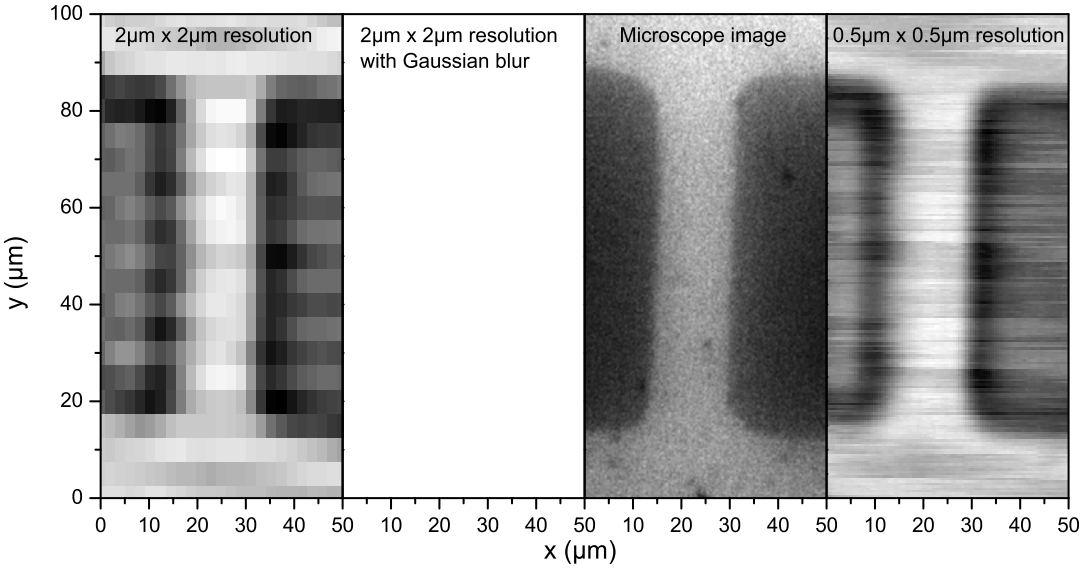

Figure 4.6: Image of a Hall bar's feed line taken at a resolution of 2 µm × 2 µm and 500 µm × 500 nm. The higher resolution image does in fact not resolve more detail as can be seen when it is compared to the Gaussian blur of the 2 µm × 2 µm image. The 500 µm × 500 nm image does also not resolve features that are visible in the conventional microscope image (and are considerably larger than 500 nm), since the resolution of the laser-raster reflectometry imaging is limited by the laser spot radius $a = 2.5\,\mu\text{m}$.

4.4 Local spin Seebeck measurements

With the laser spot well characterized, the spatially resolved spin Seebeck experiments can now be analyzed.

The heating of the sample, caused by the absorption of the laser beam by the sample, generates a temperature difference between the magnons in the ferromagnet and the electrons in the normal metal. This gives rise to the spin Seebeck effect (*cf* Sec. 2.2.2). In all samples the temperature difference ΔT as defined in Sec. 2.2.2 ($T_{\text{F}}^{\text{N}} - T_{\text{N}}$, Eq. (2.32)) is negative, since the platinum that is used as a spin detector has a much higher absorption coefficient for the laser light than the YIG (*cf.* Sec. 4.6). In the same fashion as for the recoding of the the laser-raster reflectometry images (see Sec. 4.3) the laser is scanned in small steps across the sample surface by the xyz-stage. At every laser-spot position (x, y), the voltage $V(x, y)$ (the thermo-galvanic potential) between a pair of electrodes (see Fig. 4.7) is recorded by the lock-in detector. It will be shown in this section that $V = V(x, y)$ originates almost entirely from the spin Seebeck (and subsequently the inverse spin Hall effect), such that V_{ISH} will be used throughout this thesis. Plotting $V_{\text{ISH}}(x, y)$ in a false color plot then returns the desired image, referred to as "spin Seebeck image"

in the following. In this chapter in each spin Seebeck image, an inset depicts the area on the Hall bar from which V_{ISH} originates, indicated by a green rectangle. Each individual point takes about 0.5 s to measure, which is mainly due to the time the stage needs to move from one point to the next. For samples that show a very weak spin Seebeck signal, however, the integration time of the lock-in has to be increased up to around 1 s so that this becomes the limiting factor.

To focus the laser spot onto a sample a process similar to the one in Sec. 4.2 is used. The laser is scanned across the sample in the y-direction (*cf.* Fig. 4.1) for different distances between lens and sample. This returns a square wave like signal for good and a more Gaussian like for bad focus (see also Fig. 5.2). The process can be assisted by the optical signal from photodiode B (Fig. 4.1 and Ch. 4.3) that shows a much sharper peak at the correct focus and therefore makes exact focussing easier.

It is important to note that the sign of the spin Seebeck signal (V_{ISH}) for almost all measurements presented in this thesis has to be considered as arbitrarily defined. This is due to the fact that the signal's true sign can not easily be determined from the lock-in measurements since the signal's phase shift is not known a priori. Additionally the *final* equation of the spin Seebeck theory (Eq. (2.39)) does not account for the sign reversal possible through the external magnetic field. This property was "lost" in the derivation of V_{ISH} when the inverse spin Hall effect was evaluated (Eq. (2.33)) and the magnetization and measurement direction where specifically chosen in such a way that the resulting V_{ISH} was positive. For the quantitative data evaluation (see Sec. 4.6, Ch. 5, Ch. 6) it is therefore, without loss of generality, assumed that the spin Seebeck signal V_{ISH} is positive at all times. A thorough discussion of the spin Seebeck signal's sign is given in in App. A.2.

Figure 4.7 shows a $V_{\mathrm{ISH}}(x, y)$ image where the thermo-galvanic voltage between the

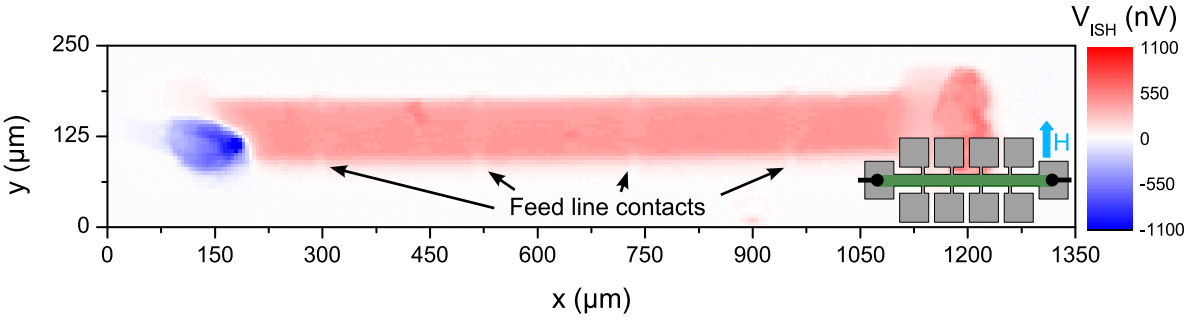

Figure 4.7: Image of sample #3 (YIG/Pt) at 60 mT ($\boldsymbol{H} \| \hat{\boldsymbol{y}}$) and ≈ 3 mW laser power with a resolution of 5 µm × 5 µm per data point. The voltage from the body of the Hall bar is about 400 nV. Clearly visible is the Hall bar itself, the two bonds that are utilized for the readout of the signal and also the places where the feed lines are connected to the main body of the Hall bar.

two contacts at the long ends of the Hall bar is plotted over the position of the laser

spot. Most notable are the two places where the bonding wires are contacted to the Hall bar ($x \cong 150\,\mu m$ and $x \cong 1200\,\mu m$). Here a strong V_{ISH} signal can be detected that has a different sign for each of the two bonds. As this signal doesn't change its sign or magnitude as a function of the magnetic field (see below) this signal is attributed to the conventional Seebeck effect. In accordance with Eq. (2.5) and Fig. 2.2 the two bonds produce a thermal voltage of opposing sign. Using the data of Fig. 4.7 with the Seebeck coefficients for platinum and aluminium ($\Delta S_{Pt-Al} = 3.5\,\mu V/K$) [54] yields a difference in temperature between the two ends of the Hall bar of around 0.3 K. It is shown later in this thesis (Ch. 5) that this rise in temperature seems to be unreasonably small considering that aluminium is an even better absorber for the laser light than platinum by a fair amount ($\alpha_{Al}^{660\,nm}/\alpha_{Pt}^{660\,nm} \approx 1.8$) [55]. Taking into account that also the reflectance ($R_{Pt}^{660\,nm} \approx 0.7,\ R_{Al}^{660\,nm} \approx 0.9$) [55] and thermal conductivity ($\kappa_{Pt} = 72\,W/m\,K,\ \kappa_{Al} = 237\,W/m\,K$) [54] are much higher, however, the result is plausible.
The most interesting observation is the spatially resolved spin Seebeck effect, however: the main body of the Hall bar gives a uniform signal along its length and width which is in good agreement with the spin Seebeck theory (Eq. (2.39)). The exact shape of the signal close to the edges also agrees with the additions made to Eq. (2.34). This is further elaborated on in Sec. 5.1.

In contrast to the *conventional* Seebeck effect (Eq. (2.5)) the *spin* Seebeck effect (Eq. (2.35)) shows a strong dependence on the magnetization direction of the ferromagnet. Figure 4.8 shows two spin Seebeck images for both a positive and a negative external magnetic fields. The external magnetic field forces the magnetization to align itself parallel and thus determines the sign and magnitude at which V_{ISH} can be measured via the inverse spin Hall effect (Eq. (2.12)). For a magnetic field in y-direction the inverse spin Hall effect creates a current in the x-direction and vice versa.

Figure 4.8**a** and **b** do indeed show that by reversing the direction of the external magnetic field V_{ISH} changes sign but is constant in magnitude. One can also record V_{ISH} at a fixed position (x, y) on the Hall bar as a function of the external magnetic field orientation α, such as shown in Fig. 4.8**c**. V_{ISH} clearly follows a $\sin\alpha$ behaviour as predicted by the inverse spin Hall effect and Eq. (2.35). Moreover, Fig. 4.8**c** shows that this $\sin\alpha$ has to be corrected by adding a constant phase φ to α in order to exactly reproduce $V_{ISH}(\alpha)$. This phase φ stems from the slight rotation of the sample that can be seen in Fig. 4.8**a** and **b**. With the data of Fig. 4.7 and 4.8 it was shown that the experimental setup presented in Sec. 4.1 can be used to create a voltage map of the spin Seebeck effect across a sample. Using a 2D vector magnet it is also possible to confirm that the measured voltage does indeed stem from the *spin* and not the *conventional* Seebeck effect.

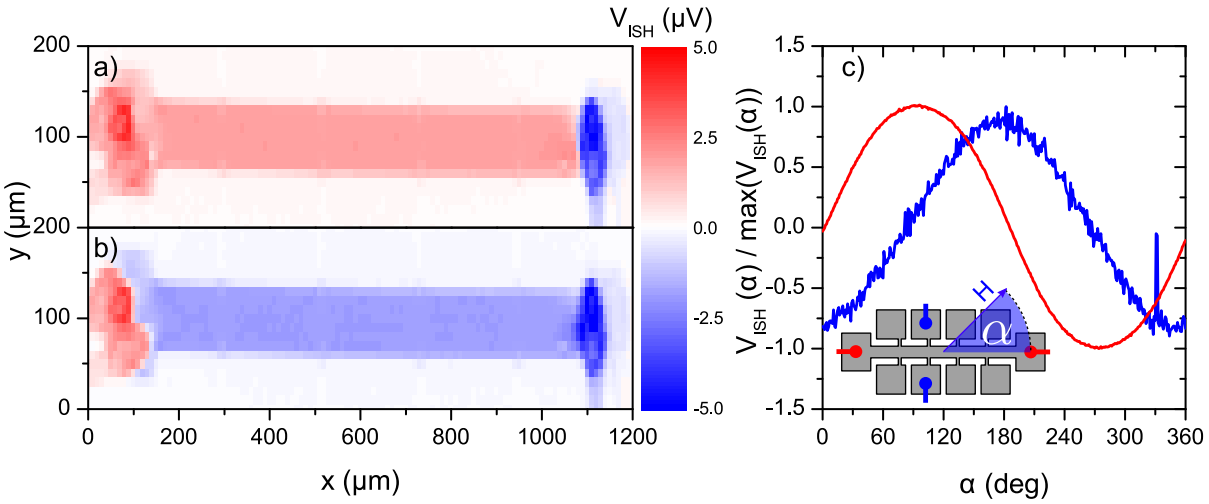

Figure 4.8: a) Spin Seebeck image of sample #14 taken at $H = +70\,\mathrm{mT}$, $\boldsymbol{H} \| \hat{\boldsymbol{y}}$. In this configuration a positive spin Seebeck voltage V_{ISH} is measured. **b)** Same as **a)** but with $H = -70\,\mathrm{mT}$. In accordance with Eq. (2.35) the sign of the measured voltage changes while the magnitude remains unaltered. Note also that V_{ISH} does not change sign with H polarity. **c)** Normalized spin Seebeck voltage V_{ISH} as a function of the orientation α of the external magnetic field. As predicted by Eq. (2.35) a $\sin\alpha$ behaviour is observed (red line). The blue line was simultaneously recorded along two transverse contacts (see Sec. 4.4.4). Here the spin Seebeck voltage is recorded in the y-direction, corresponding to a 90° shift of the measured spin Seebeck voltage, as observed.

4.4.1 Spin Seebeck magnetic domain imaging

An additional benefit of the ability to locally resolve the spin Seebeck signal is that it becomes possible to visualize magnetic domains during the magnetization reversal process. Weiler *et al.* already published first results [35] and their work has been continued in this thesis.

To observe the magnetic domains, the external magnetic field is incrementally changed from positive to negative saturation and a spin Seebeck image is taken at every field. Close to the sample's coercive field these images reveal the magnetic domains.

Figure 4.9 also shows that during a magnetic field sweep the new domain orientation nucleates on one end of the sample and spreads from there to the other end. In the figure this is especially evident from the panels **b)** and **c)** where the positive voltage V_{ISH} area (red) starts to spread from the left to the right end of the Hall bar. The direction in which the domain walls move is always the same for one specific sample for both the up- and downsweep of the magnetic field.

This agrees with observations in thin cobalt films [56] and the formation of end do-

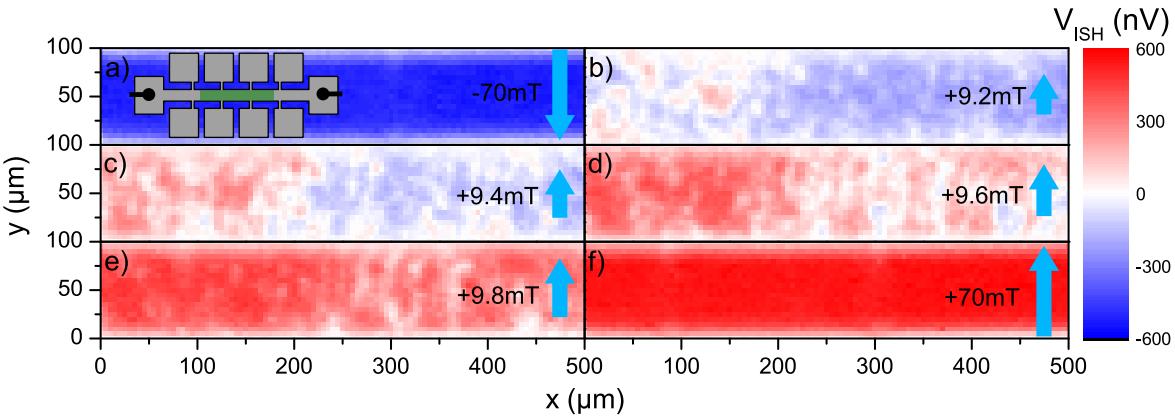

Figure 4.9: In panel **a)** the sample (#3, YIG/Pt) is homogenously magnetized and no domains are visible. Incrementally changing the magnitude of the magnetic field one can observe how the sample's magnetization starts to adjust to the new field orientation, with a domain wall moving from the left to the right side of the Hall bar (**b)-f)**)

mains [57]. These end domains easily form at the edges of a sample once the external magnetic field falls below a certain threshold that is in many cases much higher than the sample's coercive field. Since they are already partly oriented in the opposing direction they benefit the formation of the new, reversed magnetic domain. What exactly causes the domain walls to consistently move from one specific side to the other is not exactly known. The sample itself is symmetric but the contact between the normal metal and the bonding wires is not due to fabrication reasons. This could potentially explain the observed behaviour, but on the other hand if the bonding wires are responsible for the initial creation of the new magnetic domain orientation, then it is not clear why no examined sample shows a behaviour where two domain walls are moving to the center of the Hall bar from each of its two ends. Another possible explanation is that the preferred direction in which the domain wall moves is due to inhomogeneities in the magnetic field where one end of the sample resides in a slightly higher field during the reversal process than the other end. However, as the emphasis of this thesis was not on domain wall nucleation or motion this was not looked into any further.

For magnetic field values in close proximity to the coercive field (when the domain wall motion can be observed) regions of different V_{ISH} magnitude become visible within the otherwise homogeneous V_{ISH} signal. In the YIG samples (e.g., Fig. 4.9) those regions are a couple of micrometers wide. While single crystalline YIG does exhibit quite large domains [58] with lateral dimensions of several micrometers, the samples studied here are epitaxially grown thin films where much smaller domains have been reported [59, 60, 61]. A possible explanation for this difference is that the observed areas are not single magnetic domains but larger clusters of similarly oriented domains that form at rough

spots of the interface or surface of the sample.
Nevertheless, in the following these areas will still be called *magnetic domains* regardless of their true nature, since strong evidence has been found that the local magnetization orientation can be mapped with spatially resolved spin Seebeck measurements.

4.4.2 Spin Seebeck mapping resolution

One of the key parameters of a local measurement is the actual resolution at which one can resolve individual features. To quantify the resolution at which features in the thermogalvanic signal V_{ISH} can be resolved a sample is mapped close to its coercive field so that the domain patterns become visible. A small area on the Hall bar is chosen and a spin Seebeck image is recorded for different step sizes of the xyz-stage (see Fig. 4.10). The theoretical limit is again given by the refraction limit (Eq. (4.3)), although instead of the laser spot radius the radius of the heated region, which is possibly bigger by a fair amount, now enters Eq. (4.3) and sets the limit for the resolution.

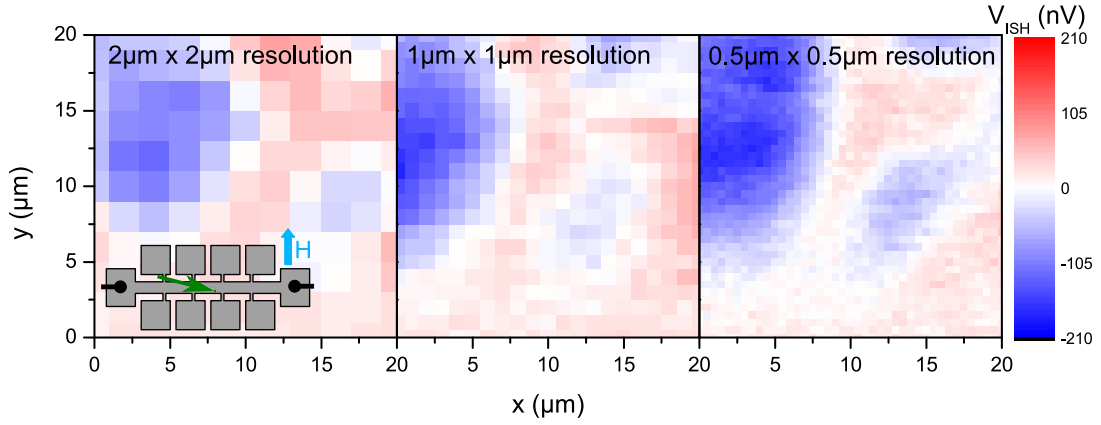

Figure 4.10: Images of a small area in the middle of the Hall bar on sample #3 (YIG/Pt) taken during a downsweep of the magnetic field at −11.4 mT. Each of the three pictures was taken with a different stepsize of the xyz-stage.

Figure 4.10 shows that while smaller features become visible up to a resolution of approximately 2 µm, even lower resolutions don't reveal new features so that it can be concluded not only that the resolution is of the order of the laser spot size (2.5 µm) but also that the region that is heated up is not much bigger than the laser spot itself. This ensures that different orientations of the magnetization can be resolved within a length of about 2.5 µm.
For future measurements this means that with spatially resolved spin Seebeck measure-

ments samples considerably smaller than the current ones (with dimensions down to few microns) could be investigated. This is particularly interesting since it has been shown before [35] that the spin Seebeck, or rather the inverse spin Hall signal V_{ISH}, scales inversely with the width of the Hall bar. This implies that the measured voltage will increase with decreasing sample dimensions. With the current laser the spin Seebeck signal V_{ISH} could therefore be increased up to about a factor of ten, which could be exploited in samples that exhibit a very small spin Seebeck signal (*cf.* Sec. 4.5) where the signal to noise ratio becomes very poor.

4.4.3 Thermal domain control

Closer inspection of the 3 images in Fig. 4.10 reveals that the texture is not exactly the same on all three images, but that the areas that yield a negative voltage V_{ISH} (blue) are actually increasing at the cost of the ones that yield a positive signal (red) with increasing resolution. Since these pictures were taken one directly after the other, the time a given position on the sample was exposed to the laser heating was also increasing.
More detailed investigations showed that the heat deposited by the laser irradiation does indeed affect the magnetic texture of the sample. This allows the magnetization to be controlled in a single measurement. For low laser powers, the magnetization texture is affected much less than for high laser power, where the laser induced magnetization manipulation can even go as far as flipping the magnetization of large parts of the sample even if only a small area was hit by the laser. Also, while this change only occurs in a magnetic field range very close to the coercive field H_{c} for low laser powers, it can be induced at magnetic fields much further away from H_{c} for higher laser powers. This leads to the conclusion that thermally assisted magnetization switching is possible in YIG/Pt where the additional heat from the laser helps to overcome the coupling between the individual magnetic moments still oriented parallel instead of *anti*parallel to the external field. This kind of behaviour has already been observed for nickel ferrite and permalloy thin films [62] and is already used in magnetic memory applications [63] but is new for YIG to our knowledge. In the first experiments (Fig. 4.11) it was shown that it is possible to selectively change the magnetization in rectangular regions on the sample. How well this process works is heavily dependent on the exact magnetic field and the laser power used. In a three step process, first an image of the sample is taken close to a coercive field at low laser power ($P \lesssim 3\,\mathrm{mW}$). In the second step the region in which the magnetization shall be switched is scanned with high laser power ($P \gtrsim 3\,\mathrm{mW}$) and/or with longer exposure to increase the time each point (x, y) is subject to the laser

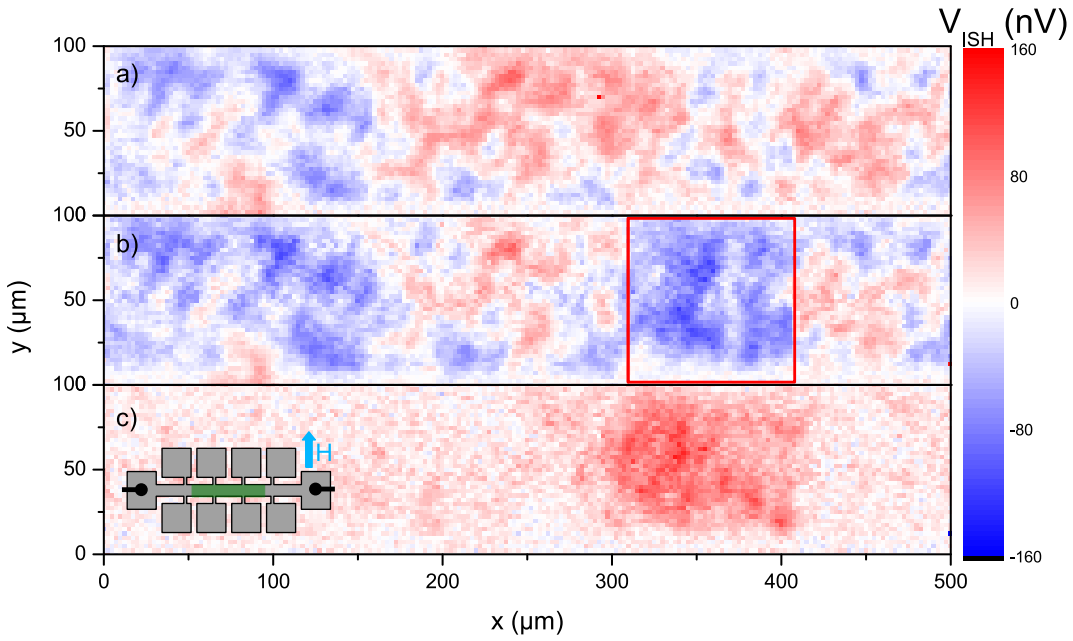

Figure 4.11: Sample #3 (YIG/Pt) is first magnetically saturated by exposing it to high (+70 mT) fields, after which the magnetic field is set to a value of −11.7 mT (the coercive field). **a)** A picture at low power ($P \approx 1\,\mathrm{mW}$) is first taken in order to minimize the thermally assisted switching at this stage. In a second step the laser is scanned across the region between $300-400\,\mu\mathrm{m}$ (red square) at higher power ($P \approx 6\,\mathrm{mW}$). **b)** Another picture at low laser power is taken afterwards, in which the treated region (red square) is already clearly visible. **c)** To get bring the laser induced magnetization switching out more clearly, the difference between panel **a)** and **b)** is taken.

heating. Finally another image of the whole sample is taken at low laser power. Low laser power is used in the first and last step to not induce, or at least minimize, laser induced changes in the magnetization texture. The region that has been treated with high laser power then becomes visible in the last image when compared to the first one. The laser induced switching of the magnetization is best visualized by plotting the difference $V_{\mathrm{ISH},1}(x,y) - V_{\mathrm{ISH},3}(x,y)$ where $V_{\mathrm{ISH},i}(x,y)$ denotes the measures spin Seebeck voltage in the i^{th} step of the above procedure. As noted above for too low laser power not all magnetic moments can be switched whereas (see also Fig. 4.12**b**) for too high laser power the region in which the magnetization switching is induced is not well defined anymore.
Following the proof of concept in Fig. 4.11, in a next step an electronic shutter was used to write shapes into the magnetization texture.
Tot this end, first a black and white image of the desired shape is made in which regions where the shutter is supposed to be opened are represented in white whereas regions where the shutter is supposed to be closed are depicted in black. The procedure is then essentially following the same steps as in the previous measurements. However, in the

second step the movement of the xyz-stage is now coordinated with the beam shutter so that the laser only reaches the samples at those positions that are depicted white in the before mentioned image.

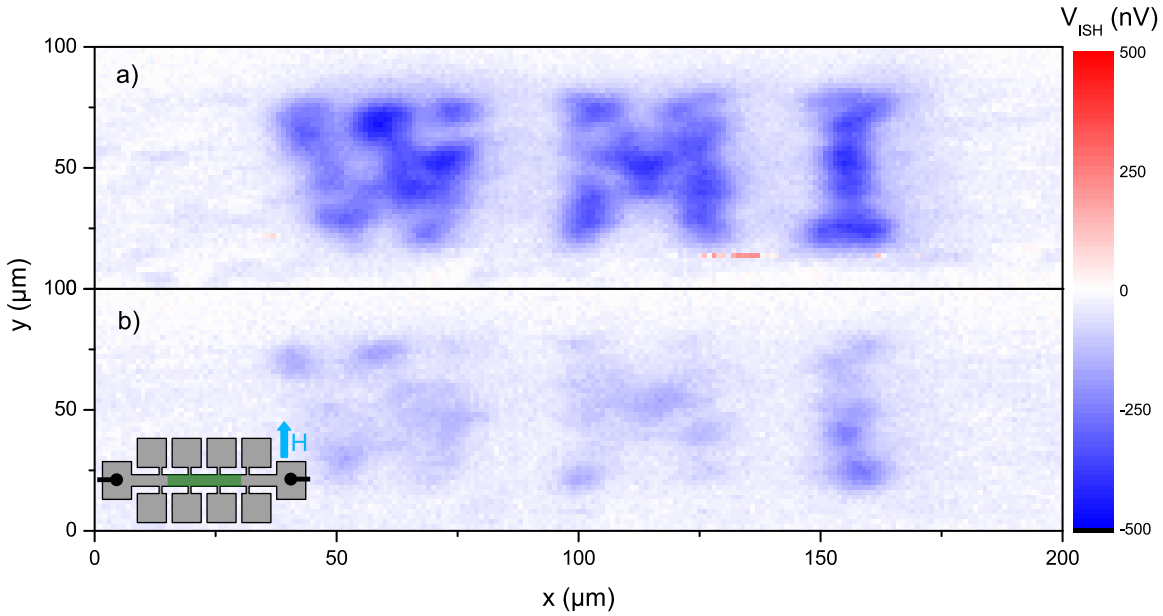

Figure 4.12: In a process similar to the one used in Fig. 4.11 one can selectively change the magnetization orientation of small regions. Here an electronic beam shutter is used to blank the laser beam selectively, thereby "drawing" a shape into the magnetization. The two images here are difference images of a measurement done on sample #3 (YIG/Pt) at two different laser powers. For both images the external field was set to $-13.7\,\mathrm{mT}$ but for **a)** a laser power of $P \approx 12\,\mathrm{mW}$ and for **b)** $P \approx 10\,\mathrm{mW}$ was used.

In Fig. 4.12 the result of this technique is shown. The quality of the reproduction of the mask image is very sensitive to both the laser power used in the different steps (especially the second one) and also to the exact magnetic field at which the process takes place. Some effort was invested into tuning those parameters but even better results with wider Hall bars, with larger room for errors, and better control over the exact laser power and magnetic field should be achieved in the future.

4.4.4 Longitudinal and transverse spin Seebeck signal

In Fig. 4.7, at the upper and lower edges of the Hall bar the V_{ISH} signal drops considerably. Due to their position and separation, one can attribute these features to the feed lines. Theses spots show a particularly interesting signal in the transverse direction (Fig. 4.13). "Transverse" hereby refers to the orientation of the electric field perpendicular to the Hall

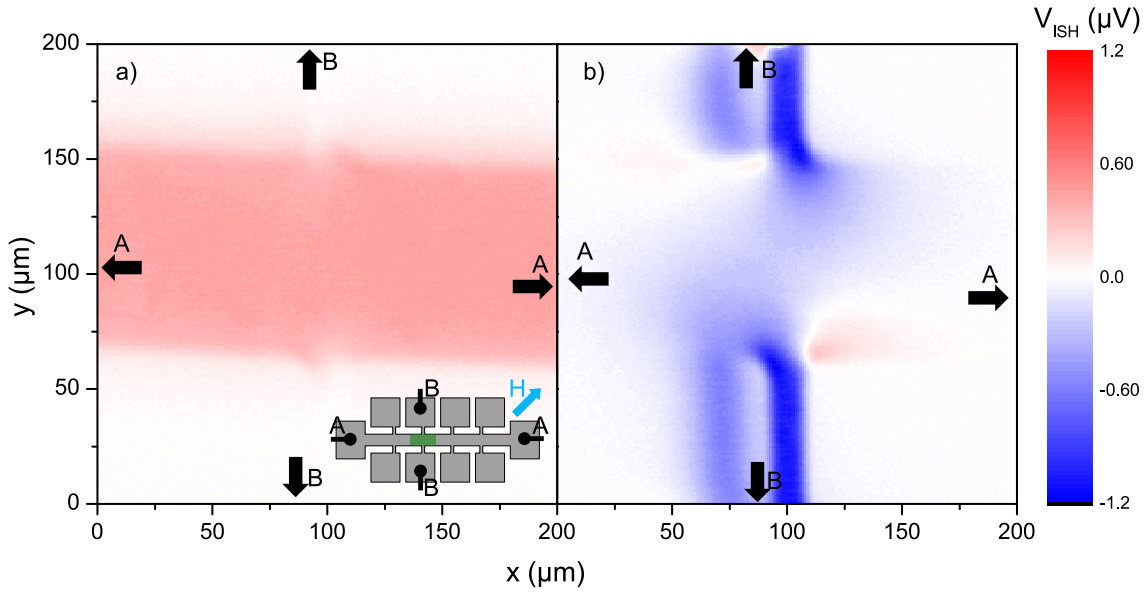

Figure 4.13: Voltage map of sample #3 (YIG/Pt). Panel **a)** shows the V_{ISH} signal obtained from the pair of contacts **A** whereas panel **b)** is an image of V_{ISH} of the same area, simultaneously recorded between the pair of contacts **B**. The influence of the transversal signal can also be seen on the edges of the longitudinal signal.

bar's body. In order to resolve this phenomenon, Fig. 4.13**b** shows a map of V_{ISH} measured along a pair of feed lines that sit opposite of each other. According to Eq. (2.35) the spin Seebeck effect should only occur if the magnetic field has a component perpendicular to the voltage measurement direction. In Fig. 4.14, however, the magnetic field was applied collinear to the measurement ($\hat{\boldsymbol{y}}$) direction. Nevertheless, a V_{ISH} signal is recorded. It is assumed that the Hall bar is not oriented exactly horizontal here, so that the magnetic field has components perpendicular to the measurement direction that make the observation of a spin Seebeck signal V_{ISH} via the inverse spin Hall effect possible.
Within the feed line the signal is homogenous but at the corners where the feed lines are connected to the main body of the Hall bar the signal not only diminishes (which is in accordance with Eq. (2.39) where a factor $1/w$ was motivated) but also splits up into two arms of different sign. This kind of behaviour is not expected since $\boldsymbol{H}$ and the sign of ΔT that determine the sign of V_{ISH} should be the same throughout the Hall bar. Due to the symmetry of the sample at this spot and the symmetry of solutions to the heat equation the change in sign can not be due to a change in the sign of the temperature difference. Additionally the change in sign also occurs exactly around the coercive field of the sample (Fig. 4.14) which was determined before. Thus this feature can probably be attributed to the YIG's magnetization that is somehow miss-oriented here. Micromagnetic experiments [64, 57, 65] show that the magnetization's orientation is indeed strongly influenced

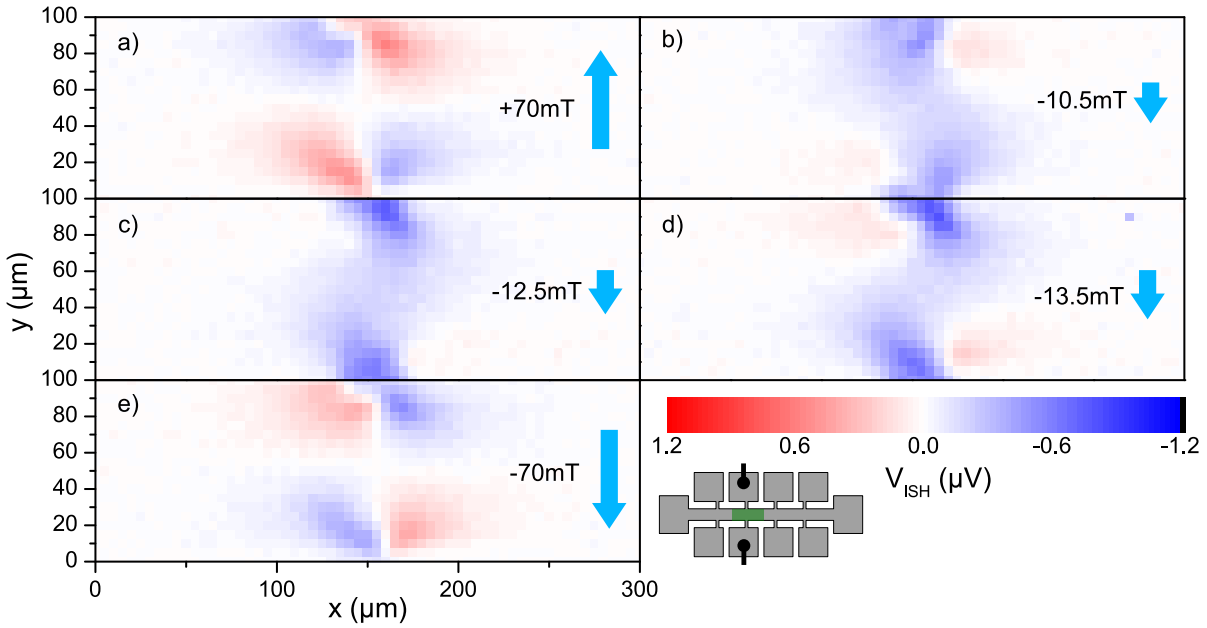

Figure 4.14: Transverse V_{ISH} signal of sample #3 (YIG/Pt) in about the same area as in Fig. 4.13 at different magnetic fields. Far away from the coercive field (**a**) a symmetric pattern is visible in the inverse spin Hall voltage. Closing in on and crossing the coercive field the different areas gradually change sign (**b,c,d**) until the pattern is reversed at the opposite of the starting field (**e**).

by edges and corners. These experiments however do not show a complete reversal of the magnetization for magnetic fields far away from the coercive field as seen in Fig. 4.13 and 4.14 but rather a slight bending of the magnetization normal to the edges. It may be noted though that the these experiments were done with much simpler ferromagnets like plain nickel or cobalt. The *ferri*magnetic nature of YIG is likely to complicate the matter.

Following the arguments just put forward, these features are attributed to the magnetization texture in combination with the geometry of the Hall bar. Further measurements need to be done to verify this claim. Since the majority of the measurements are done in the $\hat{\boldsymbol{x}}$-direction where theses features are barely visible and don not alter the V_{ISH} measurements considerably, this is not an issue for the quantitative analysis in the following.

4.5 Spin Seebeck effect in YIG/N/Pt trilayers

The results of the previous sections show that the observed voltage V_{ISH} is consistent with the predicted behaviour of the spin Seebeck effect. However, the spin Seebeck and anomalous Nernst effect depend on the magnetization orientation of the sample with respect to the direction of the temperature gradient (the F/N interface normal for the spin Seebeck effect) in exactly the same fashion (Eq. (2.8) and (2.35)). In experiment it is therefore a challenge to distinguish one from the other. In most samples presented in this thesis the electrical insulator YIG was used as the ferromagnet, such that no Nernst effect should occur. However it has been shown that a static spin polarization can be induced in normal metals in proximity to conductive ferromagnets [66, 67, 68, 69, 70]. If a static spin polarization would also occur in Pt/YIG hybrids, the spin polarized platinum could contribute an anomalous Nernst voltage to the measured signal. It has been shown ([35] supplements), however, that a possible contribution from the anomalous Nernst effect to the measured voltage V_{ISH} would be at least one order of magnitude smaller than the spin Seebeck effect voltage. This result will be confirmed at the end of this section. In order to also quantitatively resolve the anomalous Nernst issue, three samples (#4, #5 and #16) were examined, in which an additional buffer layer of either gold or copper was placed between the platinum and the YIG (Fig. 4.15). Experiments have shown that the induced magnetic proximity polarization is very small ($\approx 0.06\mu_{\mathrm{B}}$/atom) in gold [67] and in copper [71], such that for those samples Nernst effect contributions can safely be excluded.

The same setup as in Sec. 4.4 (*cf.* Fig. 4.1) has been used to measure the spin Seebeck voltage V_{ISH} on these samples. Additionally, magnetization loops have been recorded by fixing the laser spot position in the center of the Hall bar and varying the external magnetic field in a range of $\pm 60\,\mathrm{mT}$. In Fig. 4.16 it can be seen that the insertion of the nonmagnetic Au or Cu buffer layer does not qualitatively alter the V_{ISH} signal. The drastic decrease in the measured V_{ISH} magnitude is not surprising since the buffer layer effectively short circuits the inverse spin Hall voltage. This is due to the fact the spin Hall angle in copper and gold is notably smaller than the one in platinum ($\theta_{\mathrm{H}}^{\mathrm{Cu}} \approx 0$, $\theta_{\mathrm{H}}^{\mathrm{Au}} = 0.0035$, $\theta_{\mathrm{H}}^{\mathrm{Pt}} = 0.013$, see Ch. 3) so that they do not contribute inverse spin Hall voltage. To account for this one can divide the spin Seebeck voltage V_{ISH} by the samples' resistivity ρ, as it has been done in Fig. 4.16. The corresponding V_{ISH}/ρ signal magnitude only differs by a factor of about three between the individual samples. The scatter is attributed to the different absorption of the laser light by the samples and potentially different sample morphology. Additionally the spin current is further weakened by the fact that it now has to cross two instead of one interface and that further spin relaxations can occur in the buffer layer. The

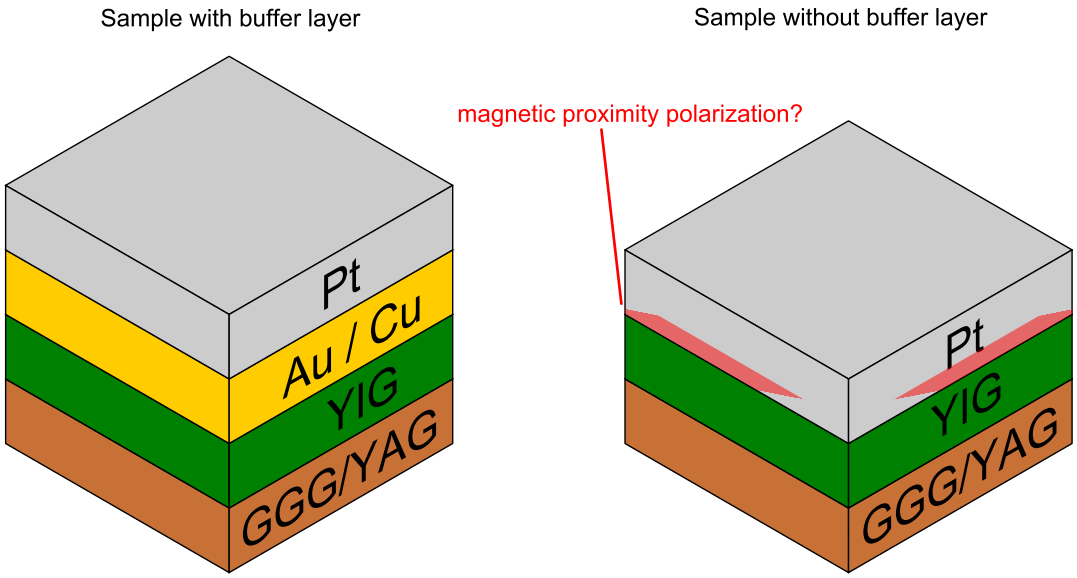

Figure 4.15: Schematic of a sample with (left) and without (right) a normal metal buffer layer between the platinum and the YIG. It has been shown that both gold and copper are not susceptible to the magnetic proximity effect. The latter could cause anomalous Nernst contributions to the measured thermo-galvanic voltage V_{ISH}. Since no magnetic proximity effect data for platinum/yttrium iron garnet bilayers have been published in literature the existence of such a phenomenon can not be excluded with certainty.

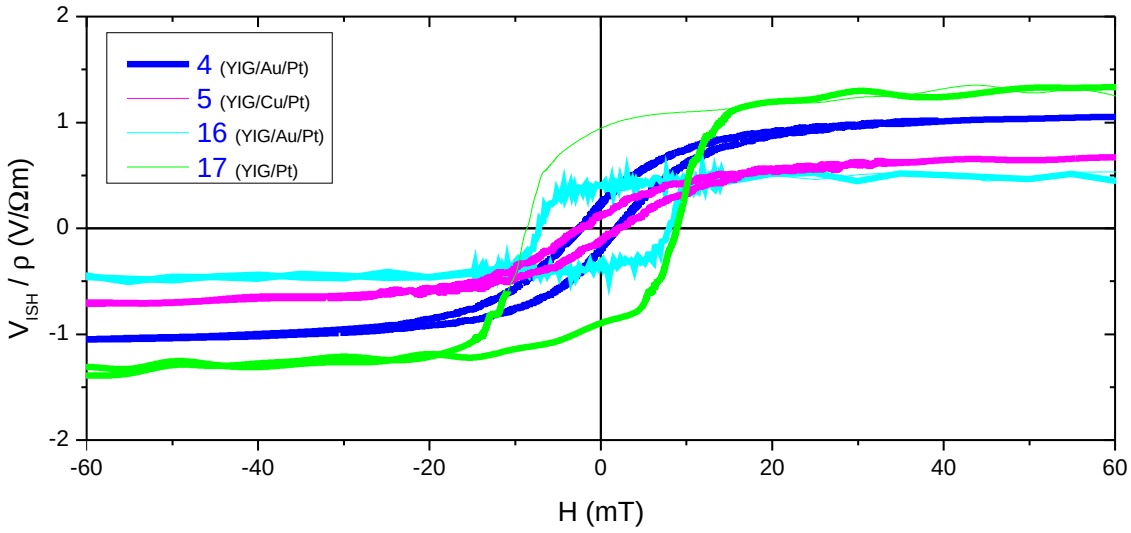

Figure 4.16: Hysteresis loop for sample #4, #5 and #16 (with buffer layer) and #17 (without buffer layer) normalized to a laser power of 10 mW and the resistivity ρ of the samples. In all four samples the spin Seebeck effect can be measured however it is weakened by the introduction of the buffer layer by a factor of about ten. The absolute values for V_{ISH} agree with each other within an order of magnitude.

latter can be described by the spin diffusion length, which is around 60 nm for gold [72] and several hundred nanometers for copper [73].
Interestingly, the coercive fields evident from Fig. 4.16 seem to shift to lower values with the introduction of the buffer layer. However, a similar behaviour is also observed on bilayer samples, so the shift in the coercive field does not seem to be induced by the buffer layer.
Additionally, one can compute the anomalous Nernst effect contribution to the measured voltage V_{ISH}, assuming that there is indeed a static magnetic proximity polarization in the platinum. Using Eq. (2.6) and using data from Sec. 5.2 ($P = 10\,\mathrm{mW} \Rightarrow \nabla T \approx 10^6\,\mathrm{K/m}$) and assuming the entire platinum thin film is magnetized (as opposed to few monolayers at the interface, reported before e.g. in [66]), with a nonrealistic large platinum Nernst coefficient of about $N \approx 1 \cdot 10^{-4}\,\mathrm{V/KT}$ [74] which has been found in a $Li_{0.9}Mo_6O_{17}$ sample at extremely low temperatures and which is among the highest Nernst coefficients found to date and orders of magnitudes larger than conventional Nernst coefficients, an anomalous Nernst effect voltage $V_{\mathrm{ANE}} \approx 2\,\mu\mathrm{V}$ is obtained. Thus several unrealistic assumptions had to be combined to obtain a V_{ANE} of the same order of magnitude as the experimental V_{ISH} data (see Fig. 4.18).
Huang *et al.* [47] claim to have observed a static magnetic polarization in Pt/YIG bilayers and put into question all results where platinum has been used as a detector for spin currents (e.g. [32]). However, these authors did not in fact directly detect the magnetic proximity polarization but used magneto transport and spin Seebeck measurements which they interpreted as evidence for induced magnetism. It can, however, be shown that the observations from their magneto transport measurements can be entirely attributed to the spin Hall magneto resistance [44], introduced in Sec. 6.2. Furthermore, Geprägs *et al.* [75] performed XMCD measurements on YIG/Pt hybrids, that showed that if there is any static magnetic proximity polarization in the platinum it is orders of magnitude smaller than in other ferromagnet/platinum bilayer hybrids (e.g. Ni/Pt). Therefore a possible anomalous Nernst effect contribution to V_{ISH} is insignificant for spin Seebeck type of experiments in YIG/Pt.
Overall, the issue of a static magnetic proximity polarization in YIG/Pt is still source of some controversy. As pointed out above, however, according to the experimental data and calculations presented above, Nernst effect contributions to the V_{ISH} signal of YIG/Pt can be ruled out.

4.6 Thermal scaling behaviour of the spin Seebeck effect

Since the spin Seebeck effect stems from a finite temperature difference at the F/N interface, which is here induced by laser heating, it is important to quantify the relation between laser power and spin Seebeck signal V_{ISH}.
In thermal equilibrium the temperature of all layers within a given sample should be equal. If now a laser beam impacts on the sample surface a fraction R of its power is reflected and subsequently causes no heating. The part that can enter the sample is partially absorbed according to the materials absorption coefficient α (see Tab. A.1). For the thin layers used in this thesis, not all laser light is absorbed within one single layer. The fraction of light that passes a specific layer of thickness d is then partially reflected and/or absorbed within the next layer and so on. Assuming an initial laser power $P_0 = P_{\mathrm{Laser}}$ just before the laser hits the sample, its decrease within each layer i with R_i and d_i can be modeled as [76]

$$P_i(z,r) = P_{\mathrm{Laser}} \left(\prod_{j=1}^{i} (1 - R_j) \right) \mathrm{e}^{-\alpha_i z - \sum_j^{i-1} \alpha_j d_j} \mathrm{e}^{-2\left(\frac{r}{a}\right)^2} \tag{4.5}$$

in cylindrical symmetry. z hereby refers to the direction normal to the layer stack and a denotes the laser spot radius (*cf.* Sec. 4.2). The reflectivity coefficients R_i are computed from the Fresnel equation [77, 51]

$$R_i = \left| \frac{n_i - n_{i+1}}{n_i + n_{i+1}} \right|^2 \tag{4.6}$$

The heat that is generated from this is directly proportional to the power density at each point (z, r) within the sample and follows [76]

$$Q_i(z,r) = -\frac{\partial P_i(z,r)}{\partial z} \frac{1}{\pi a^2} = P_i(z,r) \frac{\alpha_i}{\pi a^2}. \tag{4.7}$$

The generated heat and subsequently the sample's temperature are therefore directly proportional to the laser power P_{Laser}, as long as no additional effects (such as nonlinear absorption), come into play.
To investigate the dependence of V_{ISH} on P_{Laser} every sample is examined at magnetic fields far above[2] its coercive field, recording V_{ISH} for different laser power as determined by the filter used in the filter wheel (Fig. 4.1). For each setting of the laser power an image of an $10 \times 10\,\mu\mathrm{m}^2$ area in the center of the Hall bar is taken at both positive and negative

[2] usually $\pm 70\,\mathrm{mT}$

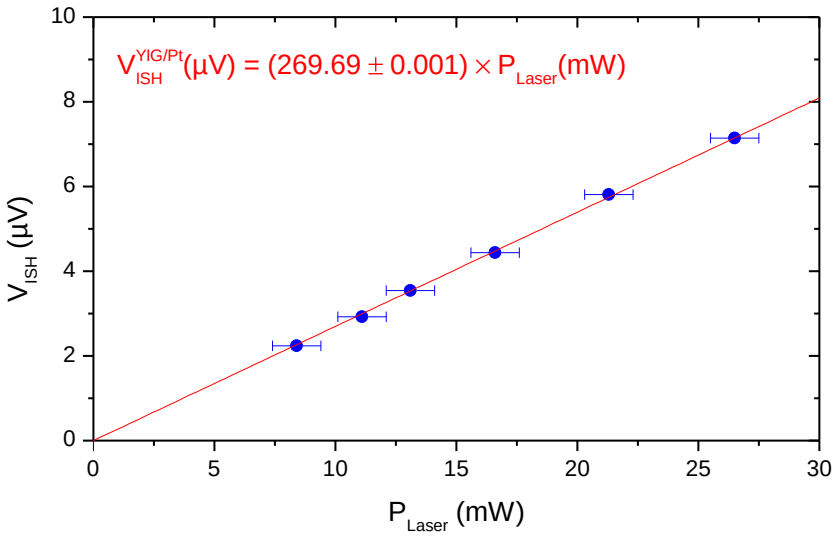

Figure 4.17: Scaling of the spin Seebeck voltage V_{ISH} with incident laser power on sample #7 (YIG/Pt). The error in the inverse spin Hall voltage for individual points varies between 2.5% for the low power measurements and around 1.5% for the high power measurements and thus is smaller than the symbol size in this figure. The error in the laser power was assumed to be 1 mW, since the power meter was heavily fluctuating at times.

magnetic field. The mean value $\sum_{x,y} V_{\mathrm{ISH}}(x,y)$ of an image is then combined with the corresponding value from the measurement at the opposing field to account for a possible offset of the data, for instance from the conventional Seebeck effect. In Fig. 4.17 a typical result of such a measurement is shown. The spin Seebeck voltage $V_{\mathrm{ISH}}(P)$ clearly follows the linear trend predicted by Eq. (4.7). By taking not only the signal from a single point on the sample but rather taking the mean over an entire area, the error in the inverse spin Hall voltage is usually very small. The determination of the laser power was however a more difficult task since one of the fibres used in the measurements showed a nonlinear response to the incident laser power so that the laser power at the sample had to be measured separately by a power meter after each set of measurements. We furthermore inserted an additional neutral density filter into the beam's path for a number of samples so that even lower powers could be achieved. The linear behaviour of the signal was also confirmed in the low power regime, as described in more detail in [78], the thesis of Kathrin Ganzhorn whom I advised.

Figure 4.18 gives an overview over the spin Seebeck voltage V_{ISH} normalized to the incident laser power P_{Laser}. Again, the laser power was not calculated but determined with help of a power meter after each measurement. Note that the normalization of V_{ISH} to P_{Laser} is only the very first step in making the spin Seebeck signals from the different

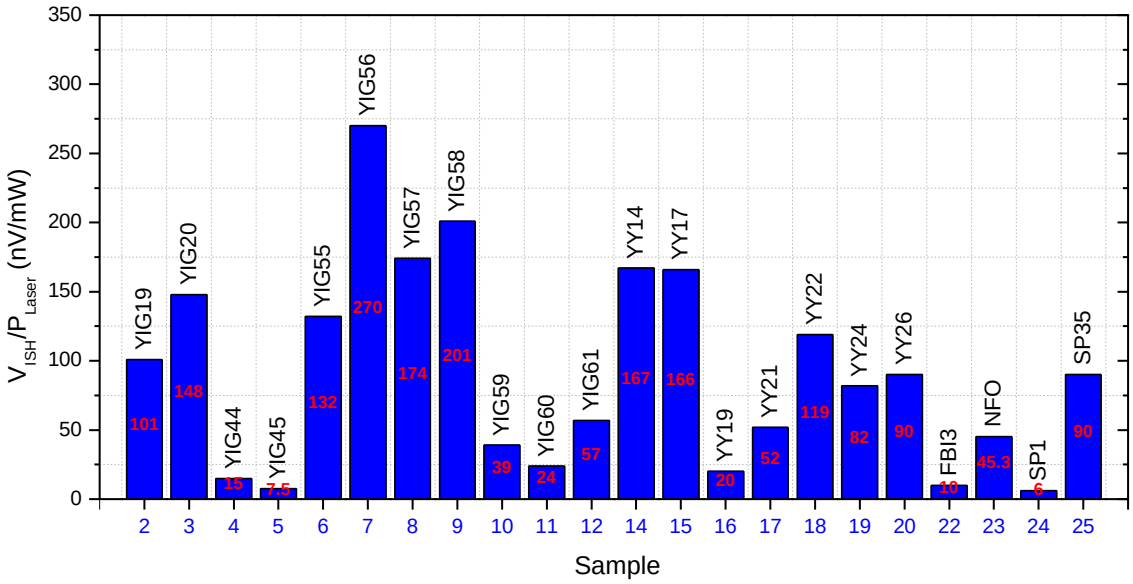

Figure 4.18: Inverse spin Hall voltage divided by laser power for all examined samples. Both the sample number (blue, x-direction) and the lab name (black) are given in combination with the absolute value $V_{\mathrm{ISH}}/P_{\mathrm{Laser}}$ (red). Since the error is too small to be resolved graphically for most samples ($\approx \pm 1\,\mathrm{nV/mW}$) it is omitted here.

samples comparable to each other. From Eq. (2.39) a normalization to ΔT is required. This however is possible only after calculating ΔT numerically as detailed in Ch. 5. The $V_{\mathrm{ISH}}/P_{\mathrm{Laser}}$ values summarized in Fig. 4.18 thus only give a qualitative picture.

On average a spin Seebeck voltage V_{ISH} of about $100\,\mathrm{nV/mW}$ was observed. Among the YIG samples, sample #4 (YIG/Au/Pt) and #5 (YIG/Cu/Pt) show the lowest ratio of $V_{\mathrm{ISH}}/P_{\mathrm{Laser}}$ whereas #7 (YIG/Pt) shows the highest value. The latter can, at least partially, be attributed to the higher resistivity of the samples with very thin Pt layers. Surprisingly, the spread for the supposedly identical samples #2 and #3 (YIG/Pt) is quite pronounced. On the other hand the thickness and composition of the substrate seems to play no major role as can be seen for the samples #3 (GGG) and #14 (YAG). The influence of the substrate is further elaborated on in Sec. 5.2.1. For all YIG/Pt samples, two major parameters in Eq. (2.39) should be the same, $\mathrm{Re}\left(g^{\uparrow\downarrow}\right)$ and θ_{SH}. The notable difference between all samples is the thickness of the individual layers that critically determines the magnitude of the spin Seebeck effect. Since the thickness does not only change the resistivity but also how strong the laser heats the samples, a more involved discussion and full calculation of ΔT is necessary, as detailed in Ch. 5. The origin of the different amplitudes is also briefly examined, in [78].

4.7 Time dependent spin Seebeck measurements

For the majority of the measurements in this thesis the laser was modulated via the chopper wheel (Fig. 4.1) at a frequency of around 850 Hz. Within the frequency range accessible using the chopper wheel ($0 - 10$ kHz) no influence of the modulation frequency onto V_{ISH} was observed.
To conduct further investigations on this matter the laser diode and its driver [35] were exchanged. The new laser diode's output power can now directly be modulated through the laser driver, controlled via an arbitrary waveform generator (AWG). By switching the modulation of the laser from mechanical to purely electrical, the laser light could be modulated with frequencies of around one kHz up to several hundred kHz. At higher modulation frequencies the laser diode's output power and the pulse shape started to degrade.
To measure $V_{\mathrm{ISH}}(t)$ while modulating the laser intensity, the laser spot position was once again fixed at the center of the sample, and a constant magnet field of 70 mT was applied. The inverse spin Hall voltage $V_{\mathrm{ISH}}(t)$ was amplified by a *Stanford Research SR560* voltage preamplifier [79] by a factor of either 1000 or 10000, depending on the measurement, and then recorded by a digitizer card [80]. The amplification has been accounted for in the data presented in the following. To monitor the laser beam's power and shape, and also to provide a trigger signal for the digitizer card, a part of the laser beam is redirected onto a photodiode (photodiode A in Fig. 4.1).
At modulation frequencies up to around 10 kHz the signal is clearly following the square wave signal from the photodiode (Fig. 4.19**a**). Since the signal to noise ratio was pretty poor, the $V_{\mathrm{ISH}}(t)$ traces in Fig. 4.19 were averaged several thousand times. For higher modulation frequencies sharp peaks at the edges of the square waves started to appear in $V_{\mathrm{ISH}}(t)$. At even higher frequencies the clear "on" and "off" levels became overlain by an oscillatory component that followed an exponential decay after every switching process. At modulation frequencies above 100 kHz it became increasingly difficult to extract the underlying spin Seebeck signal $V_{\mathrm{ISH}}(t)$ so that it eventually became impossible to extract values of the different levels (Fig. 4.19**c,e**). A phase shift between the laser light and the spin Seebeck voltage could not be observed for the frequency range $1\,\mathrm{kHz} \leq f_{\mathrm{mod}} \leq 200\,\mathrm{kHz}$.
Analyzing the signal via a Fourier transformation shows that the oscillatory component can clearly be attributed to the harmonics of the modulation frequency. The Fourier

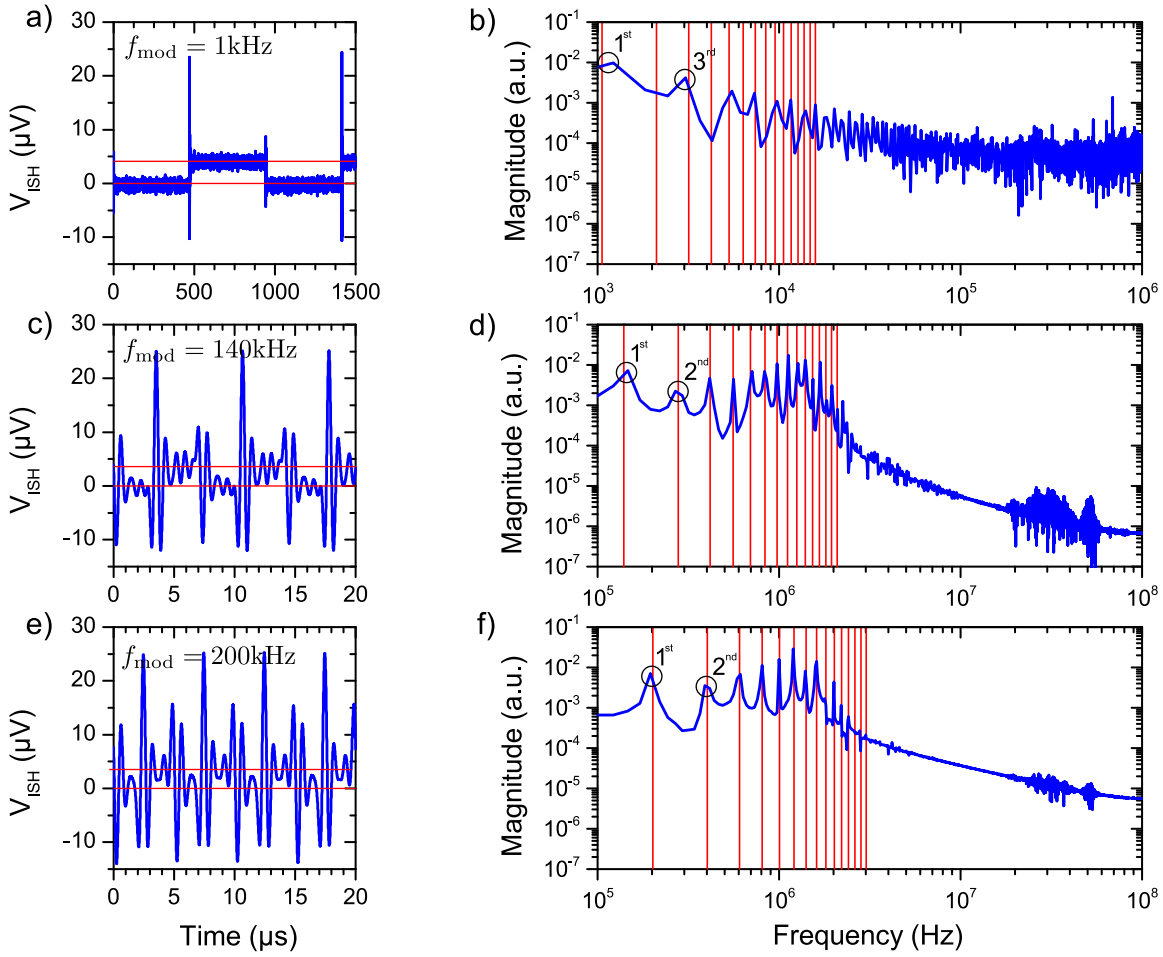

Figure 4.19: a,c,e) $V_{\mathrm{ISH}}(t)$ signal read out by the digitizer card for $f_{\mathrm{mod}} = 1\,\mathrm{kHz}, 140\,\mathrm{kHz}$ and $200\,\mathrm{kHz}$ at $P_0 = 26\,\mathrm{mW}$. For the two high frequency measurements an oscillatory component dominates the spectrum. **b,d,f)** a Fourier transform of the $V_{\mathrm{ISH}}(t)$ traces of panel **a,c** and **e**, respectively. The red lines indicate the first 15 harmonics of f_{mod}. For the 1 kHz measurement only the expected odd harmonics appear in the spectrum.

spectrum of a function $f(t)$ with periodicity T is given by [81]

$$f(t) = \frac{a_0}{2} + \sum_{k=1}^{\infty} a_k \cos(k\omega t) + b_k \sin(k\omega t) \tag{4.8}$$

where

$$\begin{aligned} a_k &= \frac{2}{T} \int_c^{c+T} f(t) \cos(k\omega t) dt \\ b_k &= \frac{2}{T} \int_c^{c+T} f(t) \sin(k\omega t) dt \end{aligned} \tag{4.9}$$

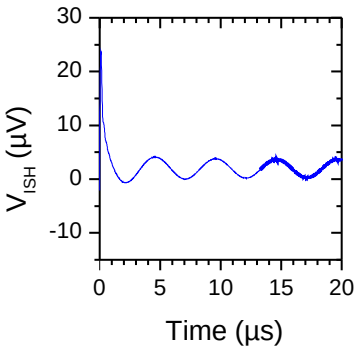

Figure 4.20: Recovered first harmonic from the $f_{\mathrm{mod}} = 200\,\mathrm{kHz}$ measurement. Its amplitude appears consistent with $4\,\mu\mathrm{V}$, coinciding with the values obtained from measurements at lower frequencies.

For a square wave signal like it is used in the measurements here

$$f(t) = \begin{cases} 1, & 0 \leq \omega t < \pi \\ -1, & \pi \leq \omega t < 2\pi \end{cases}, \quad f(t + 2\pi) = f(t) \tag{4.10}$$

the Fourier spectrum is given as

$$f(t) = \frac{4}{\pi} \sum_{k=1}^{\infty} \frac{\sin((2k-1)\omega t)}{2k-1} \tag{4.11}$$

Therefore one only expects the odd harmonics to appear in the Fourier spectrum of the experimental data. While this is true for the lower modulation frequencies (Fig. 4.19**b**) also even harmonics start to appear at the higher modulation frequencies (Fig. 4.19**d,f**). Additionally the higher harmonics become significantly more pronounced which is not what Eq. (4.11) predicts. It is a known disadvantage [82] of operational amplifiers that utilize *negative* feedback (i.e. the output signal is fed to the reversing input of the amplifier) that above a certain threshold frequency *positive* feedback can occur. The positive feedback then amplifies certain harmonics in the input spectrum as seen in Fig. 4.19**c** and **e** (or [82] Fig. 6.43).
One can attempt to recover the unperturbed signal $V_{\mathrm{ISH}}(t)$ by removing the even harmonics from the Fourier spectrum and then transform back into the time domain. However, the result (Fig. 4.20) is not good enough to allow a robust quantitative analysis.
Within the examined range of frequencies of up to 140 kHz where the "on" and "off" levels could still be distinguished, no clear dependence of V_{ISH} is found on sample #14. The combined data are shown in Fig. 4.21.

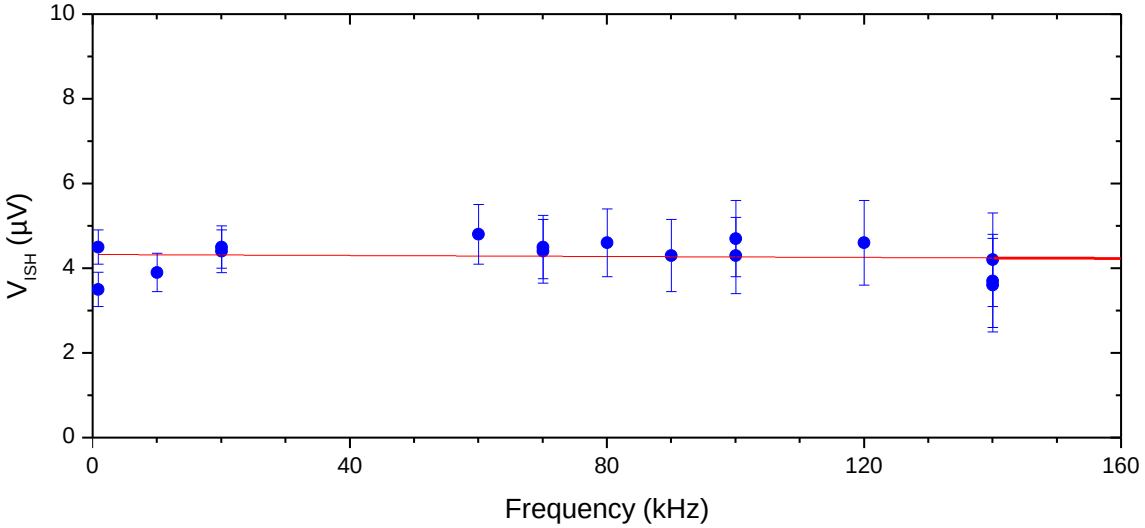

Figure 4.21: The blue dots represent the spin Seebeck voltage V_{ISH} amplitude obtained from subtracting the different voltage levels for laser on ($P_0 = 26\,\mathrm{mW}$) and laser off. The red line is a linear fit to the data. Due to the increasing harmonics contributions to V_{ISH} in the raw data, the error of this method increases drastically with the modulation frequency.

From a theoretical perspective, one would not expect a dependence of V_{ISH} on f_{mod} for $f_{\mathrm{mod}} <$ MHz. There are several processes that potentially result in a finite time constant for V_{ISH} tvia the spin Seebeck effect. The most straightforward one is the spread of heat through the sample, especially the F/N interface. Assuming that a constant spin Seebeck signal can only be achieved during steady state, one can calculate a characteristic time t_{eq} required for establishing thermal equilibrium, i.e., for a phonon to cross the F/N stack or the entire sample:

$$t_{\mathrm{eq}} \approx \frac{d}{v_{\mathrm{ph}}}. \tag{4.12}$$

Here d denotes the total length a phonon has to cross and v_{ph} is the phonon velocity given by the speed of sound in the respective material. For a lower boundary estimate it is assumed that $d = 500\,\mu\mathrm{m}$[3] and $v_{\mathrm{ph}} \geq 10^3\,\mathrm{m/s}$ (see Tab. A.1) such that $t_{\mathrm{eq}} \approx 5 \cdot 10^{-8}\,\mathrm{s}$. This is equivalent to a frequency of $f_{\mathrm{eq}} = 2 \cdot 10^6\,\mathrm{Hz}$. If one assumes that only the F/N stack ($d \approx 100\,\mathrm{nm}$) is relevant, then $f_{\mathrm{eq}} = 1 \cdot 10^{12}\,\mathrm{Hz}$.

For the spin Seebeck effect, not the phonon but the electron and magnon temperatures are relevant [9]. Assuming that the vast majority of the laser power is absorbed by phonons this energy has to be transferred to the magnon and electron populations before $T^{\mathrm{ph}} = T^{\mathrm{el}} = T^{\mathrm{m}}$ is achieved as assumed in Sec. 2.2.2. For the electrons the associated time

[3] The thickness of the samples used in this Thesis

constant $\tau_{\mathrm{ph-e}}$ can be found to usually take values of a few picoseconds [83, 84] ($f_{\mathrm{eq}} \approx 10^{12}$Hz). The associated time constant $\tau_{\mathrm{ph-m}}$ for the phonon magnon interaction is in the range of $\tau_{\mathrm{ph-m}} \approx 1 \cdot 10^{-6} \ldots 10^{-10}$s ($f_{\mathrm{eq}} = 1 \cdot 10^{6 \ldots 10}$Hz) [85, 86, 87].
In conclusion one therefore would expect that V_{ISH} is "instantaneous", at least on MHz timescales. This result is well reproduced in the data shown in Fig. 4.21. An improved setup that enables $V_{\mathrm{ISH}}(t)$ experiments on sub µs-timescales is already being worked on (*cf.* Ch. 7). In addition to a new laser that is capable of emitting µs laser pulses, a modified amplifier setup obviously will be required to avoid feedback artifacts.

5 Temperature profile numerics

It was shown in the theory part of this thesis (Ch. 2) that in order to quantitatively analyze the spin Seebeck effect, several quantities have to be determined. According to the theory developed by Xiao *et al.* [9] the parameter that is intrinsic to the spin Seebeck effect is the difference in temperature between magnons in the ferromagnet and phonons in the normal metal [9].
The question of whether this refers to the respective temperatures right at the interface or the mean value across a certain length is not trivial. The spin pumping model on which the derivation of the spin Seebeck effect by Xiao *et al.* is based on is, strictly speaking, only valid for very small volumes ($V \approx V_{\mathrm{mc}}$ see Sec. 2.2.2) in which the macrospin model is applicable. For the extended ferromagnets in this thesis it is therefore very hard to tell what temperature values to compare since, in principle, contributions from the entire ferromagnet are possible, even if the magnetic moments are far away from the interface and at a completely different temperature than the moments right at the interface. It will later be shown that the temperature difference calculated from the respective temperatures right at the interface does seem to agree better with the experimental results so that it will be assumed that ΔT does, indeed, refer to the temperature difference right at the interface.
For the original experiments performed in the longitudinal geometry [32] ΔT can straightforwardly be computed[1]. For the experimental geometry and the samples used in this thesis the same equations, however, become much more difficult to solve since not only does the dimensionality of the problem increase but also the number of layers increase and the boundary conditions are more complex. This makes the derivation of a temperature map for the different layers a very challenging task. Earlier results for the experimental geometry used in this thesis, published by Weiler *et al.* [35], used a model derived in a paper by Reichling and Grönbeck [76] who themselves where adding to a paper by Jackson *et al.* [88] to compute the temperature profile in the thin layers. While this approach

[1] Using the relation between the phonon and the magnon temperature from [9] and solving a staedy state, two layer, 1D version of Eq. (5.5) with fixed temperatures at the upper and bottom boundary of the sample. A more detailed discussion on this topic can be found in A.3.

will yield satisfactory results fur bulk-like layers[2], it is not applicable in the context of few nanometer thin films. For thin films, the thermal contact resistance comes into play and greatly influences the actual temperature distribution in the layers, which was not taken into account[3] in those earlier models. Unfortunately, thermal contact resistances for interfaces involving YIG have not been published, which complicates the problem quite a bit. In Sec. 5.2 however, models are presented by which thermal contact resistances can be computed.
Taken together, in this chapter both an experimental and a numerical approach are shown that make it possible to determine the temperature distribution in thin film heterostructures.

5.1 Experimental access to the thin film temperature

In a first step several approaches were explored to determine the temperature of the layers experimentally as accurately as possible. For the platinum, the idea was to measure the change in resistance induced by the heating of the platinum layer by the laser and relate this to the change in temperature. While it was possible to measure the change in resistance and thus calculate a mean rise in temperature for the Hall bar, calculating back on the *local* change in temperature proved to be very challenging. Different approaches to take the experimental geometry into account [35, 89] all yielded unreasonable or unphysical results.

For the YIG thin film, however, there is indeed a way to get access to its temperature. When using high enough laser power and very good focus, the local change in temperature induced by the laser irradiation can become big enough to cause a drop in the spin Seebeck signal, a behaviour one would not naively expect from Eq. (2.39). Besides the temperature difference ΔT at the F/N interface, it is not immediately apparent which quantities in Eq. (2.39) are temperature dependent and if so to what extent. The saturation magnetization M_s, the magnetic coherence volume V_mc and resistivity ρ do depend on temperature, however, if those two were the only ones that would lead to a number of problems. Up until temperatures very close to T_C, the material's Curie temperature (the temperature at which the ferromagnetism breaks down), Eq. (2.39) predicts an increasing spin Seebeck signal V_ISH, even at constant ΔT. However, the measurements in chapter

[2] One generally speaks of a bulk-like layer if its thickness is (much) larger than the phonon mean free path.

[3] The calculations by Reichling and Grönbeck are in fact taking thermal contact resistance into account but only for a single interface, while assuming continuous temperature and first derivative for the others.

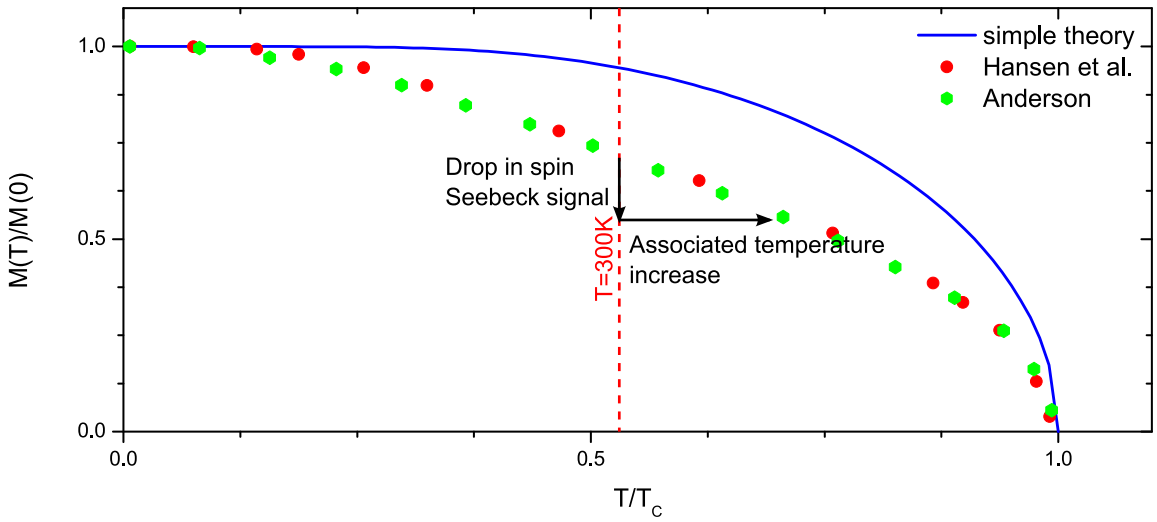

Figure 5.1: The spontaneous magnetization of YIG according to the basic mean field theory (Eq. (5.2)) approach and experimental results from Hansen *et al.* [90] and Anderson [91] (both bulk YIG). If the sample heats up, the spin Seebeck signal is expected to drop due to the decreasing spontaneous magnetization. Most likely due to the fact that YIG is not an ideal ferromagnet but rather a ferrimagnet of complex nature, the experimental magnetization data differ substantially from the simple theory. Thus, in the following only results derived from the data form Hansen *et al.* and Anderson will be given.

show no deviation from a linear dependence, which can be entirely attributed to the increasing ΔT. Therefore, in a strongly simplified and heuristic approach it is assumed that, besides $T_{\mathrm{F}}^{\mathrm{N}} - T_{\mathrm{N}}$ at the F/N interface, the only additional temperature dependence of the spin Seebeck effect can be modeled by the behaviour of saturation magnetization, since if the magnetic ordering vanishes then the spin Seebeck effect should also vanish (see Sec. 2.2.2). The temperature dependence of the material constants in Eq. (2.39) and therefore the obtained V_{ISH} signal then can be written as

$$\frac{V_{\mathrm{ISH}}(T)}{\Delta T} \propto M_{\mathrm{s}}(T), \tag{5.1}$$

unlike Eq. (2.39) where $V_{\mathrm{ISH}}/\Delta T \propto \rho(T)/(M_{\mathrm{s}}(T) \cdot V_{\mathrm{mc}}(T)) \propto \rho(T) T^{3/2} \sqrt{M_{\mathrm{s}}(T)}$. It has to be stressed again that this is a purely heuristic and very simplified approach to the complex temperature dependance of V_{ISH} and the results preseneted in the following can only be understood as an estimate to the real temperature of the YIG. However, Eq. (5.1) can be motivated if one takes into account that Eq. (2.39) was written with $T \ll T_{\mathrm{C}}$ in mind where M_{s} could be assumed constant. Then one also has to assume that $V_{\mathrm{ISH}}/\Delta T$ is basically independant of T, however, it is clear that Eq. (2.39) has to scale with $M_{\mathrm{s}}(T)$

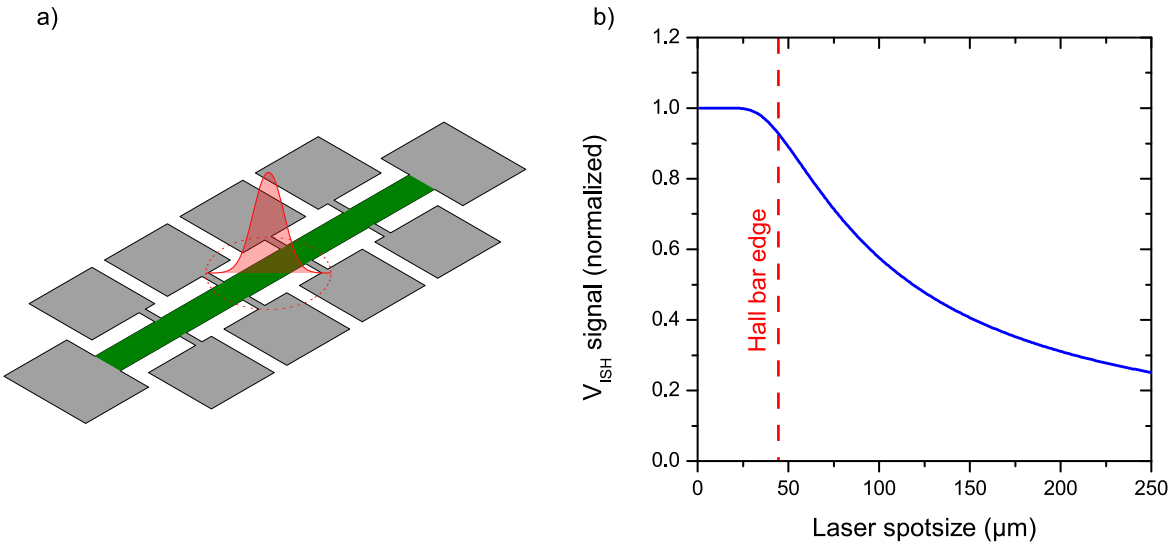

Figure 5.2: a) The detected spin Seebeck voltage is expected to stem from the area on the sample illuminated by the laser spot (only the green area is taken into account). **b)** In a simple picture, no change in the spin Seebeck signal is expected as long as the laser spot is still fully within the Hall bar irrespective of focus (see text). However, if the laser spot is only partially on the Hall bar, V_{ISH} decreases.

as no spin Seebeck signal should be observed above T_{C}.

The spontaneous magnetization of YIG is shown in Fig. 5.1. Since the locally deposited heat is inversely proportional to a^2, [4] scanning the laser spot across the Hall bar with different focus distance grants access to both the (relatively) unaltered (for a large spot radius) and lowered (for a small spot radius) magnetization.

In the mean field theory the spontaneous magnetization can be related to the temperature by [10]

$$\mathrm{Tanh}(m/t) = m, \tag{5.2}$$

with $m = M(T)/M(0)$ the spontaneous magnetization at temperature T divided by the spontaneous magnetization at zero temperature and $t = T/T_{\mathrm{C}}$. To calculate the temperature of the YIG upon laser heating, first Eq. (5.2) is numerically solved for m at a temperature of $t = 300/560$ (room temperature). An adjusted value of m is then computed by multiplying this value with the relative drop ($V_{\mathrm{ISH}}^{\mathrm{dip}}/V_{\mathrm{ISH}}^{\mathrm{plateau}}$, see Tab. 5.1) in the spin Seebeck signal V_{ISH}. Finally Eq. (5.2) is numerically solved for t at this adjusted m.

For the corresponding experiment, samples #3, #14 and #20 were chosen. Each sample was scanned in the y-direction, with incrementally increasing focus distance for each

[4] a is the beam radius. As shown in Sec. 4.2 this is directly related to the distance between lens and sample.

scan. The highest voltage obtained for each of these scans was assumed to be the value corresponding to a laser spot position in the middle of the Hall bar. Since the laser spot radius a scales linearly with the focussing distance d, the area covered by the laser spot is proportional to d^2. According to Eq. (4.7) the heat generated from the laser heating is proportional to $1/a^2 \propto 1/d^2$. Hence $V_{\mathrm{ISH}} \propto \text{area} \cdot \Delta T \propto a^2 \cdot \frac{1}{a^2}$. It can therefore be assumed that the V_{ISH} signal is only proportional to the portion A' of the laser spot radius that is within the Hall bar where a signal can be generated. Assuming the center of the laser spot is at the center of the Hall bar this portion A' is given by

$$A'(a) = \int_{-l/2}^{+l/2} \int_{-w/2}^{+w/2} \mathrm{e}^{-2\left(\frac{x^2+y^2}{a^2}\right)} dydx \tag{5.3}$$

where l denotes the length and w the width of the Hall bar. To recreate the experimental data the individual linescans have to be combined such that the focus distance of the laser spot is proportional to the laser spot radius . The curve that is obtained from the combination of the linescans therefore has to be fitted to

$$f(a, c_1, c_2, c_3) = c_3 \cdot \mathrm{Erf}\left(\frac{1}{12500\sqrt{2} \cdot \frac{c_1 - a}{c_2}}\right) \cdot \mathrm{Erf}\left(\frac{1}{1000\sqrt{2} \cdot \frac{c_1 - a}{c_2}}\right) \tag{5.4}$$

where a, c_1, c_2 and c_3 denote the laser spot radius, the center position of the plateau, a scaling factor that relates the focussing distance d to the laser spot radius and a factor to scale the (otherwise normalized) function to the actual voltage levels. All lengths are given as multiples of 1 m. The numbers stem from the integration over the width and length of the Hall bar. $\mathrm{Erf}(x)$ denotes the so called Error function which is given by $\mathrm{Erf}(x) = \frac{2}{\sqrt{\pi}} \int_0^x \mathrm{e}^{-t^2} dt$. A graphical representation of Eq. (5.4) is plotted in in Fig. 5.2.

For lower laser power densities (i.e. defocussed laser spot) where the heating of the YIG is small the experimental data fit the expected behaviour very well, as can be seen in Fig. 5.3**b**. However for higher laser power density, a drop in the otherwise flat plateau becomes apparent (Fig. 5.3**d**). The fact that the dip is not in the center of the plateau is again attributed to geometric effects from the misalignment between sample and lens. On simultaneous laser-raster reflectometry measurements it can also be seen that the dip indeed occurs when the sample's surface lies in the focal plane (and thus the beam radius is minimal). For the analysis the region with the dip is first excluded from the input data for a fit of the unperturbed plateau and then the ratio between this level and the dip's cusp is taken. This value is then used to solve for the YIG's temperature with the help of the functions derived from the data by Hansen *et al.* [90] and Anderson [91] shown in Fig. 5.1.

Table 5.1 shows the results for the three samples. At laser powers between 20 and 26 mW

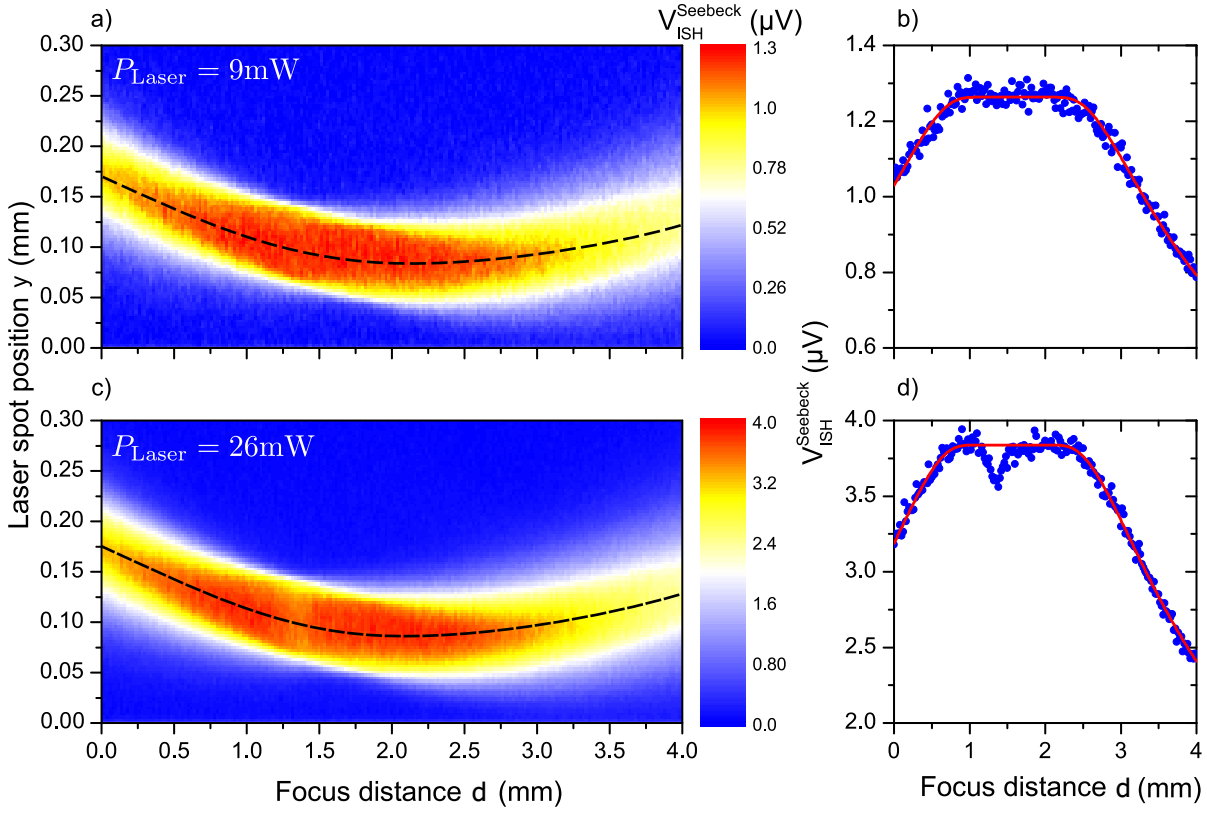

Figure 5.3: a), c) Similar to the "knife edge" procedure of Sec. 4.2 the laser is moved in the y-direction across the Hall bar of sample #3 while the spin Sebeeck voltage V_{ISH} is recorded. The banana like shape is again attributed to a slight angular mismatch between the laser and the thin film normal. The upper picture was taken at $P_{\mathrm{Laser}} = 9\,\mathrm{mW}$ whereas the lower one was taken at $P_{\mathrm{Laser}} = 26\,\mathrm{mW}$. In **c)** a drop in the V_{ISH} signal can be observed at a focussing distance of around 1.5 mm. This drop is attributed to the decreasing magnetization of the YIG (see text). **b)** and **d)** represent the data along the the dashed lines in the center of the Hall bar in **a)** and **c)**, respectively. In **b)**, where lower laser power was used the dip is only barely visible, whereas in **d)** the dip is clearly visible. Color scheme and scale were chosen to increase the visibility of the dip.

sample (@power)	plateau [μV]	dip [μV]	$\Delta T_{\mathrm{YIG}}^{\mathrm{Hansen}}$	$\Delta T_{\mathrm{YIG}}^{\mathrm{Anderson}}$	$\Delta T_{\mathrm{YIG}}^{\mathrm{theory}}$
#3 (26 mW)	3.838	3.548	35.28	32.9	64.62
#20 (20 mW)	≈1.80	1.69	28.58	25.48	56.99
#14 (24 mW)	4.055	3.803	29.11	26.05	55.3

Table 5.1: Temperature data obtained from cross-referencing the drop in the spin Seebeck signal with the drop in the YIG's spontaneous magnetization. The temperature increase is given in units of degrees K.

the YIG in all samples heats up around 30 K according to both sets of experimental magnetization data, and around 60 K for the simple mean field theoretical approach. To compare these results the values from Tab. 5.1 are now normalized to a laser power of 20 mW. Introducing $\Delta T_{\mathrm{YIG}}(i)$ that denotes the temperature increase of the YIG layer of sample i (using the Hansen *et al.* data) for a laser power of 20 mW one obtains $\Delta T_{\mathrm{YIG}}(\#3) = 27.2\,\mathrm{K}$, $\Delta T_{\mathrm{YIG}}(\#20) = 28.6\,\mathrm{K}$ and $\Delta T_{\mathrm{YIG}}(\#14) = 24.2\,\mathrm{K}$. It is now clear that sample #20 heats up slightly more than sample #14, which is consistent with the thicker platinum layer of sample #20 that absorbs much more of the laser power. Sample #3 also heats up slightly more than sample #14, although the platinum layers are equally thick. However, sample #3 is grown on a GGG substrate whereas sample #14 is grown on a YAG substrate. In Sec. 5.2.1 it will be shown that this causes a higher temperature of the sample.
Taken together, in this section it was shown that, assuming a linear relation between the spin Seebeck signal V_{ISH} and the saturation magnetization, values for the temperature increase in the YIG layer can be derived that are consistent with the sample thickness and composition. In the next section these values will be compared to results obtained from a numerical simulation of the temperature profile in the samples.

5.2 Thermal contact resistance and temperature profile simulation using ANSYS

It was laid out in Ch. 5 that it is very difficult to analytically solve the heat transfer problem for the experimental setup used in this thesis. To resolve this issue, a numerical simulation, using the 3D finite element software ANSYS, was performed to get a complete picture of the temperature distribution within the sample.
ANSYS is a commercial finite elements software and is mostly used by mechanical engineers and for fluid dynamics simulations, but also has the capability to compute heat transfer in systems. A free copy of ANSYS Academic 14 was provided by the Leibniz Rechenzentrum (LRZ) for the purpose of this study.
The simulation essentially computes the result of a number of coupled heat equations of

the form [92, 76]

$$\begin{aligned} \nabla^2 T_i - \frac{1}{k_i}\frac{\partial T_i}{\partial t} &= \frac{Q_i}{\kappa_i} \\ k_i &= \frac{\kappa_i}{\rho_i C_i} \\ -\kappa_i \left.\frac{\partial T_i}{\partial z}\right|_{\text{Interface}} &= \frac{1}{R_{\text{TH},i}} \left(T_i - T_{i+1}\right)|_{\text{Interface}} . \end{aligned} \tag{5.5}$$

Here i is the index for the individual layers, κ the thermal conductivity, ρ the density, C the heat capacity and $k = \kappa/\rho C$ the so called thermal diffusivity.
While most material parameters can be found in literature, the thermal contact resistance (TCR) R_{TH} is not so easily available. Kapitza [93] was the first to introduce and perform first calculations on this quantity (hence the TCR is also called *Kapitza resistance*). Little [94] then derived the first model for the actual computation of the TCR, called the *acoustic mismatch model* (AMM). In 1987, Swartz [95] came up with a similar approach called the *diffusive mismatch model* (DMM). Both models compute the phonon based temperature transport across an interface from the phonon density of states at each side of the interface. Little's model assumes that phonons are scattered according to Snell's law at the interface while Swartz assumes diffuse scattering. It is worth mentioning that for temperatures away from absolute zero the results obtained from these calculations often differ by factor of 2-4 from results obtained from experiments [96]. For the original purpose, calculating the TCR for a liquid Helium metal interface, experimental results also showed that the DMM gives a lower estimate while the AMM yields the upper estimate of the TCR [96, 95].
The TCR computed from the DMM is given by the following equation [97]

$$\begin{aligned} (R_{\text{TH}}^{\text{DMM}})^{-1} &= \frac{1}{4}\sum_j v_{1,j} \int_0^{\omega_c} \alpha_1^{\text{DMM}} \hbar\omega \frac{dN_{1,j}(\omega,T)}{dT} d\omega, \\ N_{i,j}(\omega,T) &= \frac{\omega^2}{2\pi^2 v_{i,j}^3 [\exp(\hbar\omega/k_B T) - 1]}, \\ \alpha_1^{\text{DMM}} &= \frac{\sum_j I_{2,j}(\omega)}{\sum_{i,j} I_{i,j}(\omega)}, \\ I_{i,j} &= v_{i,j}\hbar\omega N_{i,j}(\omega,T). \end{aligned} \tag{5.6}$$

The temperature here and in the following models is assumed to be fixed at $T = 300\,\text{K}$. For the phonon dispersion relation the Debye model [98] is generally used, with the Debye

frequencies computed from the longitudinal and transversal speed of sound v_s by

$$\omega_\mathrm{c} = (6\pi n)^{\frac{1}{3}} v_\mathrm{s} \tag{5.7}$$

with n the atomic density of the material [10]. While this approach should approximate the monoelemental layers like platinum very well, it can only be taken as a rough approximation for YIG due to its much more complex structure. Additionally, for elevated temperatures such as found in the experiments presented in this thesis, the approximation of the phonon dispersion relation by the Debye model is likely to yield imprecise results. Similarly the TCR in the AMM is computed from [96]

$$\begin{aligned}
(R_\mathrm{TH}^\mathrm{AMM})^{-1} &= \frac{1}{2}\sum_j c_{1,j}\Gamma_{1,j}\int_0^{\omega_\mathrm{c}} \hbar\omega \frac{dN_{1,j}(\omega,T)}{dT} d\omega, \\
\Gamma_{1,j} &= \int_0^{\pi/2} \alpha_{1\to2}^\mathrm{AMM}(\theta,j)\cos\theta\sin\theta d\theta, \\
\alpha_{1\to2}^\mathrm{AMM}(\theta_1,j) &= \frac{\frac{4\rho_2 v_{2,j}}{\rho_1 v_{1,j}}\cdot\frac{\cos\theta_2}{\cos\theta_1}}{\left(\frac{\rho_2 v_{2,j}}{\rho_1 v_{1,j}}+\frac{\cos\theta_2}{\cos\theta_1}\right)^2},
\end{aligned} \tag{5.8}$$

where θ_2 is linked to θ_1 by Snell's law of acoustic waves [99]

$$v_2 \sin\theta_1 = v_1 \sin\theta_2 \tag{5.9}$$

The full expression for $\alpha_{1\to2}^\mathrm{AMM}(\theta_1, j)$ was taken from [94].
As an example, the values calculated from Eq. (5.6) and (5.8) for the Pt-YIG and YIG-GGG interfaces are shown in Tab. 5.2, using the material parameters gvien in Tab. A.1.

type of resistance	Pt-YIG interface [W/m^2 K]	YIG-GGG interface [W/m^2 K]
$(R_\mathrm{TH}^\mathrm{AMM})^{-1}$	$3.31 \cdot 10^8$	$1.76 \cdot 10^8$
$(R_\mathrm{TH}^\mathrm{DMM})^{-1}$	$1.15 \cdot 10^9$	$1.02 \cdot 10^8$

Table 5.2: Thermal contact resistance for the platinum/YIG and YIG/GGG interface.

The values obtained from the AMM and DMM agree with each other within an order of magnitude, but in contrast to the metal/Helium interface, here the DMM yields the

higher TCRs. Tien and Gerner [97] note that the DMM is more applicable to rough interfaces, where diffuse scattering can occur and the AMM is better fit for epitaxially grown interfaces. Consequently the AMM value is used for all interfaces in the following. However, the values for ΔT, obtained in the following, should be considered potentially slightly too low, since the DMM yielded higher TCRs for all studied interfaces.
In addition to the YIG/Pt heterostructures, samples in which an additional metallic buffer layer was introduced between the platinum and the YIG, were also studied in this thesis. This introduces an additional type of interface where the thermal transport is dominated by the electrons of the two conductors. Following [100], the majority of electrons scatter diffusively at the interface, thus the DMM can be modified to account for the electronic transport [101]:

$$\begin{aligned}(R_{\mathrm{TH}}^{\mathrm{el}})^{-1} &= \frac{1}{2} v_1(E_{\mathrm{F}}) \Gamma_1(E_{\mathrm{F}}) \int_0^\infty E \frac{dN_1(E,T)}{dT} dE \\ \Gamma_1(E) &= \int_0^{\pi/2} \frac{v_2(E) D_2(E)}{v_1(E) D_1(E) + v_2(E) D_2(E)} \cos\theta \sin\theta d\theta\end{aligned} \tag{5.10}$$

with $D_i(E)$ and $N_i(E,T)$ the density and density of occupied states. This integral coincides with the one for the electronic heat capacity C_{e} which for a degenerate electron gas takes to from of $C_{\mathrm{e}} = (\pi^2/3) D(E_{\mathrm{F}}) k_{\mathrm{B}}^2 T = \gamma T$. Thus $R_{\mathrm{TH}}^{\mathrm{el}}$ can be written as

$$\begin{aligned}R_{\mathrm{TH}}^{\mathrm{el}} &= \frac{4(Z_1 + Z_2)}{Z_1 Z_2} \\ Z_i &= \gamma_i v_{\mathrm{F},i} T.\end{aligned} \tag{5.11}$$

For the total thermal resistance of such an interface the contributions of the phonon and electron based transport then have to be added

$$\frac{1}{R_{\mathrm{TH}}^{\mathrm{tot}}} = \frac{1}{R_{\mathrm{TH}}^{\mathrm{AMM}}} + \frac{1}{R_{\mathrm{TH}}^{\mathrm{el}}} \tag{5.12}$$

For the platinum/gold and platinum/copper interfaces the contribution from the electrons is about an order of magnitude larger ($\left(R_{\mathrm{TH}}^{\mathrm{el}}\right)^{-1} \approx 5 \cdot 10^9\,\mathrm{W/m^2\,K}$) than the contribution from the phonons which is in good agreement with experimental results [101].
Now that the TCR is computed, the temperature profile in the samples can now be simulated. In ANSYS first the geometry of the problem is set up (Fig. 5.4). The problem is modeled axially symmetric to speed up the calculations and simplify setting up the geometry, boundary conditions and loads for every sample. As a result the layers are modeled as disks of 500 µm radius. The laser heating is modeled by applying a spatially dependent heat generation function to each layer that is equivalent to the analytical expression for

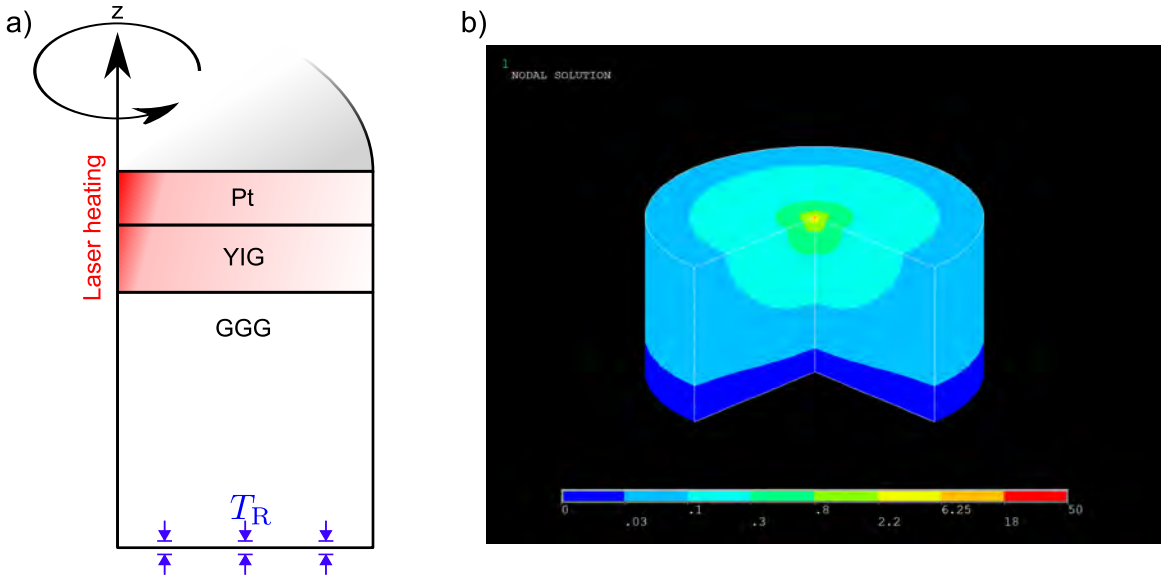

Figure 5.4: a) Depiction of the initial setup of the problem in ANSYS (not to scale). The bottom of the substrate is fixed at room temperature, whereas the other outer borders obey $\nabla T = 0$ **b)** 3/4-cut through a typical result obtained from a steady state simulation of the heat transfer problem with a logarithmic temperature scale.

the heat absorbed by the laser (Eq. (4.5) and (4.7)). As an additional boundary condition the lower end of the substrate is set to a fixed temperature of 300 K[5] (equal to room temperature). Thermal radiation is not taken into account as its contribution is negligible. A quick estimate with help of the Stefan-Boltzmann law

$$P_{\text{rad}} = \sigma A (T^4_{\text{sample}} - T^4_{\text{env}}) \tag{5.13}$$

using $\sigma = 5.67 \cdot 10^{-8} \text{W/m}^2\,\text{K}^4$, $A = 80 \cdot 1000\,\mu\text{m}^2$ and $T_{\text{sample}} \lessapprox 400\,\text{K}$ shows that less than 0.1 mW are lost due to radiation which is less then 1% of the power absorbed by the sample for typical experimental values. This was verified in a single simulation where thermal radiation was accounted for.

A typical simulation result can be seen in Fig. 5.5. Compared to the model from Reichling and Grönbeck the new simulation yields slightly higher temperature changes in the platinum and YIG layer and also shows the expected discontinuities of the temperature at the interfaces. The higher temperatures can be rationalized considering that in the ANSYS model where the TCR is taken into account the heat can not spread as easily as in the Reichling and Grönbeck model.

[5] In fact the temperature is set to 0 K since this makes the interpretation of the data easier later on. Since the temperature enters all involved equations linearly this trick does not alter the results.

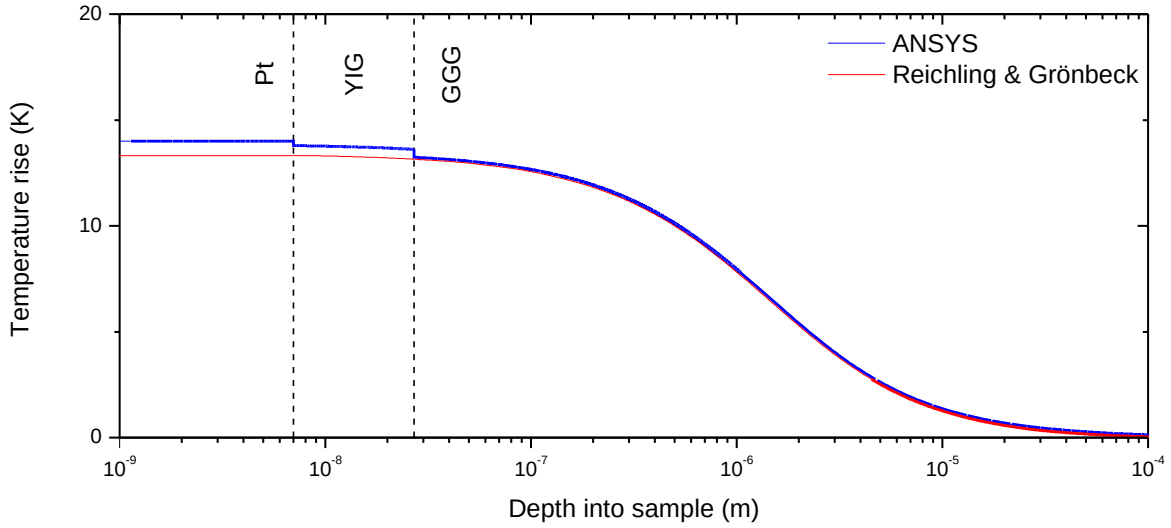

Figure 5.5: Temperature distribution of sample #3 (YIG/Pt) at $P = 10\,\mathrm{mW}$ at the center of the laser spot as given by the ANSYS (blue) and Reichling and Grönbecks (red) model (*cf.* [35]) described in this thesis. The absolute temperatures for the model from Reichling and Grönbeck agree reasonably well with the results from ANSYS ($T_{\mathrm{Pt}}^{\mathrm{R\&G}} = 13.4\,\mathrm{K}$, $T_{\mathrm{Pt}}^{\mathrm{ANSYS}} = 14\,\mathrm{K}$). The temperature distribution is, however, continuous as opposed to the jumps at the interfaces in the ANSYS result. Moreover, in the ANSYS simulation, due to the relatively low TCR (expected for epitaxial interfaces) there is still a notable temperature gradient in the YIG as opposed to a constant temperature that is expected for films with thicknesses of the same magnitude as the phonon mean free path.

sample	$\Delta T_{\mathrm{YIG}}^{\mathrm{Hansen}}$	$\Delta T_{\mathrm{YIG}}^{\mathrm{Anderson}}$	$\Delta T_{\mathrm{YIG(mean)}}^{\mathrm{ANSYS}}$	$\Delta T_{\mathrm{Pt/YIG(mean)}}^{\mathrm{ANSYS}}$	$\Delta T_{\mathrm{Pt/YIG(Interface)}}^{\mathrm{ANSYS}}$
#3	35.28	32.9	35.63	0.76	0.53
#20	28.58	25.48	28.25	1.29	0.65
#14	29.11	26.05	21.76	1.24	0.49

Table 5.3: Comparison between experimental and simulation temperature increase and difference values for the samples where sufficient data for the experimental temperature determination was available. All temperatures and temperature differences are given in units of degrees K.

Overall the results from the simulation agree well with the values directly derived from the experiment, as summarized in Tab. 5.3, especially taking into account that the margin of error for some crucial parameters such as the laser power or the V_{ISH} dip depth is around 10%. As the phonon mean free path is comparable to the platinum and YIG layer thickness, one would expect a uniform phonon temperature normal to the thin film

plane [102]. However, in the simulation, especially for the thicker YIG layers, a clear temperature gradient across the YIG film thickness can be observed. It is therefore not entirely clear a priori what value the actual temperature difference between the platinum and the YIG takes. However, introducing $\Delta T(i)$ that denotes the temperature difference between the platinum and the YIG for sample i either directly at the interface or between the respective mean values of the layers and comparing the ratios $\Delta T^{\mathrm{ANSYS}}_{\mathrm{Pt/YIG(mean)}}(\#3)/\Delta T^{\mathrm{ANSYS}}_{\mathrm{Pt/YIG(mean)}}(\#14)$, $\Delta T^{\mathrm{ANSYS}}_{\mathrm{Pt/YIG(Interface)}}(\#3)/\Delta T^{\mathrm{ANSYS}}_{\mathrm{Pt/YIG(Interface)}}(\#14)$ with the experimental $V_{\mathrm{ISH}}(P_{\mathrm{Laser}}, \#3)/V_{\mathrm{ISH}}(P_{\mathrm{Laser}}, \#14)$ from Sec. 4.6 shows that $\Delta T^{\mathrm{ANSYS}}_{\mathrm{Pt/YIG(Interface)}}$ gives a much better agreement with the values from the experiment (Sec. 4.6). As evident from Tab. 5.3, the full numerical simulation of the temperature

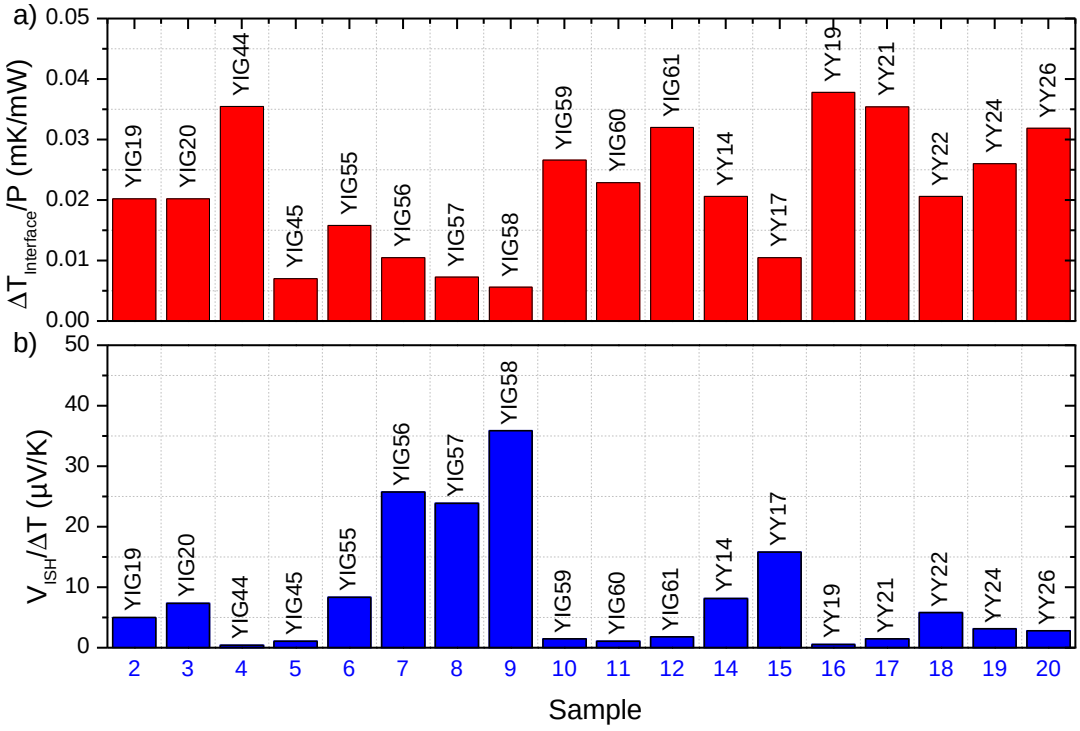

Figure 5.6: a) Temperature drop at the interface, computed with the simulation presented in Sec. 5.2, normalized to laser power $P = P_{\mathrm{Laser}}$. **b)** The spin Seebeck effect voltage V_{ISH} normalized to the temperature drop at the F/N interface. While the temperature drop scales with the thickness of the platinum layer, the V_{ISH} is apparently also influenced by other factors than temperature difference.

profiles, including the TCR, is consistent with the experimental results. Now the values for the power dependant signal from Sec. 4.6 can be normalized to the temperature difference at the F/N interface. Figure 5.6 shows that $\Delta T_{\mathrm{Pt/YIG}}$ for all samples that were simulated is within an order of magnitude. It can also be seen that $\Delta T_{\mathrm{Pt/YIG}}$ scales with the platinum layer thickness of the sample. This is consistent with Eq. (4.5) since a thicker platinum layer absorbs more laser light and thus heats up more. The two samples with

the gold buffer layer produce the highest $\Delta T_{\mathrm{Pt/YIG}}$, also because of their good absorbance and the slightly higher TCR between gold and YIG. Surprisingly the samples with high $\Delta T_{\mathrm{Pt/YIG}}$ do not necessarily produce a high spin Seebeck voltage V_{ISH}. The origin of this mismatch will be discussed in more detail in Sec. 6.1.

5.2.1 Substrate influence

As mentioned in Ch. 3, the YIG samples were grown on two different substrates, GGG and YAG. Due to severe spread in the results even for seemingly identical samples (Sec. 4.6) it is very hard to quantify the substrate's influence on the results. While there may also be contributions to the underlying processes involved in the generation of the spin Seebeck effect (e.g. influence on phonon-magnon coupling due to differing lattice mismatch) only the immediate effect of the substrate on the phonon temperature can be quantified with the simulation. To this end a stack of 10 nm platinum on 50 nm YIG was simulated for both a YAG and a GGG substrate.

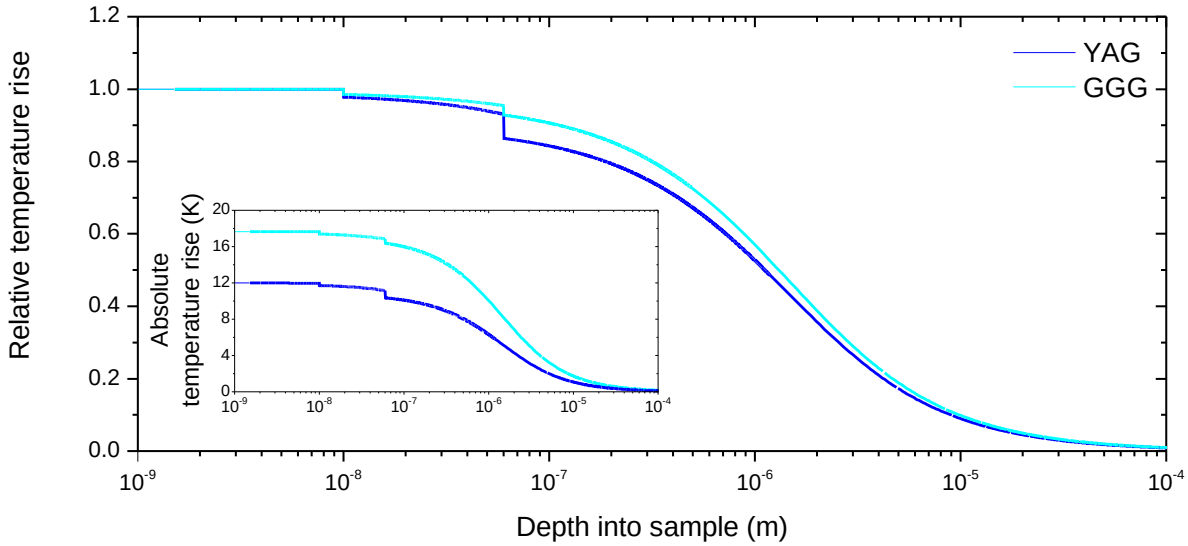

Figure 5.7: Simulation of the temperature profile of a Pt/YIG/GGG and a Pt/YIG/YAG stack arising from illumination at 10 mW laser power.

The simulation (Fig. 5.7) shows that samples grown on GGG heat up considerably more than the samples grown on YAG so that $T_{\mathrm{GGG}}(z)/T_{\mathrm{YAG}}(z) = 1.5$ for the entire F/N region. The temperature difference at the F/N interface ΔT_{i} however is almost equal: $\Delta T_{\mathrm{GGG}}/\Delta T_{\mathrm{YAG}} = 0.97$. Accordingly, the choice of the substrate is not relevant from a

spin Seebeck point of view ($V_{\mathrm{ISH}} \propto \Delta T$) since its influence on the temperature difference is smaller than other random influences, e.g. fluctuations in the laser power or growth related parameters that influence the spin Seebeck signal. However, the higher absolute temperature of the GGG samples should help determining the temperature of the YIG from experimental data as discussed in Sec. 5.1 since the additional heat should shift the YIGs temperature closer to T_{C} and thus cause a more visible dip in the spin Seebeck Signal. The experimental data, although not sufficiently statistically significant, do agree with this trend.

Another parameter that systematically changes across all samples is the thickness of the YIG layer. It takes values between 20 and around 70 nm. To quantify its influence a simulation was done for a 10 nm platinum thin film with YIG layers varying in thickness between 10 and 120 nm on a GGG substrate and additionally one sample was examined where the same platinum layer was deposited on 500 µm thick YIG bulk. According to the simulation (Fig. 5.8) the temperature difference at the F/N interface shows no film thickness dependence in the the thin film regime, but a notable decrease for the bulk sample. The absolute temperatures of the samples follow the same trend.

Comparing these findings with the data from the experiment this seems to be very

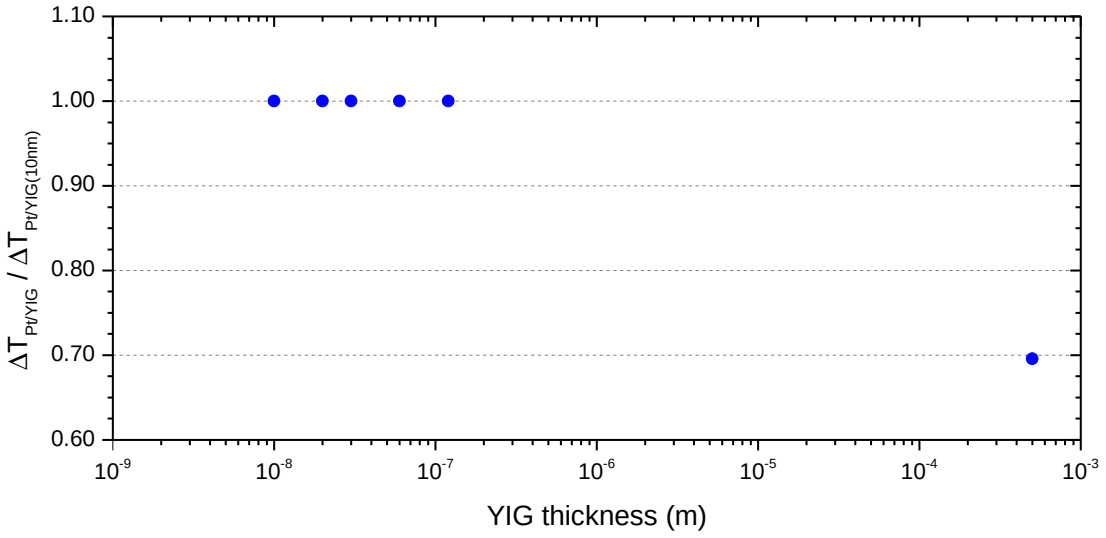

Figure 5.8: The YIG thin film samples all show the exact same temperature difference at the interface. This value decreases for the bulk YIG sample. Note that here the boundary conditions are slightly different since the temperature sink at the backside of the sample is now directly connected to the YIG.

reasonable. Neglecting the different YIG thicknesses, the samples #2, #3, #14 and #18 (7 nm platinum) all show about the same spin Seebeck signal. This is also true for sample #10 and #17 ($\approx$ 20 nm platinum), and furthermore agrees well with earlier studies on

this subject [78].

Taken together, it was shown in this chapter that the experimental data and the simulation presented in this thesis have been shown to agree well with another. The simulation could account for the thermal contact resistance between the individual layers of the samples and thus now provides the temperature difference at the ferromagnet/normal metal interface, which was not available from previous models. With this an important step for the qualitative analysis of the results in Sec. 4.6 has been done.

6 Spin currents across interfaces

The spin Seebeck effect is just one of a number of effects in which (pure) spin currents play an important role. In this chapter, an attempt is made to give a quantitative interpretation of the spin Seebeck measurement results obtained in this thesis, followed by a comparison to results obtained from spin pumping and spin Hall magneto resistance. The latter two effects also deal with spin currents at interfaces. A comparison of the individual theories shows that one can potentially predict the strength of every single effect from the results of a measurement of any one of the three. The experimental data support this result. Thus a unified description of spin angular moment transport across interfaces appears possible.

6.1 Spin Seebeck data analysis

In Ch. 2 a theory for both the spin Seebeck effect and the inverse spin Hall effect (that makes the experimental detection of the former possible) was presented. This theoretical model then was modified and extended (Eq. (2.39)) to account for the results from the experiments presented in Sec. 4.6.As discussed in Ch. 5, the temperature profile in multilayer thin film stacks can be numerically computed. Thus, one can now quantitatively compare spin Seebeck theory and experiment. Using Eq. (2.39)

$$V_{\mathrm{ISH}} = \frac{\rho\theta_{\mathrm{H}} e\gamma \mathrm{Re}(g^{\uparrow\downarrow}) k_{\mathrm{B}}}{\pi M_{\mathrm{s}} V_{\mathrm{mc}}} \frac{\Delta T'}{w} \frac{a^2\pi}{2}$$

with $\theta_{\mathrm{H}} = 0.013$ [46], $\gamma = 1.89 \cdot 10^{11}\,\mathrm{Hz/T}$ [45], $\mathrm{Re}(g^{\uparrow\downarrow}) = 4 \cdot 10^{18}\,\mathrm{m}^{-2}$ [103], $M_{\mathrm{s}} = 129\,\mathrm{kA/m}$ [45], $V_{\mathrm{mc}} = (5.4\,\mathrm{nm})^3$ [29], $a = 2.5\,\mu\mathrm{m}$ and $w = 80\,\mu\mathrm{m}$ with the appropriate ρ and $\Delta T'$ (*cf.* CH. 5) for the individual samples in Eq. (2.39)

$$V_{\mathrm{ISH}} = \frac{\rho\theta_{\mathrm{H}} e\gamma \mathrm{Re}(g^{\uparrow\downarrow}) k_{\mathrm{B}}}{\pi M_{\mathrm{s}} V_{\mathrm{mc}}} \frac{\Delta T'}{w} \frac{a^2\pi}{2}$$

one obtains V_{ISH} values in the order of 100 pV, as shown in Fig. 6.1. This is considerably smaller than the nanovolt values obtained from the experiment (Sec. 4.6). In other words a fudge factor of about 400 has to be used for the theoretical values to agree with the experimental results.

Looking at possible sources of this mismatch it becomes clear that almost every parameter

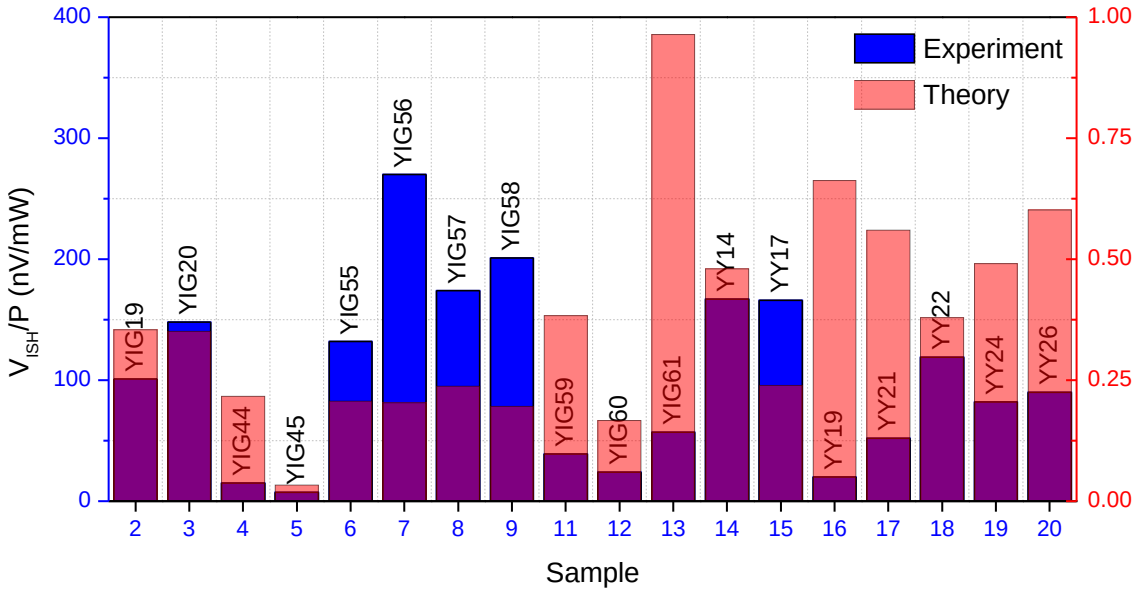

Figure 6.1: Comparison between experimental (blue) and theoretical (red) values for the spin Seebeck signal at 1 mW laser power (see text).

in Eq. (2.39) is only known up to a factor of around two or not even within an order of magnitude as in the case of V_{mc}. Revised parameters may therefore be necessary to bring theory and experiment into satisfactory agreement. In Sec. 6.2, it will be shown that a much higher spin mixing conductance and spin Hall angle (which would improve the agreement between theory and experiment) can also be found in other experiments. It should be noted though that these very high values for the spin Hall angle and especially the spin mixing conductance differ from previously published and well established data, such as the ones used above. This will be discussed in more detail in the associated section.

In the discussion so far the thickness t_{Pt} of the platinum layer was not explicitly taken into account (except for the simulation of the temperature difference at the F/N interface, and possibly encoded in the resistance of each sample). To check if the V_{ISH} results are also directly influenced by t_{Pt}, the experimental values are divided by $\Delta T'$ calculated in detail in Ch. 5 and ρ, and then plotted as a function of the respective platinum layer thickness. Figure 6.2 shows the result. If Eq. (2.39) would account for all contributions

then

$$\frac{d}{dt_{\mathrm{Pt}}}\left(\frac{V_{\mathrm{ISH}}}{\Delta T'\rho}\right) = 0, \tag{6.1}$$

which clearly is not consistent with experiment. For the following more detailed analysis,

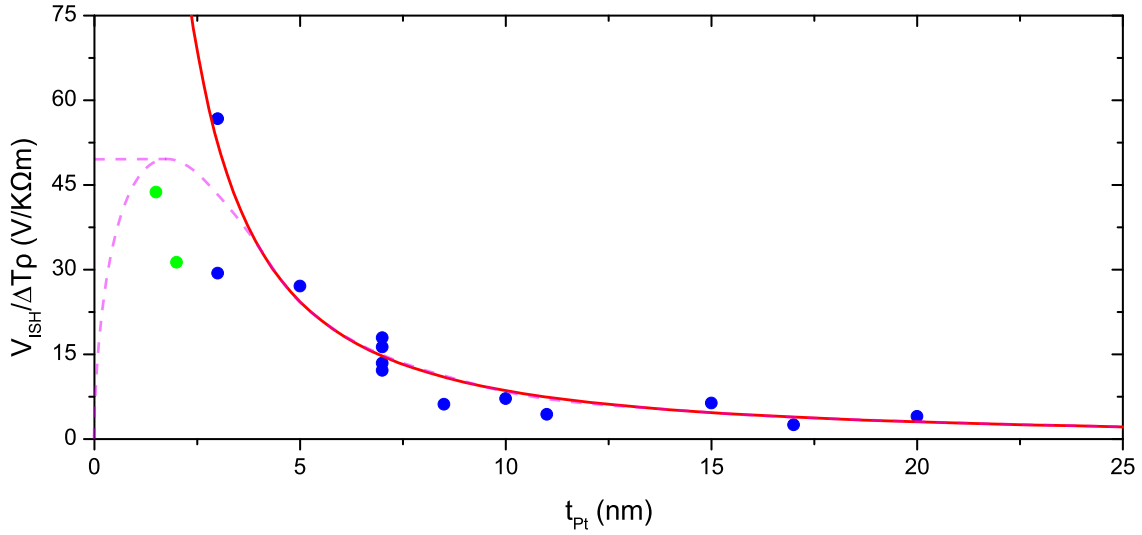

Figure 6.2: Plot of the inverse spin Hall voltage V_{ISH} divided by the two quantities known to be a function of the platinum layer thickness (ΔT, ρ) over t_{Pt}. The red line is a fit of the assumed $t_{\mathrm{Pt}}^{-3/2}$ dependence of the inverse spin Hall voltage for the thicker samples, while the dashed lines are supposed to give an idea of the possible behaviour for very thin platinum films, which are marked green here.

samples #16, #4 and #5 are disregarded since their behaviour is likely to be different due to the additional buffer layer between the platinum and the YIG. For reasons that will become apparent during the course of this and the next chapter also samples with a platinum layer thickness of less than 3 nm are not taken into account[1]. Even without these restrictions, Fig. 6.2 shows that Eq. (6.1) is *not* obeyed but that the experimental data rather follow

$$V_{\mathrm{ISH}} \propto \frac{1}{(t_{\mathrm{Pt}})^{\alpha}}, \ \alpha > 0. \tag{6.2}$$

A proper fit of the experimental data to Eq. (6.2) yields $\alpha = 1.36 \pm 0.22$. It is now assumed that $\alpha = 3/2$ in good agreement with the fit and for reasons that will become clearer in the next section.

It is important to note that Fig. 6.2 quite clearly indicates $V_{\mathrm{ISH}} \propto t_{\mathrm{Pt}}^{-\alpha}$ is only valid for large t_{Pt}. For $t_{\mathrm{Pt}} \leq 3\,\mathrm{nm}$ a constant or even decreasing V_{ISH} is observed.

[1] $\lambda_{\mathrm{Pt}} \approx 1 - 3\,\mathrm{nm}$

Such a behaviour can be understood when one compares the derivation of the spin Seebeck signal (Eq. (2.39)) to that of the *spin Hall magneto resistance*[2] and the signal obtained from spin pumping [18]. In the latter two, the spin accumulation $\boldsymbol{\mu}_\mathrm{s}$ in the platinum layer is taken into account by solving the spin diffusion equation

$$\frac{\partial \boldsymbol{\mu}_\mathrm{s}}{\partial t} = D_\mathrm{N} \Delta \boldsymbol{\mu}_\mathrm{s} - \frac{1}{\tau_\mathrm{sf}} \boldsymbol{\mu}_\mathrm{s} \tag{6.3}$$

where D_N denotes the normal metal diffusion constant and τ_sf the spin-flip time. Since Eq. (2.39) is derived using a modified version of the spin pumping mechanism [9] it appears natural that the spin accumulation has to be taken into account for the spin Seebeck effect as well, resulting in a behaviour as depicted by the dashed lines in Fig. 6.2. The upper dashed line outlines the trend of the established spin pumping theory (Eq. (6.16)) while the lower one gives the trend of the spin Hall magneto resistance.
With that in mind a *heuristic* correction parameter can now be constructed by plotting the ratio of $V_\mathrm{ISH}^\mathrm{th}/V_\mathrm{ISH}^\mathrm{exp}$ (the ratio of the the results from Eq. (2.39) to the experimental V_ISH results from Ch. 4.6) over t_Pt in order to fit the exponent of the platinum thickness dependence (Fig. 6.3).

Using the correction function obtained by this method, Eq. (2.39) transforms to

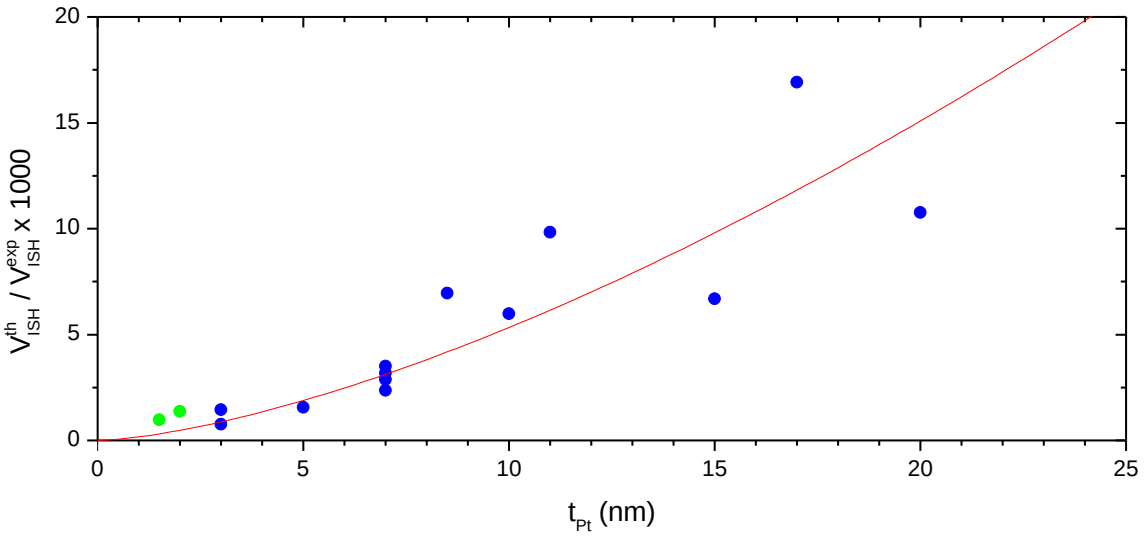

Figure 6.3: Plot of the ratio between the signal obtained from Eq. (2.39) and the experimental values as a function of the platinum layer thickness. The green dots once again mark samples with $t_\mathrm{Pt} < 3\,\mathrm{nm}$ which might not be within the validity limit of the approach taken in this chapter.

[2] Nakayama, Althammer *et al.*, unpublished. See also Ch. 6.2

$$V_{\mathrm{ISH}} = \frac{\rho\theta_{\mathrm{H}} e\gamma \mathrm{Re}(g^{\uparrow\downarrow}) k_{\mathrm{B}}}{\pi M_{\mathrm{s}} V_{\mathrm{mc}}} \frac{\Delta T'}{w} \frac{a^2\pi}{2} \cdot \frac{\bar{\lambda}}{t_{\mathrm{Pt}}^{3/2}} \tag{6.4}$$

where the correction factor takes a value of $\bar{\lambda} = 1.87 \cdot 10^{-10}\,\mathrm{m}^{3/2}$. With the exception of the two samples with extremely thin platinum layers (marked in green) this improves the agreement between theory and experiment by a factor of four (see Fig. 6.4) compared to the simple correction with a uniform fudge factor. It has to be stressed again that the

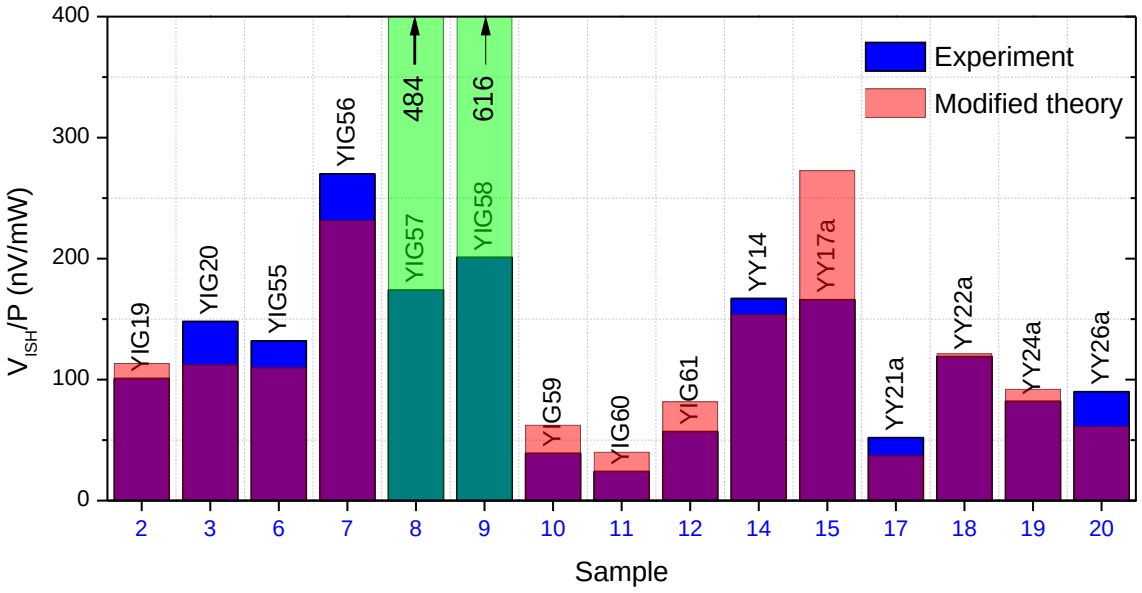

Figure 6.4: Plot of the experimental and modified theoretical values (same scale). The two green bars indicate the two samples with very thin platinum films where the error between the approximation and the real behaviour becomes very large.

exact scaling behaviour of the spin Seebeck effect with the platinum layer thickness is not known and that the approach taken here is only heuristic. more precisely, both the absolute value of the correction factor $\bar{\lambda}$ and the proposed dependence $t_{\mathrm{Pt}}^{-3/2}$ are purely heuristically motivated to this point.

6.2 Comparison of spin Hall magneto resistance and spin Seebeck effect

Following an early report by Weiler *et al.* [35], both Althammer *et al.* [44] and Nakayama *et al.* [104] independently discovered a new type of magneto resistance that is induced through conversion of a charge current into a spin current and subsequent reconversion to

a charge current in insulating ferromagnet/normal metal hybrid structures via the spin Hall and inverse spin Hall effect (Sec. 2.2). Hence, the effect was baptised "spin Hall magneto resistance" (SMR).

More precisely, in a SMR experiment, a magnetic field is applied perpendicular to a charge current in the normal metal. This induces a spin current perpendicular to both the charge current and the magnetic field via the spin Hall effect. Depending on the spin current's spin polarization $\boldsymbol{\sigma}$ and the magnetization direction $\boldsymbol{m}$ of the underlying, electrically insulating ferromagnet, this spin current can either be absorbed ($\boldsymbol{\sigma} \perp \boldsymbol{m}$) by the ferromagnet or reflected ($\boldsymbol{\sigma} \parallel \boldsymbol{m}$) at the F/N interface, since angular momentum can either be transferred into the ferromagnet or not. The part of the spin current that is reflected at the interface is then reconverted to a charge current through the inverse spin Hall effect. This leads to additional contributions to the original charge current J_C that can be expressed in terms of changes in the transverse and longitudinal resistances [44]

$$\rho_\mathrm{long} = \rho_0 + \rho_1 m_\mathrm{t}^2 \tag{6.5}$$

$$\rho_\mathrm{trans} = \rho_2 m_\mathrm{n} + \rho_3 m_\mathrm{j} m_\mathrm{t}. \tag{6.6}$$

Here m_j, m_t and m_n denote the projection of the magnetization onto the axes j, t and n (Fig. 6.5) while $\rho_1 = -\rho_3$ according to the theory (Eq. (6.7)).

The SMR signal (called SMR amplitude in the following) is commonly expressed in terms of the ratio $\Delta\rho/\rho$ which is usually of the order of 10^{-4}. The experiments done by Althammer *et al.* [44] were conducted in the same YIG/Pt (and YIG/(Au/Cu)/Pt) samples that were studied for the spin Seebeck measurements presented in Ch. 4. Interestingly, samples with large SMR effect (large ρ_1/ρ_0) also showed large spin Seebeck signals V_ISH. To quantify these observations, the theory of the spin Seebeck effect and the spin Hall magneto resistance have to be compared.

Introducing the spin diffusion length in platinum λ_Pt, the SMR amplitude can be written as [104]

$$\frac{\Delta\rho}{\rho} = \frac{-\rho_1}{\rho_0} = \frac{\theta_\mathrm{H}^2 \frac{2\lambda_\mathrm{Pt}^2 \rho_\mathrm{Pt}}{t_\mathrm{Pt}} \frac{e^2}{h} \mathrm{Re}(g^{\uparrow\downarrow}) \tanh^2\left(\frac{t_\mathrm{Pt}}{2\lambda_\mathrm{Pt}}\right)}{1 + 2\lambda_\mathrm{Pt}\rho_\mathrm{Pt}\frac{e^2}{h}\mathrm{Re}(g^{\uparrow\downarrow}) \coth\left(\frac{t_\mathrm{Pt}}{\lambda_\mathrm{Pt}}\right)}. \tag{6.7}$$

This theory can be fitted to the data obtained from measurements on samples #2, #3, #6, #7, #8, #9, #10, #11, #12, #14, #15, #17, #18, #19 and #20 assuming $\rho_\mathrm{Pt} = 400\,\mathrm{n\Omega m}$, $\lambda_\mathrm{Pt} = 1.3\,\mathrm{nm}$, $\theta_\mathrm{H} = 0.074$ and $\mathrm{Re}(g^{\uparrow\downarrow}) = 1.14 \cdot 10^{22}\,\mathrm{m}^{-2}$ (Fig. 6.6). Note that the values for the spin Hall angle and spin mixing conductance obtained here differ substantially from the previously published values that were used throughout the rest of this thesis. However, using these values for the calculation of the spin Seebeck signal in Eq. (2.39) brings the data to an agreement within a factor of 40, which is considerably

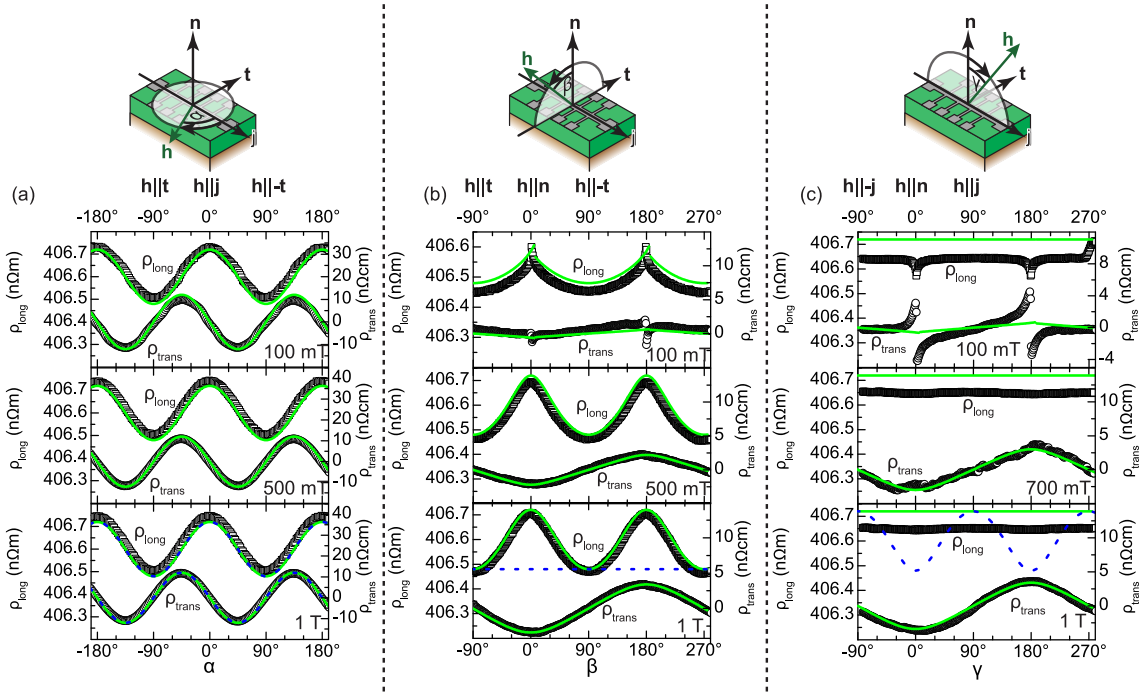

Figure 6.5: Figure taken from [44]. SMR measurements of sample #3 at $T = 300\,\mathrm{K}$ at an external magnetic fields of $\mu_0 H_{\mathrm{meas}} = 1000,\ 500,\ 100\,\mathrm{mT}$ ($\mu_0 H_{\mathrm{meas}} = 1000,\ 700,\ 100\,\mathrm{mT}$ for (c)). The green line represents a fit of the data to the model given in Eq. (6.5) and (6.6). The dashed blue line indicates the behaviour expected for *anisotropic magneto resistance*.

better than what was found using the literature values. It is important to stress that this does not change the observed t_{Pt} dependence of the spin Seebeck signal (*cf.* Fig. 6.2), but only (drastically) alters the value of the correction factor $\bar{\lambda}$. Due to a non-trivial relation between the individual parameters in Eq. (6.7) the obtained values for the spin Hall angle and spin mixing conductance have a very high uncertainty, which for the latter is in the order of several magnitudes. Therefore the better agreement between the spin Seebeck theory and the experimental data should be treated cautiously.

Since

$$\lim_{t_{\mathrm{Pt}}\to\infty} \tanh(c \cdot t_{\mathrm{Pt}}) = \lim_{t_{\mathrm{Pt}}\to\infty} \coth(c \cdot t_{\mathrm{Pt}}) = 1,\ c > 0$$

one finds that

$$\lim_{t_{\mathrm{Pt}}\to\infty} \frac{\theta_{\mathrm{H}}^2 \frac{2\lambda_{\mathrm{Pt}}^2 \rho_{\mathrm{Pt}}}{t_{\mathrm{Pt}}} \frac{e^2}{h} \mathrm{Re}(g^{\uparrow\downarrow}) \tanh^2\left(\frac{t_{\mathrm{Pt}}}{2\lambda_{\mathrm{Pt}}}\right)}{1 + 2\lambda_{\mathrm{Pt}}\rho_{\mathrm{Pt}} \frac{e^2}{h} \mathrm{Re}(g^{\uparrow\downarrow}) \coth\left(\frac{t_{\mathrm{Pt}}}{\lambda_{\mathrm{Pt}}}\right)} = \lim_{t_{\mathrm{Pt}}\to\infty} \frac{\theta_{\mathrm{H}}^2 \frac{2\lambda_{\mathrm{Pt}}^2 \rho_{\mathrm{Pt}}}{t_{\mathrm{Pt}}} \frac{e^2}{h} \mathrm{Re}(g^{\uparrow\downarrow})}{1 + 2\lambda_{\mathrm{Pt}}\rho_{\mathrm{Pt}} \frac{e^2}{h} \mathrm{Re}(g^{\uparrow\downarrow})} \propto \frac{1}{t_{\mathrm{Pt}}}. \tag{6.8}$$

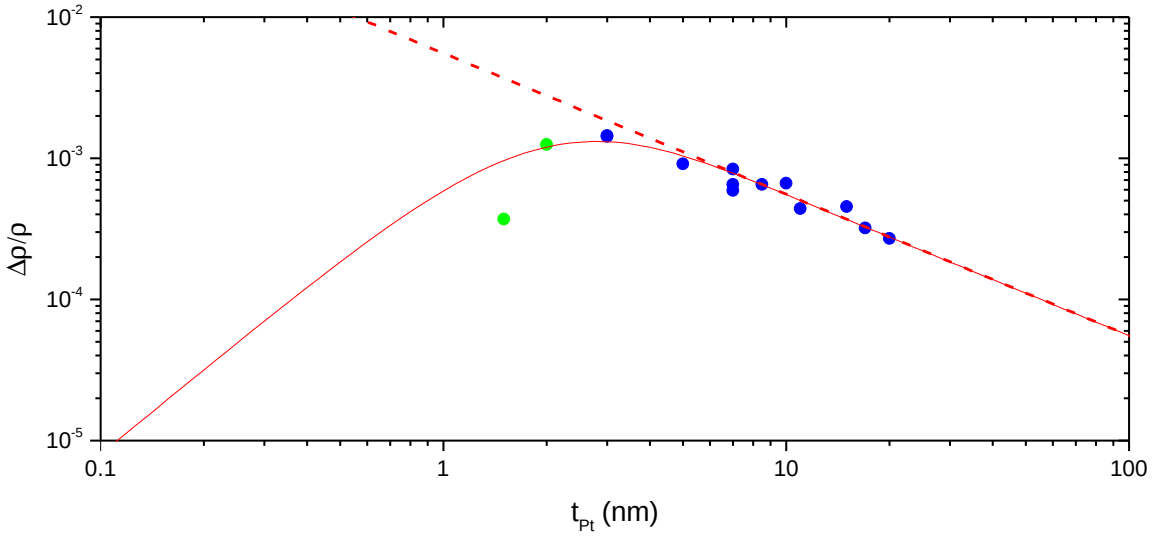

Figure 6.6: SMR data plotted over the samples' platinum layer thickness t_{Pt}. The solid line is a fit to the experimental data according to Eq. (6.7). The dashed line indicates the $1/t_{\mathrm{Pt}}$ limit of Eq. (6.7). At above $t_{\mathrm{Pt}} \gtrapprox 2\,\mathrm{nm}$ the difference between the fit and the simple power law is sufficiently small to justify the approximation. The green dots mark the samples where this approximation fails. The data have been provided by Matthias Althammer.

For the above parameter values, this limit is justified beyond a platinum layer thickness of around $t_{\mathrm{Pt}} = 2.2\,\mathrm{nm}$, where the deviation from the full theory is less than a factor of two. Hence, the analysis will now be restricted to samples with $t_{\mathrm{Pt}} \geq 3\,\mathrm{nm}$. This a posteriori justifies the assumption made in the previous section that samples with a platinum layer thickness of less than 3 nm do follow a different trend and should therefore be omitted from the analysis.

In Sec. 6.1 it was found that (*cf.* Fig. 6.3)

$$\frac{V_{\mathrm{ISH}}}{\Delta T \rho} \propto \frac{1}{t_{\mathrm{Pt}}^{3/2}}. \tag{6.9}$$

The ratio

$$\frac{\frac{\Delta\rho}{\rho}}{\frac{V_{\mathrm{ISH}}}{\Delta T \rho}} = \frac{\Delta T \Delta \rho}{V_{\mathrm{ISH}}} \tag{6.10}$$

$$= \frac{\theta_{\mathrm{H}}^2 \frac{2\lambda_{\mathrm{Pt}}^2 \rho_{\mathrm{Pt}}}{t_{\mathrm{Pt}}} \frac{e^2}{h} \mathrm{Re}(g^{\uparrow\downarrow})}{1 + 2\lambda_{\mathrm{Pt}} \rho_{\mathrm{Pt}} \frac{e^2}{h} \mathrm{Re}(g^{\uparrow\downarrow})} \Big/ \frac{\theta_{\mathrm{H}} e \gamma \mathrm{Re}(g^{\uparrow\downarrow}) k_{\mathrm{B}}}{\pi M_{\mathrm{s}} V_{\mathrm{mc}}} \frac{1}{w} \frac{a^2 \pi}{2} \frac{\bar{\lambda}}{t_{\mathrm{Pt}}^{3/2}} \tag{6.11}$$

$$= \frac{\theta_{\mathrm{H}} \lambda_{\mathrm{Pt}}^2 \rho_{\mathrm{Pt}} e M_{\mathrm{s}} V_{\mathrm{mc}} w}{\left(1 + 2\lambda_{\mathrm{Pt}} \rho_{\mathrm{Pt}} \frac{e^2}{h} \mathrm{Re}(g^{\uparrow\downarrow})\right) h \gamma k_{\mathrm{B}} a^2 \bar{\lambda}} t_{\mathrm{Pt}}^{1/2} \tag{6.12}$$

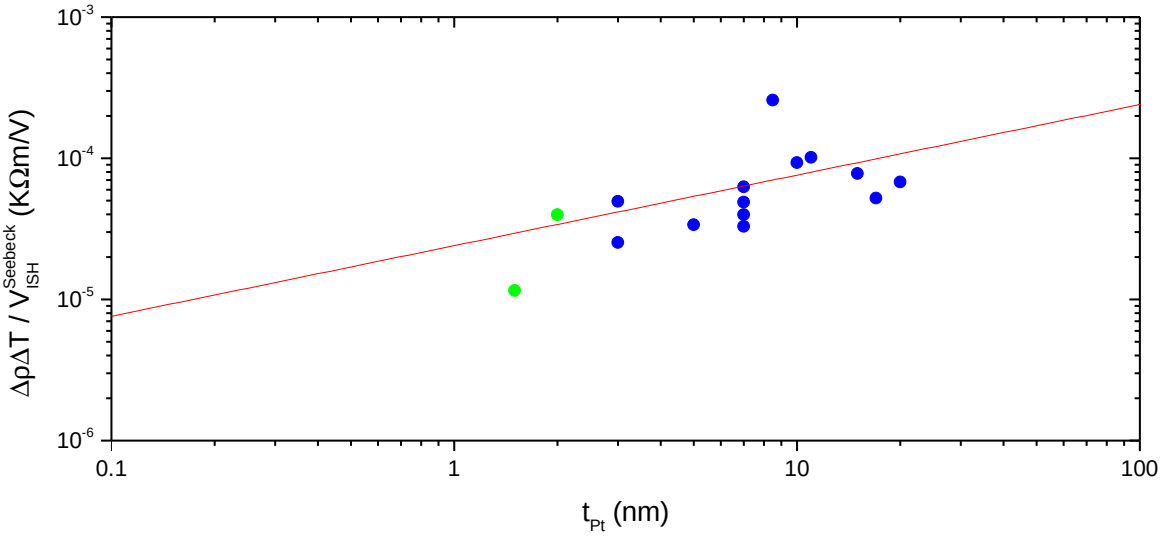

Figure 6.7: Test of the validity of Eq. (6.12): The ratio of the SMR amplitude $\Delta\rho/\rho$ to the spin Seebeck voltage V_{ISH} plotted as a function of t_{Pt}. The green dots once again mark samples with $t_{\mathrm{Pt}} < 3\,\mathrm{nm}$ which are not taken into account for the $t_{\mathrm{Pt}}^{1/2}$ fit (red line)

suggests that the ratio of SMR amplitude and spin Seebeck voltage should scale with $t_{\mathrm{Pt}}^{1/2}$. Indeed, the data available corroborates this prediction (Fig. 6.7). Fitting a t_{Pt}^{α} dependency to the corresponding data yields $\alpha = 0.38 \pm 0.19$ ($\alpha = 0.76 \pm 0.17$ if sample #12 which shows the highest SMR amplitude but only average spin Seebeck voltage was not taken into account[3]) so that the assumed $t_{\mathrm{Pt}}^{1/2}$ behaviour is well represented by the data.

Another approach is to directly compare the SMR amplitude and the spin Seebeck voltage for each sample. In Fig. 6.8 it can be seen that

$$\frac{\Delta\rho}{\rho} \propto \left(\frac{V_{\mathrm{ISH}}}{\Delta T \rho}\right)^{\beta}, \tag{6.13}$$

holds, with $\beta = 0.49 \pm 0.09$. However, if one assumes $\beta = 2/3$ the error of the fit only increases marginally. Under this assumption and since $\frac{V_{\mathrm{ISH}}}{\Delta T \rho} \propto t_{\mathrm{Pt}}^{-3/2}$ it follows that

$$\left(\frac{V_{\mathrm{ISH}}}{\Delta T \rho}\right)^{2/3} \propto t_{\mathrm{Pt}}^{-(3/2)\cdot(2/3)} = t_{\mathrm{Pt}}^{-1} \propto \frac{\Delta\rho}{\rho}.$$

[3] When this sample was examined in the spin Seebeck setup, the copper block that the sample is glued to was notably skewed so that the applied magnetic field was most likely not very well aligned to the thin film plane. Thus the measured spin Seebeck voltage is potentially lower than the actual maximal signal of the sample.

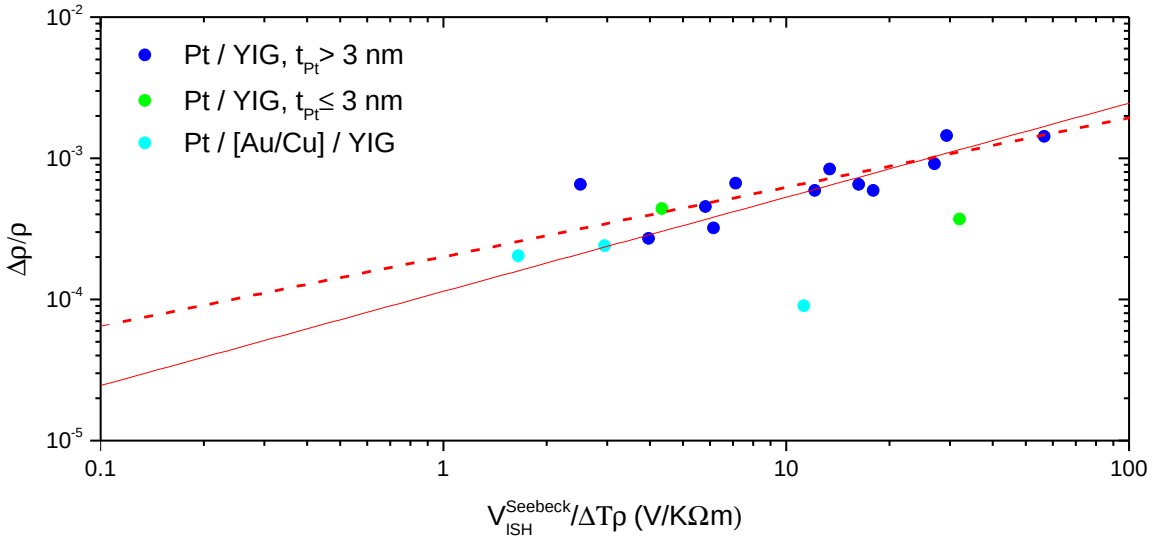

Figure 6.8: Plot of the SMR amplitude $\Delta\rho/\rho$ over the respective spin Seebeck voltage $V_{\mathrm{ISH}}/\Delta T\rho$ for the different samples. While the 2/3 fit (Eq. (6.13), solid red line) has been done for the blue points with $t_{\mathrm{Pt}} > 3\,\mathrm{nm}$ only, it does agree reasonably well even for samples with thin platinum layers and those with an additional buffer layer between the platinum and the YIG. The dashed red line is a fit with free exponent to the blue data points.

This corroborates the notion that the spin Seebeck effect and the spin Hall magneto resistance are indeed dependent on t_{Pt} as given by Eq. (6.9) and (6.8).

Taking the samples with very thin platinum layers and the ones with an additional buffer layer into account, the fit (Eq. (6.13)) yields $\beta = 0.58 \pm 0.16$, which agrees well with the above value of 2/3.

While this is a consistent and therefore convincing result, it is important to note that a similar agreement with the experimental data can be achieved if one assumes $\Delta\rho/\rho \propto (V_{\mathrm{ISH}}/\Delta T\rho)^{1/2}$ and therefore $V_{\mathrm{ISH}}/\Delta T\rho \propto t_{\mathrm{Pt}}^{-2}$.

Eq. (6.13) shows that either the spin Seebeck effect or the spin Hall magneto resistance can be used to quantitatively predict the strength of the other even if the exact relation between the two can only be approximated as of now. Further experiments are therefore necessary to quantitatively resolve this issue.

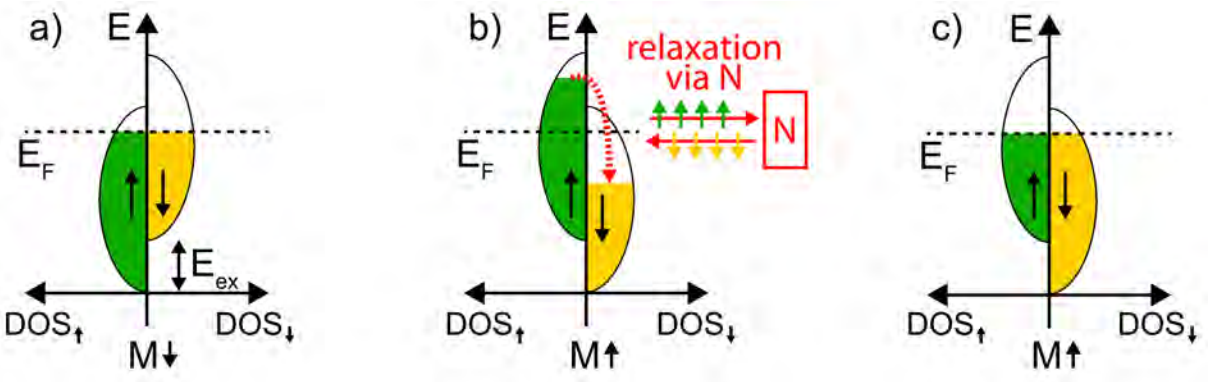

Figure 6.9: Figure taken from [18]. The distribution of conduction electrons among the two different spin species with their respective density of states (DOS) in a ferromagnet. **a)** In equilibrium the DOS for up and down electrons is shifted due to the exchange energy E_{ex}. **b)** In a gedankenexperiment the energy levels for the two spin species change almost instantaneously (in realty this is caused by to the rf magnetic field), bringing the system out of equilibrium that is restored via a spin relaxation process. **c)** After some time the system is in equilibrium again.

6.3 Comparison of spin pumping and spin Seebeck effect

Another approach for creating pure spin currents has been theoretically proposed by Tserkovnyak *et al.* [105] in 2002, following a paper by Berger [106] in 1996. In this so-called spin pumping scheme, a radio frequency magnetic field is applied to a ferromagnet which causes the magnetization vector to precess. The relaxation of the latter then creates a spin current that can be converted into a charge current by means of the inverse spin Hall effect (*cf.* Ch. 2). Usually this type of experiment is done in F/N hybrid structures such as the ones examined in this thesis.

With an ansatz [105] that is only marginally different than the one chosen for the derivation of the spin Seebeck effect (Ch. 2) one finds an instantaneous spin current

$$\boldsymbol{I}_{\mathrm{s}} = \frac{\hbar}{4\pi}\mathrm{Re}(g^{\uparrow\downarrow})\,[\boldsymbol{m}\times\dot{\boldsymbol{m}}] \tag{6.14}$$

which time-averages to the DC spin current

$$I_{\mathrm{s}} = P\cdot\frac{1}{2\pi}\frac{\hbar}{2}\omega\mathrm{Re}(g^{\uparrow\downarrow})\sin^2\Theta \tag{6.15}$$

in the approximation of a circular precession cone. Here ω denotes the microwave frequency[4], Θ is the precession cone angle of the magnetization caused by the microwave magnetic field and P is a correction factor that accounts for the influence of demagnetization fields on the magnetization precession [107]. Taking into account the accumulation of spins within the thin normal metal film in which the spin current is converted into a charge current this leads to [105, 18]

$$V_{\mathrm{sp}} = \frac{e\theta_{\mathrm{H}}\lambda_{\mathrm{N}} \tanh\left(\frac{t_{\mathrm{N}}}{2\lambda_{\mathrm{N}}}\right) \mathrm{Re}(g^{\uparrow\downarrow})}{\sigma_{\mathrm{F}} t_{\mathrm{F}} + \sigma_{\mathrm{N}} t_{\mathrm{N}}} \nu_{\mathrm{MW}} P l \sin^2\Theta. \tag{6.16}$$

Here λ_{N} is the spin diffusion length within the normal metal and σ_{F}, σ_{N}, t_{F} and t_{N} are the electrical conductivities and thicknesses of the ferromagnet and normal metal, respectively and l denotes the sample length. In the thick platinum layer regime ($t_{\mathrm{Pt}} > \lambda_{\mathrm{Pt}}$) and with YIG as ferromagnet ($\sigma_{\mathrm{F}} = 0$) Eq. (6.16) transforms into

$$\lim_{t_{\mathrm{Pt}}\to\infty} V_{\mathrm{sp}} = \lim_{t_{\mathrm{Pt}}\to\infty} \frac{e\theta_{\mathrm{H}}\lambda_{\mathrm{Pt}}\mathrm{Re}(g^{\uparrow\downarrow})}{\sigma_{\mathrm{Pt}} t_{\mathrm{Pt}}} \nu_{\mathrm{MW}} P l \sin^2\Theta. \tag{6.17}$$

In order to compare the spin Seebeck signal $V_{\mathrm{ISH}}^{\mathrm{Seebeck}}$ with the spin pumping magnitude across different samples, one has to divide Eq. (6.17) by factors that are not directly related to the effect itself or show a known inherent thickness dependence. Under the assumptions that $\tanh\left(\frac{t_{\mathrm{N}}}{2\lambda_{\mathrm{N}}}\right) \approx 1$, Eq. (6.17) then transforms into

$$\frac{V_{\mathrm{sp}}}{\nu_{\mathrm{MW}} P l \rho_{\mathrm{Pt}} \sin^2\Theta} = \frac{e\theta_{\mathrm{H}}\lambda_{\mathrm{Pt}}\mathrm{Re}(g^{\uparrow\downarrow})}{t_{\mathrm{Pt}}} \propto \frac{1}{t_{\mathrm{Pt}}}. \tag{6.18}$$

In Fig. 6.10 data for samples #2, #3, #6, #10, #11, #12, #17, #19 and #20 ($t_{\mathrm{Pt}} > 3\,\mathrm{nm}$) are shown along with a t_{Pt}^{-1} fit of the data. The spin pumping data for these samples have been provided by Johannes Lotze. While the agreement between the theoretical prediction and the experimental data is reasonable a fit with a free exponent α returns $\alpha = -1.54 \pm 0.32$, which suggests that other parameters also are dependent on the platinum layer thickness.

Note that the spin pumping samples are not *exactly* the same as in the SMR and spin Seebeck experiments: after a YIG/Pt sample was grown via pulsed laser deposition (see Ch. 3) it was cut into several pieces, one of which was used for the spin pumping measurements, while another was used for the spin Seebeck and spin Hall magneto resistance measurements. Therefore the quality of the YIG and platinum should be the same in the spin pumping, spin Seebeck and spin Hall magneto resistance experiments, but anything that could have altered the samples during the patterning and etching process will not be

[4] the rf magnetic field frequency

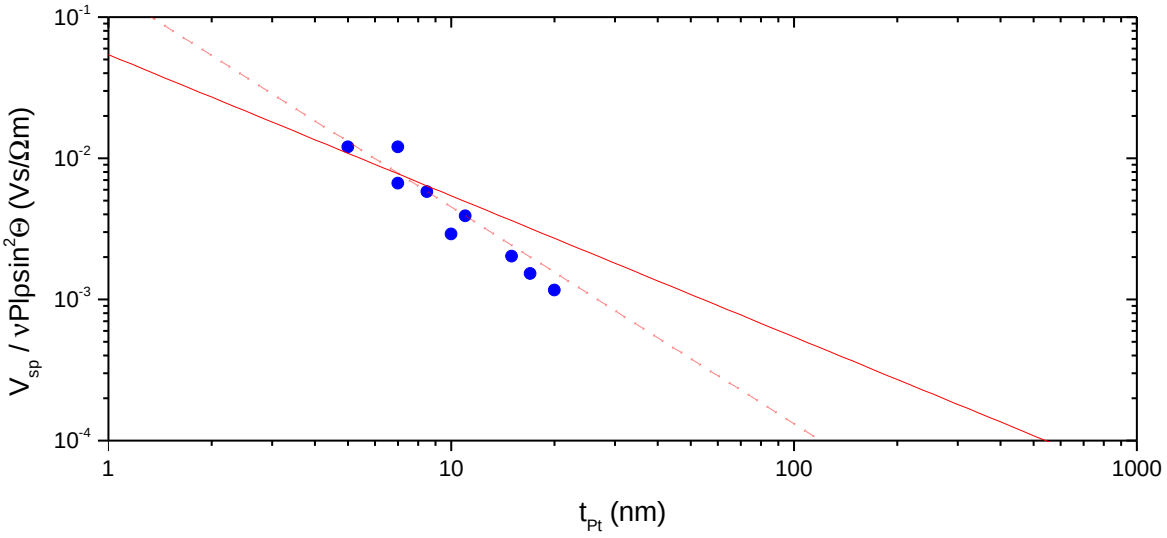

Figure 6.10: To allow for a comparison of the spin pumping voltage V_{sp} in samples with different platinum layer thickness, V_{sp} is divided by all factors that are known to vary across the different samples and measurements. The solid red line indicates a t_{Pt}^{-1} fit according to Eq. (6.18), to the data while the dashed line is a fit with free exponent. The data have been provided by Johannes Lotze.

seen in this data.

Just as in Sec. 6.2, a comparison of spin pumping and spin Seebeck data, appears mandatory. Since

$$\frac{V_{\mathrm{ISH}}}{\Delta T \rho} \propto t_{\mathrm{Pt}}^{-3/2}$$

for the spin Seebeck effect (Eq. (6.9)), one should observe

$$\frac{\frac{V_{\mathrm{sp}}}{\nu_{\mathrm{MW}} P l \rho_{\mathrm{Pt}} \sin^2\Theta}}{\frac{V_{\mathrm{ISH}}}{\Delta T \rho_{\mathrm{Pt}}}} = \frac{V_{\mathrm{sp}} \Delta T'}{V_{\mathrm{ISH}} \nu_{\mathrm{MW}} P l \sin^2\Theta} \tag{6.19}$$

$$= \frac{\frac{e\theta_{\mathrm{H}}\lambda_{\mathrm{Pt}}\mathrm{Re}(g^{\uparrow\downarrow})}{t_{\mathrm{Pt}}}}{\frac{\theta_{\mathrm{H}} e\gamma \mathrm{Re}(g^{\uparrow\downarrow}) k_{\mathrm{B}}}{\pi M_{\mathrm{s}} V_{\mathrm{mc}}} \frac{1}{w} \frac{a^2\pi}{2} \frac{\bar{\lambda}}{t_{\mathrm{Pt}}^{3/2}}} \tag{6.20}$$

$$= \frac{\lambda_{\mathrm{Pt}} \gamma k_{\mathrm{B}} a^2 \pi \bar{\lambda}}{2 M_{\mathrm{s}} V_{\mathrm{mc}} w} t_{\mathrm{Pt}}^{1/2}. \tag{6.21}$$

Figure. 6.11 shows the data, plotted according to Eq. (6.21). However the data do not support the predicted $t_{\mathrm{Pt}}^{1/2}$ trend in a satisfactorily fashion. The result in fact allows for no clear determination of a scaling behaviour with the platinum layer thickness between spin pumping and spin Seebeck effect.

Again, an alternative approach to compare spin pumping and spin Seebeck effect is to

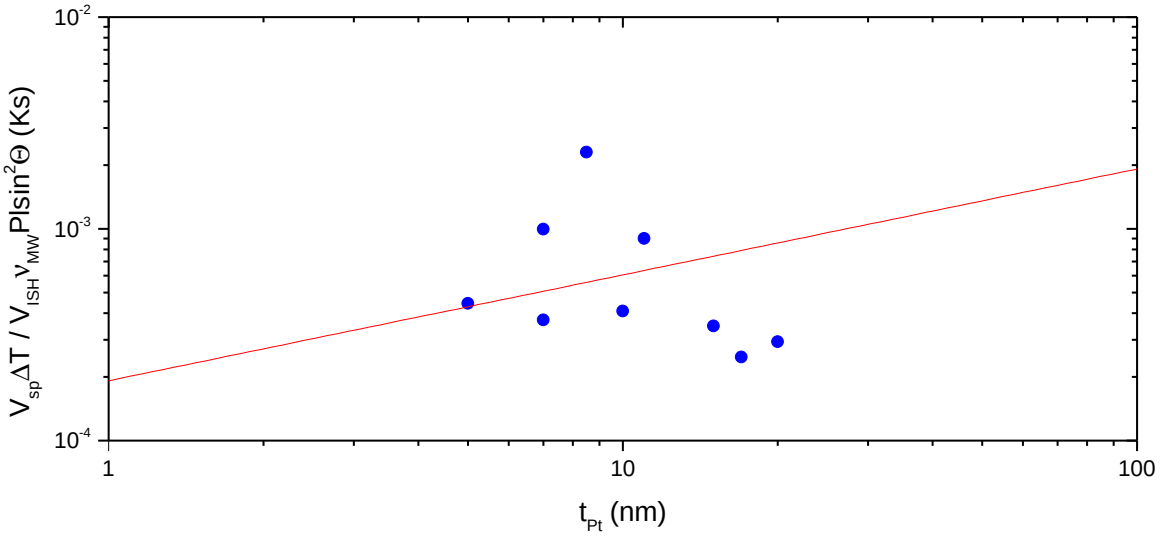

Figure 6.11: Plot of the ratio of the spin pumping signal V_{sp} over the spin Seebeck signal V_{ISH} for each sample as a function of the sample thickness t_{Pt}. The red line is a fit of the suspected $t_{\mathrm{Pt}}^{1/2}$ behaviour. No clear conclusion about the relation between the spin pumping signal V_{sp} and the spin Seebeck signal V_{ISH} can be made from the data available.

look at how the spin pumping signal scales with the spin Seebeck signal directly. Since

$$V_{\mathrm{sp}} \propto t_{\mathrm{Pt}}^{-1},\ V_{\mathrm{ISH}} \propto t_{\mathrm{Pt}}^{-3/2} \Rightarrow V_{\mathrm{sp}} \propto (V_{\mathrm{ISH}})^{2/3} \tag{6.22}$$

if the assumptions made before are correct. In Fig. 6.12 it can be seen that the data follow the predicted trend reasonably well and a fit with free exponent α yields $\alpha = 0.74 \pm 0.26$ in good agreement with the heuristic model. This again supports the notion that spin currents can be described by a unified model.

Overall the comparison between spin Seebeck effect and spin pumping yields a qualitative agreement while and the comparison with the spin Hall magneto resistance appears more robust. However if one assumes that $V_{\mathrm{sp}} \propto t_{\mathrm{Pt}}^{-3/2}$ (instead of t_{Pt}^{-1}) then $V_{\mathrm{sp}}/V_{\mathrm{ISH}} = \text{const.}$ which agrees with the result that is obtained from a fit of the data (Fig.6.10) with free exponent ($\alpha = -0.43 \pm 0.76$). This would result in $V_{\mathrm{sp}} \propto (V_{\mathrm{ISH}})^1$ which is well within the margin of error of the fit. The same can be argued for $V_{\mathrm{sp}} \propto t_{\mathrm{Pt}}^{-2}$. Assuming both the spin pumping and spin Seebeck theory are correct, then this could hint at additional parameters not being independent of the film thickness. Since $g^{\uparrow\downarrow}$ is an interface effect this leaves λ_{Pt} as a possible culprit.

In summary, in this chapter it was found that the spin Seebeck theory developed by Xiao *et al.*[9] has to be modified to take the platinum layer thickness into account. A simple

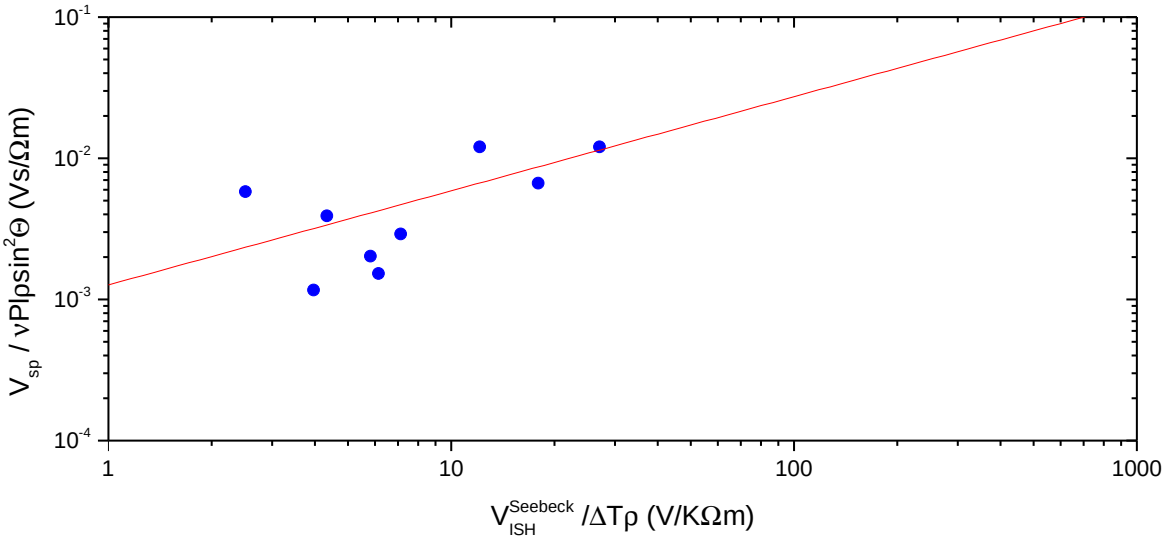

Figure 6.12: Plot of the spin pumping voltage over the spin Seebeck voltage obtained for the different samples studied. The red line is a $t_{\mathrm{Pt}}^{2/3}$ fit of the data according to Eq. (6.22).

power law appears sufficient to describe the experimental data. On this basis a comparison between the spin Seebeck effect, the spin Hall magneto resistance and spin pumping was done. The experimental data show a strong correlation between the three effects which could be accounted for by comparing the individual theories with each other. However, to quantitatively connect these different spin current related effects further theory work and experiments will be necessary.

7 Summary and Outlook

This thesis gives a detailed, quantitative experimental study of the spin Seebeck effect. It thus continues and substantially extends the work done at the Walther-Meißner-Institute by Mathias Weiler during his PhD thesis [49].
The spin Seebeck effect hinges on the interplay between thermally excited phonons and magnons in a ferromagnet and how a thermal non-equilibrium leads to the creation of pure spin currents. Mathias Weiler showed that not only is it possible to observe the spin Seebeck effect in yttrium iron garnet thin films, but that the effect can be locally detected. The spin Seebeck effect thus enables the generation of local spin currents, and can furthermore be utilized to map the domain structure in the ferromagnetic layer [35].

This thesis goes beyond the results of Weiler *et al.* [49, 35] in several aspects. For one, we showed that it is possible to locally manipulate the yttrium iron garnet's magnetization and how edge states and other geometric effects influence the creation of magnetic domains (Sec. 4.4).Furthermore a new class of ferromagnetic insulator/normal metal samples with an additional layer between the ferromagnet and the normal metal was examined (Sec. 4.5). These experiments prove that spin currents can not only be detected far away from the ferromagnetic insulator/normal metal interface at which they are created, but also that anomalous Nernst contributions to the measured voltage signal can be excluded. The scaling of the spin Seebeck effect with the induced temperature increase was examined and experimentally confirmed to be linear (Sec. 4.6) as predicted by the theory. Additionally, first experiments have been done to address the time constants involved in the generation of the spin Seebeck signal. In good agreement with the known time constants for the phonon-magnon and phonon-electron coupling we could confirm that the spin Seebeck signal arises on timescales shorter than one microsecond (Sec. 4.7).
One key outcome of the present thesis is the substantially improved simulation of the temperature distribution in the ferromagnetic insulator/normal metal hybrids, most prominently taking into account thermal contact resistances between the individual layers. The corresponding results enabled a quantitative analysis of the spin Seebeck signal (Ch. 5).

This new simulation now not only makes it possible to directly compute (and possibly predict) the spin Seebeck effect magnitude from theory, but is furthermore versatile enough to account for any combination of layers in the thin film samples, which was not possible in previous models [76, 108]. Additionally, we found that the spin Seebeck signal is inversely proportional to the platinum layer thickness (Sec. 6.1) a fact that is not evident from the published theory but could be motivated by comparison with spin pumping experiments. Last but not least, the spin Seebeck effect data obtained in this thesis were quantitatively compared to spin pumping measurements and the newly discovered spin Hall magneto resistance. The latter two effects are also influenced by a spin current/interface interaction. We found a direct, quantitative relation between spin Seebeck effect, spin Hall magneto resistance and spin pumping that could be accounted for both in a modelling approach and the experimental data (Sec. 6.2 and 6.3).
These results unambiguously show that the voltage signals observed in this thesis are indeed due to the *longitudinal* spin Seebeck. This is a very encouraging result since the original *transversal* spin Seebeck effect [8] has been questioned a lot lately since the corresponding results from Uchida *et al.* appear difficult to replicate. Furthermore, our experiments show that the spin Seebeck theory needs to be adjusted for additional dependencies. Eventually a new theory accounting for all spin transport type phenomena clearly will be required.
The contributions from this thesis help in the fundamental understanding of not only the spin Seebeck effect, but also the spin Hall magneto resistance and the spin pumping effect. Nevertheless there are still many issues that need to be tackled before a truly complete picture of spin current related physics can be drawn. We strongly believe that further investigations and investments into this filed will be greatly rewarding.

Outlook

Spintronics could be a future key factor in the never ending pursuit of faster computation. Spincaloritronics is the a new spin to this field, and the understanding of the processes involved is still in its early days.
For application purposes, the behaviour of the spin Seebeck effect on short timescales will be of critical importance. Corresponding spin Seebeck experiments on timescales in the sub microsecond regime are currently under way at the Walther-Meißner-Institute. The scaling of the effect on short timescales could very well also give important fundamental insights and determine the feasibility of possible computing applications.

A seemingly endless field is the search for material systems with larger Spin Seebeck magnitude. Right now, the measured spin Seebeck voltages are of the order of a couple of microvolts, which is not straightforward to detect and prone to noise. One important step here also is to study the impact of the ferromagnetic insulator ayer thickness on the spin Seebeck effect. Yttrium iron garnet samples are already in production to verify the spin Seebeck effect in the bulk regime. Additionally, engineering of samples with high thermal contact resistance could be a way of increasing signal strength. Le Breton *et al.* [109] showed that the spin *dependent* Seebeck effect[1] can even be observed when the spin current has to cross a tunneling barrier. By careful engineering one could possibly design a device with large spin mixing conductance but much higher temperature difference between the ferromagnet and the normal metal, and thus increase the spin current between the two. That way one could also utilize different ferromagnets, especially conducting ones, if the tunneling barrier could be designed in a way that the tunneling resistance is different for electrons and magnons. Since a tunneling process can not occur unless there are free states at the opposite side of the barrier it also has to be thin enough to allow the exchange interaction to influence the electrons in the normal metal in order to observe the spin Seebeck effect.

There have also been reports about new materials exhibiting very large spin Hall angles [111]. Replacing the platinum layer on top of the yttrium iron garnet, e.g. by β-tantalum, should increase the spin Seebeck signal and make observations at lower heating power possible. The existing setup could also be used to find such materials, or, once a full picture of the quantities involved emerges, to measure those quantities that are still only known within some orders of magnitude (e.g., $g^{\uparrow\downarrow},\ \theta_{\mathrm{H}},\ \lambda_{\mathrm{sd}}$).

Since the different"spin current at interfaces" experiments (namely spin pumping, spin Hall magneto resistance and spin Seebeck effect) seem to be correlated to each other it would also be interesting to develop a device enabling all the different measurements in one setup.

Up to now, our improved simulation still uses a simplified geometry to calculate the temperature profile in the samples. This is not a limit of the simulation itself, but was done to speed up the simulation work since, after all necessary parameters are collected and/or calculated, creating the geometry is the most time consuming task. Therefore, an extended version of the existing simulation could be used to not only reevaluate to data collected so far but also to develop new sample designs in which the temperature profile becomes more beneficial to the spin Seebeck effect.

Just like the classical Seebeck has its inverse in the Peltier effect, there is also the spin Peltier effect. While the spin *dependent* Peltier effect [112] has already been observed,

[1] In the spin dependent Seebeck effect, the Seebeck coefficient is different for spin up and spin down electrons, which gives rise to spin polarized currents [110].

the spin Peltier effect still awaits experimental observation. In general this could be done with the current samples in the spin pumping setup, if one would be able to distinguish between the signal from spin pumping and the additional contribution from the heating or cooling of the platinum induced by the spin Peltier effect and the subsequent change in resistance.
Just as the classical Seebeck and Peltier effect can be derived form the same theory, the correlations between spin Seebeck effect, spin Hall magneto resistance and spin pumping revealed in this work ask for a new theory developed by which all spin current related effects can be described. Maybe in the future there will be "Maxwell's spin equations" that achieve this goal.

We are confident that the results presented here contribute to both the theoretical and experimental understanding of the spin Seebeck effect. Yet they also showed that many more experiments and theoretical work will be necessary to create a full understanding of the spin Seebeck effect. We hope that our results can inspire others to investigate the open issues and contribute to this fascinating field of physics.

A Appendix

A.1 Simulation parameters

	abosrption coefficient α [m^{-1}]	heat capacity C [J/kgK]	density ρ [kg/m^3]	thermal conductivity κ [W/m K]	refractive index n
Pt	$82 \cdot 10^6$ [55]	130 [113]	21450 [114]	72 [114]	$2.41 + 4.3i$ [55]
YIG	$0.5 \cdot 10^5$ [115]	570 [113]	5170 [116]	7.4 [117]	$2.2 + 0.003i$ [115]
GGG	0 [118]	400 [119]	7080 [119]	8 [120]	-
YAG	0 [121]	625 [119]	4560 [122]	13 [123]	-
Au	$62.5 \cdot 10^6$ [55]	130 [113]	19300 [124]	318 [125]	$0.16 + 3.28i$ [55]
Cu	$72 \cdot 10^6$ [55]	385 [113]	8960 [54]	419 [126]	$2.14 + 3.75i$ [55]

	longitudinal speed of sound v_{long} [m/s]	transversal speed of sound v_{trans} [m/s]	Sommerfeld constant γ [J/m^3K^2]	Fermi velocity v_F [m/s]
YIG	7180 [127]	3300 [128]	-	-
Pt	3300 [129]	1700 [129]	748.1 [130]	$2.188 \cdot 10^5$ [131]
GGG	6545 [132]	3531 [132]	-	-
YAG	8600 [133]	4960 [133]	-	-
Au	3240 [54]	1200 [54]	67.6 [130]	$1.041 \cdot 10^6$ [134]
Cu	4760 [54]	2325 [54]	96.8 [130]	$1.245 \cdot 10^6$ [134]

Table A.1: Material parameters used for the ANSYS simulation of the heat distribution

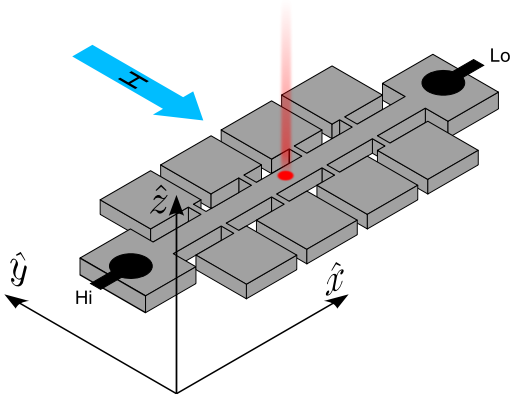

Figure A.1: The sign measurement was done with a digital multimeter with the contacts connected and external magnetic field oriented as depicted above.

A.2 Sign in the spin Seebeck measurements

Since the spin Seebeck measurements presented in Ch. 4.4 were done using the lock-in technique it is not possible to determine the actual sign of the measured voltage as a phase has to be chosen arbitrarily. However a spin Seebeck measurement was also done where a Keithley K2002 [135] multimeter was used to measure the spin Seebeck signal. In order to get an absolutely reliable sign the external magnetic field direction was determined using a compass. Positive magnetic field direction is defined as the direction from the Antarctic to the Arctic. With the setup depicted in Fig. A.1 a **positive** voltage was measured.
The spin polarization $\hat{\boldsymbol{s}}$, orients itself antiparallel to the external magnetic field $\boldsymbol{H} = -\hat{\boldsymbol{y}}H$. Since YIG has a fairly low absorption coefficient compared to platinum it follows that $T_\mathrm{F} < T_\mathrm{N} \Rightarrow \Delta T < 0$ and hence the spin current (Eq. 2.31) is flowing in $-\hat{\boldsymbol{z}}$ direction. Now the *physical* (positive) charge current direction can be calculated as

$$\begin{aligned}
\boldsymbol{I}_\mathrm{c}^\mathrm{ISH} &= \theta_\mathrm{H}\left(-\frac{2e}{\hbar}\right) I_\mathrm{s} \begin{pmatrix} 0 \\ 0 \\ -1 \end{pmatrix} \times \begin{pmatrix} 0 \\ 1 \\ 0 \end{pmatrix} \\
&= -\theta_\mathrm{H}\frac{2e}{\hbar} I_\mathrm{s} \begin{pmatrix} 1 \\ 0 \\ 0 \end{pmatrix} \\
&= -\hat{\boldsymbol{x}}\theta_\mathrm{H}\frac{2e}{\hbar} I_\mathrm{s}.
\end{aligned} \tag{A.1}$$

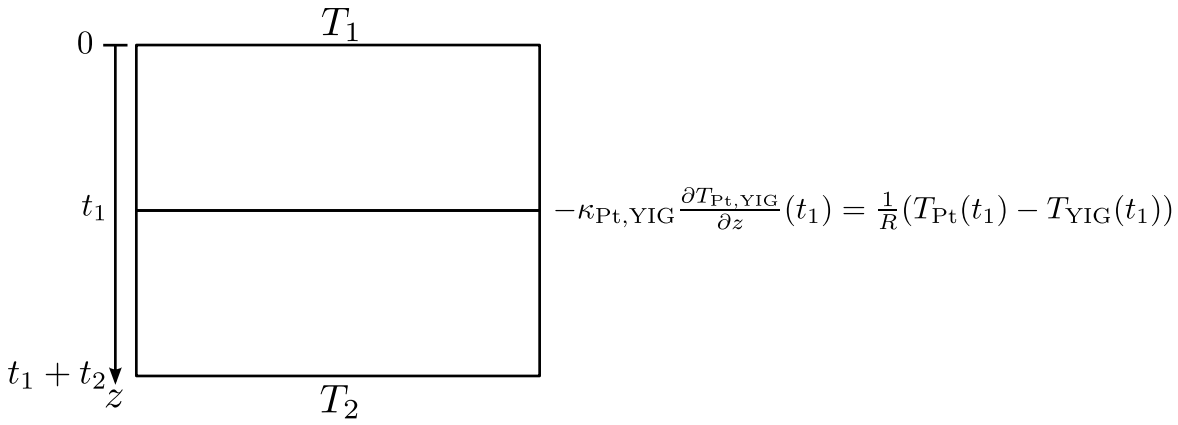

Figure A.2: Depiction of the simplified heat transport problem as used e.g. in [32]

Therefore the *conventional* current direction is in $+\hat{\boldsymbol{x}}$ direction, from **Hi** to **Lo**, and returns a positive voltage.
This is consistent with the sign observed by Uchida *et al.* [32] and Weiler *et al.* [35].

A.3 Derivation of the temperature distribution in a two layer system

In the spin Seebeck experiments by Uchida *et al.* [32] a thin platinum layer was deposited on bulk yttrium iron garnet. The temperature of the top and bottom of the sample were held at constant temperatures T_1 and T_2. With the geometry depicted in Fig. A.2 the solution of Eq. (5.5) in steady state is of the form

$$\Delta T_i = 0 \tag{A.2}$$

Using the Dirichlet boundary conditions mentioned above and the finite thermal contact resistance R at the interface between the platinum and the yttrium iron garnet this is solved by

$$\begin{aligned}
T_i(z) &= a_i + b_i z, \\
T_{\mathrm{Pt}}(0) &= T_1 \Rightarrow a_{\mathrm{Pt}} = T_1, \\
T_{\mathrm{YIG}}(t_1 + t_2) &= T_2 \Rightarrow T_2 = a_{\mathrm{YIG}} + b_{\mathrm{YIG}}(t_1 + t_2), \\
\left.\frac{\partial T_{\mathrm{Pt}}}{\partial z}\right|_{t_1} &= b_{\mathrm{Pt}} = \frac{-1}{\kappa_{\mathrm{Pt}} R}\left[T_{\mathrm{Pt}}(t_1) - T_{\mathrm{YIG}}(t_1)\right] = \frac{-1}{\kappa_{\mathrm{Pt}} R}\left[T_1 + b_{\mathrm{Pt}} t_1 - a_{\mathrm{YIG}} - b_{\mathrm{YIG}} t_1\right], \\
\left.\frac{\partial T_{\mathrm{YIG}}}{\partial z}\right|_{t_1} &= b_{\mathrm{YIG}} = \frac{-1}{\kappa_{\mathrm{Pt}} R}\left[T_{\mathrm{Pt}}(t_1) - T_{\mathrm{YIG}}(t_1)\right] = \frac{-1}{\kappa_{\mathrm{YIG}} R}\left[T_1 + b_{\mathrm{Pt}} t_1 - a_{\mathrm{YIG}} - b_{\mathrm{YIG}} t_1\right],
\end{aligned}$$

which yields the coefficients

$$\begin{aligned}
a_{\mathrm{Pt}} &= T_1, \\
b_{\mathrm{Pt}} &= \frac{\kappa_{\mathrm{YIG}} T_2 - \kappa_{\mathrm{Pt}} T_1}{\kappa_{\mathrm{Pt}}\kappa_{\mathrm{YIG}} R + \kappa_{\mathrm{YIG}} t_1 + \kappa_{\mathrm{Pt}} t_2}, \\
a_{\mathrm{YIG}} &= \frac{\kappa_{\mathrm{Pt}} t_1 T_1 + \kappa_{\mathrm{Pt}} t_2 T_1 + \kappa_{\mathrm{Pt}}\kappa_{\mathrm{YIG}} R T_2 - \kappa_{\mathrm{Pt}} t_1 T_2 + \kappa_{\mathrm{YIG}} t_1 T_2}{\kappa_{\mathrm{Pt}}\kappa_{\mathrm{YIG}} R + \kappa_{\mathrm{YIG}} t_1 + \kappa_{\mathrm{Pt}} t_2}, \\
b_{\mathrm{YIG}} &= \frac{\kappa_{\mathrm{Pt}}(T_1 - T_2)}{\kappa_{\mathrm{Pt}}\kappa_{\mathrm{YIG}} R + \kappa_{\mathrm{YIG}} t_1 + \kappa_{\mathrm{Pt}} t_2}.
\end{aligned} \tag{A.3}$$

Due to the reduced dimensionality of this solution compared to the heat transfer problem discussed in this thesis (see Ch. 5) the different results can not be compared directly, since the heat flow in the lateral direction drastically influences the final result. For very thin layers, however, these differences become less significant. Using $t_{\mathrm{Pt}} = 7\,\mathrm{nm}$ and $t_{\mathrm{YIG}} = 20\,\mathrm{nm}$ (sample #3), the thermal conductivities tabulated in Tab. A.1 and the thermal contact resistance from Tab. 5.2 with the temperatures for the platinum and the yttrium iron garnet from the simulation results shown in Fig. 5.5 the temperature difference at the F/N interface calculated analytically as obtained above and by the ANSYS simulation agree with each other within 2%. Note that this does not mean that the temperature profiles in our samples can be calculated analytically by the above since once the (thick) substrate ($t_{\mathrm{GGG}} = 500\,\mu\mathrm{m}$) has to be taken into account the heat flow in the lateral direction drastically changes the shape of the temperature profile.

Bibliography

[1] G. E. Moore. "Cramming More Components onto Integrated Circuits". In: *Electronics* 38.8 (Apr. 1965), pp. 114–117. ISSN: 0018-9219. DOI: 10.1109/JPROC.1998.658762. URL: http://dx.doi.org/10.1109/JPROC.1998.658762.

[2] Benjamin Franklin. "Experiments and Observations on Electricity, Made at Philadelphia in America, by Mr. Benjamin Franklin". In: *The Gentlemans Magazine* (1750).

[3] Luigi Galvani. *Aloysii Galvani in Bononiensi Archigymnasio, & Instituto Scientiarum publici professsoris... De viribus electricitatis in motu musculari commentarius: cum Joannis Aldini dissertatione et notis: accesserunt epistolae ad animalis electricitatis theoriam pertinentes*. Mutinae: Apud Societatem Typographicam, 1792.

[4] André-Marie Ampère. *Exposé des nouvelles découvertes sur l'électricité et le magneétisme*. Chez Méquignon-Marvis, 1822.

[5] P. M. Tedrow and R. Meservey. "Spin-Dependent Tunneling into Ferromagnetic Nickel". In: *Phys. Rev. Lett.* 26 (4 Jan. 1971), pp. 192–195. DOI: 10.1103/PhysRevLett.26.192. URL: http://link.aps.org/doi/10.1103/PhysRevLett.26.192.

[6] M. Julliere. "Tunneling between ferromagnetic films". In: *Physics Letters A* 54.3 (1975), pp. 225 –226. ISSN: 0375-9601. DOI: 10.1016/0375-9601(75)90174-7. URL: http://www.sciencedirect.com/science/article/pii/0375960175901747.

[7] Thomas Johann Seebeck. "Metallische Polarisation der Metalle und Erze durch Temperatur-Differenz". In: *Abhandlungen der Königlichen Akademie der Wissenschaften zu Berlin* 1822-1823 (1825), pp. 265–375.

[8] K. Uchida et al. "Observation of the spin Seebeck effect". In: *Nature* 455.7214 (Oct. 2008), pp. 778–781. ISSN: 0028-0836. URL: http://dx.doi.org/10.1038/nature07321.

[9] Jiang Xiao et al. "Theory of magnon-driven spin Seebeck effect". In: *Phys. Rev. B* 81 (21 June 2010), p. 214418. DOI: 10.1103/PhysRevB.81.214418. URL: http://link.aps.org/doi/10.1103/PhysRevB.81.214418.

[10] S. Hunklinger and C. Kittel. *Einführung in die Festkörperphysik*. Einführung in die Festkörperphysik. Oldenbourg Wissenschaftsverlag, 2005. ISBN: 9783486577235. URL: http://books.google.de/books?id=b3L3flBBavQC.

[11] E. Fermi. "Quantisation of the monatomic perfect gas". In: *Atti della Reale Accademia Nazionale dei Lincei* 3 (1926), pp. 145–149.

[12] P. A. M. Dirac. "On the Theory of Quantum Mechanics". In: *Proceedings of the Royal Society of London. Series A* 112.762 (1926), pp. 661–677. DOI: 10.1098/rspa.1926.0133. eprint: http://rspa.royalsocietypublishing.org/content/112/762/661.full.pdf+html. URL: http://rspa.royalsocietypublishing.org/content/112/762/661.short.

[13] S. Blundell and K. Blundell. *Concepts in Thermal Physics*. Oxford University Press, USA, 2006. ISBN: 9780198567707. URL: http://books.google.de/books?id=v2W5ha0E_D4C.

[14] A. v. Ettingshausen and W. Nernst. "Ueber das Auftreten electromotorischer Kräfte in Metallplatten, welche von einem Wärmestrome durchflossen werden und sich im magnetischen Felde befinden". In: *Ann. Phys.* 265.10 (1886), pp. 343–347. ISSN: 1521-3889. URL: http://dx.doi.org/10.1002/andp.18862651010.

[15] Shigeki Onoda, Naoyuki Sugimoto, and Naoto Nagaosa. "Quantum transport theory of anomalous electric, thermoelectric, and thermal Hall effects in ferromagnets". In: *Phys. Rev. B* 77 (16 Apr. 2008), p. 165103. DOI: 10.1103/PhysRevB.77.165103. URL: http://link.aps.org/doi/10.1103/PhysRevB.77.165103.

[16] Walther Gerlach and Otto Stern. "Das magnetische Moment des Silberatoms". In: *Zeitschrift für Physik A Hadrons and Nuclei* 9 (1 1922). 10.1007/BF01326984, pp. 353–355. ISSN: 0939-7922. URL: http://dx.doi.org/10.1007/BF01326984.

[17] J. Kessler. *Polarized Electrons*. Springer Series on Atoms + Plasmas. Springer, 1985. ISBN: 9783540157366. URL: http://books.google.de/books?id=pMOy9AMjzd8C.

[18] Franz Czeschka. "Spin Currents in Metallic Nanostructures". PhD thesis. Technical University of Munich, 2011.

[19] N. F. Mott. "The Scattering of Fast Electrons by Atomic Nuclei". In: *Proceedings of the Royal Society of London. Series A* 124.794 (1929), pp. 425–442. DOI: 10.1098/rspa.1929.0127. eprint: http://rspa.royalsocietypublishing.org/content/124/794/425.full.pdf+html. URL: http://rspa.royalsocietypublishing.org/content/124/794/425.short.

[20] L. Berger. "Side-Jump Mechanism for the Hall Effect of Ferromagnets". In: *Phys. Rev. B* 2 (11 Dec. 1970), pp. 4559–4566. DOI: 10.1103/PhysRevB.2.4559. URL: http://link.aps.org/doi/10.1103/PhysRevB.2.4559.

[21] Robert Karplus and J. M. Luttinger. "Hall Effect in Ferromagnetics". In: *Phys. Rev.* 95 (5 Sept. 1954), pp. 1154–1160. DOI: 10.1103/PhysRev.95.1154. URL: http://link.aps.org/doi/10.1103/PhysRev.95.1154.

[22] Y. Kajiwara et al. "Detection of Spin-Wave Spin Current in a Magnetic Insulator". In: *Magnetics, IEEE Transactions on* 47.6 (June 2011), pp. 1591 –1594. ISSN: 0018-9464. DOI: 10.1109/TMAG.2011.2118747.

[23] M. I. D'yakonov and V. I. Perel'. "Possibility of orienting electron spins with current". In: *JETP Letters* 13.11 (May 1971), pp. 467–9.

[24] Yaroslav Tserkovnyak, Arne Brataas, and Gerrit E. W. Bauer. "Enhanced Gilbert Damping in Thin Ferromagnetic Films". In: *Phys. Rev. Lett.* 88 (11 Feb. 2002), p. 117601. DOI: 10.1103/PhysRevLett.88.117601. URL: http://link.aps.org/doi/10.1103/PhysRevLett.88.117601.

[25] Arne Brataas, Yu. V. Nazarov, and Gerrit E. W. Bauer. "Finite-Element Theory of Transport in Ferromagnet/Normal Metal Systems". In: *Phys. Rev. Lett.* 84 (11 Mar. 2000), pp. 2481–2484. DOI: 10.1103/PhysRevLett.84.2481. URL: http://link.aps.org/doi/10.1103/PhysRevLett.84.2481.

[26] T.L. Gilbert. "A Lagrangian formulation of the gyromagnetic equation of the magnetic field". In: *Physical Review* 100 (1955), p. 1243.

[27] William Fuller Brown. "Thermal Fluctuations of a Single-Domain Particle". In: *Phys. Rev.* 130 (5 June 1963), pp. 1677–1686. DOI: 10.1103/PhysRev.130.1677. URL: http://link.aps.org/doi/10.1103/PhysRev.130.1677.

[28] Jørn Foros et al. "Magnetization Noise in Magnetoelectronic Nanostructures". In: *Phys. Rev. Lett.* 95 (1 June 2005), p. 016601. DOI: 10.1103/PhysRevLett.95.016601. URL: http://link.aps.org/doi/10.1103/PhysRevLett.95.016601.

[29] Jiang Xiao et al. "Erratum: Theory of magnon-driven spin Seebeck effect [Phys. Rev. B 81, 214418 (2010)]". In: *Phys. Rev. B* 82 (9 Sept. 2010), p. 099904. DOI: 10.1103/PhysRevB.82.099904. URL: http://link.aps.org/doi/10.1103/PhysRevB.82.099904.

[30] H. Nyquist. "Thermal agitation of electric charge in conductors". In: *Physical Review* 32 (1928), pp. 110–114. DOI: 10.1103/PhysRev.32.110.

[31] D. Forster. *Hydrodynamic fluctuations, broken symmetry, and correlation functions*. Frontiers in Physics : a lecture note and reprint series. W. A. Benjamin, Advanced Book Program, 1975. URL: http://books.google.de/books?id=iPFQAAAAMAAJ.

[32] K. Uchida et al. "Observation of longitudinal spin-Seebeck effect in magnetic insulators". In: *Applied Physics Letters* 97.17, 172505 (2010), p. 172505. DOI: 10.1063/1.3507386. URL: http://link.aip.org/link/?APL/97/172505/1.

[33] K. Uchida et al. "Spin Seebeck insulator". In: *Nature Materials* 9.11 (Nov. 2010), pp. 894–897. ISSN: 1476-1122. URL: http://dx.doi.org/10.1038/nmat2856.

[34] C. M. Jaworski et al. "Observation of the spin-Seebeck effect in a ferromagnetic semiconductor". In: *Nat Mater* 9.11 (Nov. 2010), pp. 898–903. ISSN: 1476-1122. URL: http://dx.doi.org/10.1038/nmat2860.

[35] Mathias Weiler et al. "Local Charge and Spin Currents in Magnetothermal Landscapes". In: *Phys. Rev. Lett.* 108 (10 Mar. 2012), p. 106602. DOI: 10.1103/PhysRevLett.108.106602. URL: http://link.aps.org/doi/10.1103/PhysRevLett.108.106602.

[36] W. C. Chiang et al. "FMR studies Of $Y_3Fe_5O_{12}/Gd_3Ga_5O_{12}$ (YIG/GGG) superlattices and YIG thin films". In: *Journal of Magnetism and Magnetic Materials* 239.1-3 (Feb. 2002), pp. 332–334. DOI: 10.1016/S0304-8853(01)00655-2.

[37] K. Sun, P. Dorsey, and C. Vittoria. "Zero magnetic field ferromagnetic resonance properties of single-crystal YIG/GGG/YIG layers". In: *Journal of Applied Physics* 69.8 (1991), pp. 6212–6214. DOI: 10.1063/1.348811. URL: http://link.aip.org/link/?JAP/69/6212/1.

[38] J. D. Adam and M. R. Daniel. "Magnetostatic Volume Wave-propagation In Multilayer Yig Ggg Structures". In: *Ieee Transactions On Magnetics* 20.5 (1984), pp. 1246–1248. DOI: 10.1109/TMAG.1984.1063467.

[39] Shinji Mino et al. "Structure and Lattice Deformation of Ce-Substituted Yttrium Iron Garnet Film Prepared by RF Sputtering". In: *Japanese Journal of Applied Physics* 32.Part 1, No. 7 (1993), pp. 3154–3159. DOI: 10.1143/JJAP.32.3154. URL: http://jjap.jsap.jp/link?JJAP/32/3154/.

[40] Vladimir Cherepanov, Igor Kolokolov, and Victor L'vov. "The saga of YIG: Spectra, thermodynamics, interaction and relaxation of magnons in a complex magnet". In: *Physics Reports* 229.3 (July 1993), pp. 81–144. ISSN: 0370-1573. DOI: 10.1016/0370-1573(93)90107-O. URL: http://www.sciencedirect.com/science/article/pii/037015739390107O.

[41] H. T. Liu et al. “Optical and Magnetic Investigation of YA(Fe)O-Garnets”. In: *Chinese Journal of Physics* 49 (2011), pp. 639–646.

[42] M. Swirkowicz et al. “Investigation of structural, optical and lasing properties of YAG : Yb single crystals”. In: *Opto-electronics Review* 13.3 (2005), pp. 213–220.

[43] S. Geller et al. “Ferrimagnetic Garnets Containing Pentavalent Vanadium”. In: *Journal of Applied Physics* 35.3 (1964), pp. 570–572. DOI: 10.1063/1.1713418. URL: http://link.aip.org/link/?JAP/35/570/1.

[44] Matthias Althammer. “A quantitative analysis of the spin Hall magnetoresistance in ferromagnetic insulator/normal metal hybrids”. unpublished. 2012.

[45] Matthias Althammer. “Spin-transport-phenomena in metals, semiconductors, and insulators”. PhD thesis. Technical University of Munich, 2012.

[46] O. Mosendz et al. “Detection and quantification of inverse spin Hall effect from spin pumping in permalloy/normal metal bilayers”. In: *Phys. Rev. B* 82 (21 Dec. 2010), p. 214403. DOI: 10.1103/PhysRevB.82.214403. URL: http://link.aps.org/doi/10.1103/PhysRevB.82.214403.

[47] S. Y. Huang et al. “Transport Magnetic Proximity Effects in Platinum”. In: *Phys. Rev. Lett.* 109 (10 Sept. 2012), p. 107204. DOI: 10.1103/PhysRevLett.109.107204. URL: http://link.aps.org/doi/10.1103/PhysRevLett.109.107204.

[48] Y. Niimi et al. “Extrinsic Spin Hall Effect Induced by Iridium Impurities in Copper”. In: *Phys. Rev. Lett.* 106 (12 Mar. 2011), p. 126601. DOI: 10.1103/PhysRevLett.106.126601. URL: http://link.aps.org/doi/10.1103/PhysRevLett.106.126601.

[49] Mathias Weiler. “Magnon-Phonon Interactions in Ferromagnetic Thin Films”. PhD thesis. Technical University of Munich, 2012.

[50] A. Yoshida and T. Asakura. “A simple technique for quickly measuring the spot size of Gaussian laser beams”. In: *Optics & Laser Technology* 8.6 (1976), pp. 273–274. ISSN: 0030-3992. DOI: 10.1016/0030-3992(76)90042-6. URL: http://www.sciencedirect.com/science/article/pii/0030399276900426.

[51] W. Zinth and H.J. Körner. *Optik, Quantenphänomene und Aufbau der Atome: Mit 13 Tabellen*. Physik : Einführungskurs für Studierende der Naturwissenschaften und Elektrotechnik. Oldenbourg, 1998. ISBN: 9783486240542. URL: http://books.google.de/books?id=6RIeAQAACAAJ.

[52] *MAX300 Series NanoMax 3-Axis Flexure Stage User Guide*. Thorlabs. URL: http://www.thorlabs.de/Thorcat/10900/MAX313D_M-Manual.pdf.

[53] Sir Isaac Newton. *Opticks: or, A treatise of the reflections, refractions, inflections and colours of light*. London: Printed for William Innys at the West-End of St. Paul's, 1730.

[54] D.R. Lide. *CRC Handbook of Chemistry and Physics, 89th Edition*. Taylor & Francis, 2008. ISBN: 9780849321801. URL: http://books.google.de/books?id=P1wkRgAACAAJ.

[55] *RefractiveIndex.INFO*. URL: http://refractiveindex.info.

[56] U. Welp et al. "Domain formation in exchange biased Co/CoO bilayers". In: *Journal of Applied Physics* 93.10 (2003), pp. 7726–7728. DOI: 10.1063/1.1540152. URL: http://link.aip.org/link/?JAP/93/7726/1.

[57] J. Shi et al. "End domain states and magnetization reversal in submicron magnetic structures". In: *Magnetics, IEEE Transactions on* 34.4 (July 1998), pp. 997 –999. ISSN: 0018-9464. DOI: 10.1109/20.706336.

[58] R. D. Enoch and E. A. D. White. "An unusual magnetic domain structure in a single crystal of YIG". In: *Journal of Materials Science* 6 (3 1971). 10.1007/BF00550023, pp. 263–264. ISSN: 0022-2461. URL: http://dx.doi.org/10.1007/BF00550023.

[59] A. Braginski et al. "Domain structure and stress in epitaxial YIG films". In: *Magnetics, IEEE Transactions on* 8.3 (Sept. 1972), pp. 300 –303. ISSN: 0018-9464. DOI: 10.1109/TMAG.1972.1067316.

[60] E. Duda, B. Desormiere, and G. Volluet. "Domain structure in YIG films subjected to magnetic fields and stresses". In: *Magnetics, IEEE Transactions on* 10.3 (Sept. 1974), pp. 634 –637. ISSN: 0018-9464. DOI: 10.1109/TMAG.1974.1058401.

[61] W. X. Xia et al. "Investigation of magnetic structure and magnetization process of yttrium iron garnet film by Lorentz microscopy and electron holography". In: *Journal of Applied Physics* 108.12, 123919 (2010), p. 123919. DOI: 10.1063/1.3524273. URL: http://link.aip.org/link/?JAP/108/123919/1.

[62] R. H. Koch et al. "Thermally Assisted Magnetization Reversal in Submicron-Sized Magnetic Thin Films". In: *Phys. Rev. Lett.* 84 (23 June 2000), pp. 5419–5422. DOI: 10.1103/PhysRevLett.84.5419. URL: http://link.aps.org/doi/10.1103/PhysRevLett.84.5419.

[63] URL: http://www.computerbase.de/news/2012-10/tdk-steigert-datendichte-auf-neues-rekordniveau/.

[64] S. H. Lee et al. “Effect of geometry on magnetic domain structure in Ni wires with perpendicular anisotropy: A magnetic force microscopy study”. In: *Phys. Rev. B* 77 (13 Apr. 2008), p. 132408. DOI: 10.1103/PhysRevB.77.132408. URL: http://link.aps.org/doi/10.1103/PhysRevB.77.132408.

[65] Youfeng Zheng and Jian-Gang Zhu. “Switching field variation in patterned submicron magnetic film elements”. In: *Journal of Applied Physics* 81.8 (1997), pp. 5471–5473. DOI: 10.1063/1.364629. URL: http://link.aip.org/link/?JAP/81/5471/1.

[66] Fabrice Wilhelm. “Magnetic Properties of Ultrathin Films, Coupled Trilayers and 3d/5d Multilayers studied by X-ray Magnetic Circular Dichroism”. PhD thesis. Freie Universität Berlin, 2000.

[67] F. Wilhelm et al. “Magnetic moment of Au at Au/Co interfaces: A direct experimental determination”. In: *Phys. Rev. B* 69 (22 June 2004), p. 220404. DOI: 10.1103/PhysRevB.69.220404. URL: http://link.aps.org/doi/10.1103/PhysRevB.69.220404.

[68] F. Wilhelm et al. “Layer-Resolved Magnetic Moments in Ni/Pt Multilayers”. In: *Phys. Rev. Lett.* 85 (2 July 2000), pp. 413–416. DOI: 10.1103/PhysRevLett.85.413. URL: http://link.aps.org/doi/10.1103/PhysRevLett.85.413.

[69] F. Wilhelm et al. “Systematics of the Induced Magnetic Moments in 5d Layers and the Violation of the Third Hund’s Rule”. In: *Phys. Rev. Lett.* 87 (20 Oct. 2001), p. 207202. DOI: 10.1103/PhysRevLett.87.207202. URL: http://link.aps.org/doi/10.1103/PhysRevLett.87.207202.

[70] P. Poulopoulos et al. “X-ray magnetic circular dichroic magnetometry on Ni/Pt multilayers”. In: *Journal of Applied Physics* 89.7 (2001), pp. 3874–3879. DOI: 10.1063/1.1345862. URL: http://link.aip.org/link/?JAP/89/3874/1.

[71] Stefania Pizzini et al. “Evidence for the Spin Polarization of Copper in Co /Cu and Fe /Cu Multilayers”. In: *Phys. Rev. Lett.* 74 (8 Feb. 1995), pp. 1470–1473. DOI: 10.1103/PhysRevLett.74.1470. URL: http://link.aps.org/doi/10.1103/PhysRevLett.74.1470.

[72] T. Kimura, J. Hamrle, and Y. Otani. “Estimation of spin-diffusion length from the magnitude of spin-current absorption: Multiterminal ferromagnetic/nonferromagnetic hybrid structures”. In: *Phys. Rev. B* 72 (1 July 2005), p. 014461. DOI: 10.1103/PhysRevB.72.014461. URL: http://link.aps.org/doi/10.1103/PhysRevB.72.014461.

[73] Satoshi Yakata et al. “Temperature Dependences of Spin-Diffusion Lengths of Cu and Ru layers”. In: *Japanese Journal of Applied Physics* 45.5A (2006), pp. 3892–3895. DOI: 10.1143/JJAP.45.3892. URL: http://jjap.jsap.jp/link?JJAP/45/3892/.

[74] J. L. Cohn et al. "Giant Nernst Effect and Bipolarity in the Quasi-One-Dimensional Metal $Li_{0.9}Mo_6O_{17}$". In: *Phys. Rev. Lett.* 108 (5 Feb. 2012), p. 056604. DOI: 10.1103/PhysRevLett.108.056604. URL: http://link.aps.org/doi/10.1103/PhysRevLett.108.056604.

[75] Stephan Gepraegs, Sibylle Meyer, and Matthias Opel. "XMCD measurements in Pt/YIG bilayers (tentaitive)". unpublished.

[76] M Reichling and H Gronbeck. "Harmoic Heat-flow in Isotropic Layered Systems and its use for Thin-film Thermal-Conductivity Measurements". English. In: *Journal of Applied Physics* 75.4 (Feb. 1994), pp. 1914–1922. ISSN: 0021-8979. DOI: 10.1063/1.356338.

[77] Augustine Fresnel. *Premier mémoire sur la diffraction de la lumière*. Ed. by Jean-Louis Basdevant. 1815. URL: http://bibnum.education.fr/physique/optique/premier-mmoire-sur-la-diffraction-de-la-lumire.

[78] Katrhin Ganzhorn. *Spatially Resolved Spin Seebeck Experiments*. Bachelorthesis. 2012.

[79] *Low-Noise Voltage Preamplifier*. Stanford Research. URL: http://www.thinksrs.com/downloads/PDFs/Catalog/SR560c.pdf.

[80] *Razor CompuScope 12X2 12-Bit Family of Multi-channel Digitizers for the PCI Express or PCI Bus*. GaGe. URL: http://www.gage-applied.com/products/PDF/Express/Razor_CS12X2-PCI-PCIe.pdf.

[81] O. Forster. *Analysis 1: Differential- und Integralrechnung einer Veränderlichen*. Grundkurs Mathematik. Vieweg+Teubner Verlag, 2011. ISBN: 9783834812513. URL: http://books.google.de/books?id=pgcFad1VC9oC.

[82] M. Reisch. *Elektronische Bauelemente: Funktion, Grundschaltungen, Modellierung mit SPICE*. Springer, 2006. ISBN: 9783540340140. URL: http://books.google.de/books?id=8IbLAAAACAAJ.

[83] H. E. Elsayed-Ali et al. "Time-resolved observation of electron-phonon relaxation in copper". In: *Phys. Rev. Lett.* 58 (12 Mar. 1987), pp. 1212–1215. DOI: 10.1103/PhysRevLett.58.1212. URL: http://link.aps.org/doi/10.1103/PhysRevLett.58.1212.

[84] Rogier H. M. Groeneveld, Rudolf Sprik, and Ad Lagendijk. "Femtosecond spectroscopy of electron-electron and electron-phonon energy relaxation in Ag and Au". In: *Phys. Rev. B* 51 (17 May 1995), pp. 11433–11445. DOI: 10.1103/PhysRevB.51.11433. URL: http://link.aps.org/doi/10.1103/PhysRevB.51.11433.

[85] R. Weber. "Magnon-Phonon Coupling in Metallic Films". In: *Phys. Rev.* 169 (2 May 1968), pp. 451–456. DOI: 10.1103/PhysRev.169.451. URL: http://link.aps.org/doi/10.1103/PhysRev.169.451.

[86] U. N. Upadhyaya and K. P. Sinha. "Phonon-Magnon Interaction in Magnetic Crystals. II. Antiferromagnetic Systems". In: *Phys. Rev.* 130 (3 May 1963), pp. 939–944. DOI: 10.1103/PhysRev.130.939. URL: http://link.aps.org/doi/10.1103/PhysRev.130.939.

[87] L. M. Woods. "Magnon-phonon effects in ferromagnetic manganites". In: *Phys. Rev. B* 65 (1 Nov. 2001), p. 014409. DOI: 10.1103/PhysRevB.65.014409. URL: http://link.aps.org/doi/10.1103/PhysRevB.65.014409.

[88] W. B. Jackson et al. "Photothermal Deflection Spectroscopy and Detection". In: *Applied Optics* 20.8 (1981), pp. 1333–1344. DOI: 10.1364/AO.20.001333.

[89] Robert Werner et al. "Local tunneling magnetoresistance probed by low-temperature scanning laser microscopy". In: *Applied Physics Letters* 99.18, 182513 (2011), p. 182513. DOI: 10.1063/1.3659301. URL: http://link.aip.org/link/?APL/99/182513/1.

[90] P. Hansen, P. Roschman, and W. Tolksdor. "Saturation Magnetization of Gallium-substituted Yttrium Iron-Garnet". English. In: *JOURNAL OF APPLIED PHYSICS* 45.6 (1974), pp. 2728–2732. ISSN: 0021-8979. DOI: {10.1063/1.1663657}.

[91] Elmer E. Anderson. "Molecular Field Model and the Magnetization of YIG". In: *Phys. Rev.* 134 (6A June 1964), A1581–A1585. DOI: 10.1103/PhysRev.134.A1581. URL: http://link.aps.org/doi/10.1103/PhysRev.134.A1581.

[92] J.B.J. Fourier. *Théorie analytique de la chaleur*. Chez Firmin Didot, père et fils, 1822. URL: http://books.google.de/books?id=TDQJAAAAIAAJ.

[93] P. L. Kapitza. "The study of heat transfer in helium II". In: *Journal of Physics* 4.3 (1941), pp. 181–210.

[94] W. A. Little. "The Transport of Heat Between Dissimilar Solids At Low Temperatures". In: *Canadian Journal of Physics* 37.3 (1959), pp. 334–349.

[95] E. T. Swartz. "Thermal resistance at interfaces". PhD thesis. Cornell University, 1987.

[96] E. T. Swartz and R. O. Pohl. "Thermal boundary resistance". In: *Rev. Mod. Phys.* 61 (3 July 1989), pp. 605–668. DOI: 10.1103/RevModPhys.61.605. URL: http://link.aps.org/doi/10.1103/RevModPhys.61.605.

[97] Chan L. Tien and F.M. Gerner. *Microscale Energy Transport*. Ed. by Chang-Lin Tien. Taylor & Francis Inc, 1997.

[98] Peter Debye. "Zur Theorie der spezifischen Waerme". In: *Annalen der Physik* 39 (1912), p. 789.

[99] J. W. S. Rayleigh. *The Theory of Sound*. MacMillan, 1894.

[100] V. Drchal et al. "Electron transport in magnetic multilayers: Effect of disorder". In: *Phys. Rev. B* 65 (21 May 2002), p. 214414. DOI: 10.1103/PhysRevB.65.214414. URL: http://link.aps.org/doi/10.1103/PhysRevB.65.214414.

[101] Bryan C. Gundrum, David G. Cahill, and Robert S. Averback. "Thermal conductance of metal-metal interfaces". In: *Phys. Rev. B* 72 (24 Dec. 2005), p. 245426. DOI: 10.1103/PhysRevB.72.245426. URL: http://link.aps.org/doi/10.1103/PhysRevB.72.245426.

[102] Akashdeep Kamra. priv. comm.

[103] Johannes Lotze. priv. comm.

[104] Hiroyasu Nakayama. unpublished.

[105] Yaroslav Tserkovnyak, Arne Brataas, and Gerrit E. W. Bauer. "Spin pumping and magnetization dynamics in metallic multilayers". In: *Phys. Rev. B* 66 (22 Dec. 2002), p. 224403. DOI: 10.1103/PhysRevB.66.224403. URL: http://link.aps.org/doi/10.1103/PhysRevB.66.224403.

[106] L. Berger. "Emission of spin waves by a magnetic multilayer traversed by a current". In: *Phys. Rev. B* 54 (13 Oct. 1996), pp. 9353–9358. DOI: 10.1103/PhysRevB.54.9353. URL: http://link.aps.org/doi/10.1103/PhysRevB.54.9353.

[107] K. Ando, T. Yoshino, and E. Saitoh. "Optimum condition for spin-current generation from magnetization precession in thin film systems". In: *Applied Physics Letters* 94.15, 152509 (2009), p. 152509. DOI: 10.1063/1.3119314. URL: http://link.aip.org/link/?APL/94/152509/1.

[108] Bin-cheng Li and Shu-yi Zhang. "The effect of interface resistances on thermal wave propagation in multi-layered samples". In: *Journal of Physics D: Applied Physics* 30.10 (1997), p. 1447. URL: http://stacks.iop.org/0022-3727/30/i=10/a=010.

[109] Jean-Christophe Le Breton et al. "Thermal spin current from a ferromagnet to silicon by Seebeck spin tunnelling". In: *Nature* 475.7354 (July 2011), pp. 82–85. ISSN: 0028-0836. URL: http://dx.doi.org/10.1038/nature10224.

[110] G. E. W. Bauer, E. Saitoh, and B. J. van Wees. "Spin caloritronics". In: *Nature Materials* 11.5 (May 2012), pp. 391–399. DOI: 10.1038/NMAT3301.

[111] L. Liu et al. "Spin-Torque Switching with the Giant Spin Hall Effect of Tantalum". In: *Science* 336 (May 2012), pp. 555–. DOI: 10.1126/science.1218197. arXiv:1203.2875 [cond-mat.mtrl-sci].

[112] J. Flipse et al. "Direct observation of the spin-dependent Peltier effect". In: *Nat Nano* 7.3 (Mar. 2012), pp. 166–168. ISSN: 1748-3387. URL: http://dx.doi.org/10.1038/nnano.2012.2.

[113] URL: http://www.diracdelta.co.uk/science/source/s/p/specific%20heat%20capacity/source.html.

[114] URL: http://www.pgmdatabase.com/jmpgm/main.jsp.

[115] G. B. Scott, D. E. Lacklison, and J. L. Page. "Absorption spectra of $Y_3Fe_5O_{12}$ (YIG) and $Y_3Ga_5O_{12}$: Fe^{3+}". In: *Phys. Rev. B* 10 (3 Aug. 1974), pp. 971–986. DOI: 10.1103/PhysRevB.10.971. URL: http://link.aps.org/doi/10.1103/PhysRevB.10.971.

[116] A. E. Clark and R. E. Strakna. "Elastic Constants of Single-Crystal YIG". In: *Journal of Applied Physics* 32.6 (1961), pp. 1172–1173. DOI: 10.1063/1.1736184. URL: http://link.aip.org/link/?JAP/32/1172/1.

[117] URL: http://www.isowave.com/pdf/materials/Yttrium_Iron_Garnet.pdf.

[118] P. Potera et al. "Induced Absorption in Gadolinium Gallium Garnet Irradiated by High Energy ^{235}U Ions". In: *ACTA PHYSICA POLONICA A* 117 (2010), pp. 181–183.

[119] Anne Hofmeister. "Thermal diffusivity of garnets at high temperature". In: *Physics and Chemistry of Minerals* 33 (1 2006), pp. 45–62. ISSN: 0342-1791. URL: http://dx.doi.org/10.1007/s00269-005-0056-8.

[120] N. N. Sirota, P. A. Popv, and I. A. Ivanov. "The Thermal Conductivity of Monocrystalline Gallium Garnets Doped with Rare-Earth Elements and Chromium in the Range 6-300 K". In: *Crystal Research and Technology* 27.4 (1992), pp. 535–543. ISSN: 1521-4079. DOI: 10.1002/crat.2170270421. URL: http://dx.doi.org/10.1002/crat.2170270421.

[121] Slawomir M. Kaczmarek et al. "Changes in optical properties of YAG:Ce single crystals due to codoping and ionizing radiation treatment". In: *International Conference on Solid State Crystals '98: Single Crystal Growth, Characterization, and Applications* (1999), pp. 339–345. DOI: 10.1117/12.343020. URL: http://dx.doi.org/10.1117/12.343020.

[122] RP Photonics. URL: http://www.rp-photonics.com/yag_lasers.html.

[123] Northrop Grumman. URL: http://www.as.northropgrumman.com/products/synoptics_undoped_yag/assets/undop_Data_sheet.pdf.

[124] *Tabellenbuch Mechatronik: Tabellen, Formeln, Normenanwendung.* Europa-Fachbuchreihe für Mechatronik. Europa Lehrmittel Verlag, 2001. ISBN: 9783808545010. URL: http://books.google.de/books?id=u8FCAAAACAAJ.

[125] Gero Bernhard Martin Fiege et al. “Quantitative thermal conductivity measurements with nanometre resolution”. In: *Journal of Physics D: Applied Physics* 32.5 (1999), p. L13. URL: http://stacks.iop.org/0022-3727/32/i=5/a=003.

[126] W. J. Parker et al. “Flash Method of Determining Thermal Diffusivity, Heat Capacity, and Thermal Conductivity”. In: *Journal of Applied Physics* 32.9 (1961), pp. 1679–1684. DOI: 10.1063/1.1728417. URL: http://link.aip.org/link/?JAP/32/1679/1.

[127] G. G. Siu, C. M. Lee, and Yulong Liu. “Magnons and acoustic phonons in $Y_{3-x}Bi_xFe_5O_{12}$”. In: *Phys. Rev. B* 64 (9 Aug. 2001), p. 094421. DOI: 10.1103/PhysRevB.64.094421. URL: http://link.aps.org/doi/10.1103/PhysRevB.64.094421.

[128] M. Dube and P.C.E. Stamp. “Effects of Phonons and Nuclear Spins on the Tunneling of a Domain Wall”. In: *eprint arXiv:cond-mat/9708191* (Aug. 1997). eprint: arXiv:cond-mat/9708191.

[129] F. Kohlrausch and F. Henning. *Praktische Physik: Band 1*. Bd. 1. Teubner, 1950. URL: http://books.google.de/books?id=HiM4QwAACAAJ.

[130] Zhibin Lin, Leonid V. Zhigilei, and Vittorio Celli. “Electron-phonon coupling and electron heat capacity of metals under conditions of strong electron-phonon nonequilibrium”. In: *Phys. Rev. B* 77 (7 Feb. 2008), p. 075133. DOI: 10.1103/PhysRevB.77.075133. URL: http://link.aps.org/doi/10.1103/PhysRevB.77.075133.

[131] J.B. Ketterson et al. “Fermi velocity and Fermi radius in platinum”. In: *Solid State Communications* 6.12 (1968), pp. 851 –854. ISSN: 0038-1098. DOI: 10.1016/0038-1098(68)90071-9. URL: http://www.sciencedirect.com/science/article/pii/0038109868900719.

[132] Xianming Zhou et al. “Pressure-dependent Hugoniot elastic limit of $Gd_3Ga_5O_{12}$ single crystals”. In: *Journal of Applied Physics* 109.8, 083536 (2011), p. 083536. DOI: 10.1063/1.3575330. URL: http://link.aip.org/link/?JAP/109/083536/1.

[133] V. F. Kitaeva, E. V. Zharikov, and I. L. Chistyi. “The properties of crystals with garnet structure”. In: *phys. stat. sol. (a)* 92.2 (1985), pp. 475–488. ISSN: 1521-396X. URL: http://dx.doi.org/10.1002/pssa.2210920217.

[134] B. Lengeler et al. “Precision measurements of cyclotron masses and Fermi velocities in the noble metals by the de Haas-van Alphen effect”. In: *Phys. Rev. B* 15 (12 June 1977), pp. 5493–5503. DOI: 10.1103/PhysRevB.15.5493. URL: http://link.aps.org/doi/10.1103/PhysRevB.15.5493.

[135] *$8\frac{1}{2}$-Digit High Performance Multimeter*. Keithley. URL: http://www.keithley.de/data?asset=361.

Acknowledgements

This thesis is the result of the work of many individuals without whom none of the contents would have been possible.

- *Prof. Dr. Rudolf Gross* for giving his blessing to all my various shopping sessions, the support and input I received and most of all for giving me the opportunity to do this work at the Walther-Meißner-Institute
- *PD. Dr. Sebastian T.B. Gönnenwein* for his passion, his endurance, for "einfach weitermessen", for my thesis' topic and my admittance into the magnetics group.
- *Dr. Mathias Weiler* for supervising my work, introducing me to the spin Seebeck setup at the WMI and his patience with countless requests for help.
- *Dr. Hans Hübl* for his lecture on magnetism and spintronics that roped me into the magnetics group, his critical attitude and practical knowledge.
- *Dr. Matthias Opel* for his support in dealing with the Leibniz Rechenzentrum
- *Dr. Matthias Althammer* for showing me a lot of the ins and outs at the WMI, the production of many many samples, the work on the spin Hall magneto resistance and having to cope with me when Mathias Weiler was not in office.
- *Kathrin Ganzhorn* for doing a big portion of the power dependent spin Seebeck measurements and all of the time resolved ones.
- *Sibylle Meyer* for providing me with many many samples, helping me with the production of such and her work on the spin Hall magneto resistance.
- *Johannes Lotze* for the spin pumping data on YIG.
- The entire rest of the magnetics group *Matthias Pernpeintner, Christoph Zollitsch, Philipp Ross, Dr. Stephan Geprägs, Stefan Altmannshofer* and *Friedrich Witek* for all their contributions and the atmosphere of the magnetics group.
- *Akashdeep Kamra* for his invaluable theoretical contributions to the theoretical understanding of the spin Seebeck effect.
- The technical staff at the WMI, most notably *Robert Müller*, that made many experiments possible in the first place.

- *Thomas Losinger* and the other students in the diploma students' office for providing a healthy atmosphere.
- *The developers* of **GIMP, Inkscape, VESTA, LaTable, Notepad++, TeXnicCenter, Sumatra PDF, JabRef** for devoting so much of their time to develop and distribute awesome software free of charge.
- And last but not least, *my parents* that unconditionally supported me throughout not only this thesis but my entire life.

Persönliche Erklärung

Ich versichere, dass ich diese Diplomarbeit selbstständig angefertigt, sowie alle Stellen, die wörtlich oder annähernd wörtlich aus Veröffentlichungen entnommen wurden, als solche kenntlich gemacht und nur die angegebenen Hilfsmittel verwendet habe. Die Arbeit hat in dieser Form keiner anderen Prüfungsinstitution vorgelegen.

Ort, Datum	Unterschrift